

令和3年度

長岡技術科学大学 大学院工学研究科 博士課程

エネルギー・環境工学専攻

博士論文

論文題目

**Study on Surface Modification of Hydroxyapatite
Particles and Evaluation of Their Hydration States and
Protein Interactions**

(水酸アパタイト粒子の表面改質とその水和状態と
タンパク質相互作用の評価に関する研究)

申請者：Shota Yamada

(山田 翔太)

学籍番号：13109590

Acknowledgments

I wish to express my deepest gratitude to Prof. Dr. Motohiro Tagaya of the Department of Material Science and Technology, Nagaoka University of Technology (NUT), for his continuous and kindly support, supervision, guidance and encouragement throughout my study during the period from 2015 when I was assigned to the Nanobiomaterials laboratory.

In carrying out this study, I received great support from the Japan Society for the Promotion of Science (JSPS) Research Fellowships for Young Scientists. This study was partially supported by a grant from JSPS KAKENHI (Grant-in-Aid for JSPS Fellows, Grant No. 19J21315).

I deeply appreciate Prof. Dr. Shunichi Kidokoro, Prof. Dr. Tsuyoshi Honma and Prof. Dr. Yuichi Otsuka of NUT and Prof. Dr. Tomohiro Hayashi of Tokyo Institute of Technology for giving instructions and helpful comments on this thesis review. I am grateful that Analytical Measurement Center in NUT, which has allowed me to use many analyzers for my study. I would like to thank Dr. Yoshimitsu Sakaguchi of Nagoya University and Dr. Nobuhiro Ogawa of Tokyo University for analysis regarding sample property and morphology. I would like to thank Prof. Dr. Satoshi Motozuka of Kyushu Institute of Technology and Prof. Dr. Tania Guadalupe Peñaflor Galindo of Nagaoka College for their useful comments regarding publication papers.

I would like to express an incredibly special thanks to my colleagues in the Nanobiomaterials laboratory for their help, suggestions and teachings, and especially express my gratitude to Mr. Yadong Chai, Mr. Iori Yamada, Mr. Zizhen Liu, Mr. Kazuto Sugimoto and Mr. Ryota Akutsu for their advising and help every day. The other younger students of the laboratory made an environment that I could focus on the experiment. I am deeply grateful to everyone who took care of me.

Thanks to everyone's cooperation, I was able to finish doctoral course. At the end, I am deeply grateful to my parents (Mr. Masahiko Yamada and Ms. Masami Yamada) who warmly watched and supported my life in doing university life and study.

山田 翔太

Shota Yamada

March 2022

Contents

Chapter 1. General Introduction

1.1 Issues of Bioceramic Particle Surfaces for Substituting Bone Defects	1
1.2 Surface Modification of Hydroxyapatite Particles with Tetraethoxysilane for Bone Regeneration	2
1.2.1 Properties and Applications of Hydroxyapatite Particles	4
1.2.2 Reaction of Tetraethoxysilane with Hydroxyapatite Particles	4
1.2.2.1 Presence of Silicate Ions in Living Body and the Significance	4
1.2.2.2 Possible Reactions	5
1.2.2.3 Mesoporous Silica Formation	5
1.3 Hydration States on Bioceramic Particles	6
1.3.1 Possible Formation Process of Cell-Bioceramic Interfaces	6
1.3.2 Type of Hydration States	7
1.3.3 Hydration Layers on Mesoporous Silica, Silicates, Hydroxyapatite Containing Silicates	8
1.3.4 Poly(ethylene glycol) for Controlling Hydration States	10
1.4 Proteins for Bone Regeneration and Their Preferential Adsorption States on Bioceramic Particles	11
1.4.1 Collagen	11
1.4.2 Albumin	12
1.5 Purpose of This Study	15
1.6 Contents of This Thesis	16
References	17

Chapter 2. Modification of Hydroxyapatite Particles with Tetraethoxysilane and Poly(ethylene glycol) and Evaluation of Their Hydration States and Collagen Fibrillation

2.1 Introduction	24
2.2 Experimental Section	27

2.2.1	Chemicals	27
2.2.2	Synthesis of Silicate-Containing Hydroxyapatite Particles and Their Poly(ethylene glycol) Immobilization	27
2.2.3	Characterization of the Particles	28
2.2.4	Fabrication of Silicate-Containing-Hydroxyapatite Particle Films and the Poly(ethylene glycol) Immobilization	30
2.2.5	Basic Characterization of the Particle Films	31
2.2.6	Formation of Hydration Layers and Collagen Adlayers on the Particle Surfaces	31
2.2.7	FT-IR Spectral Deconvolutions for Analyzing the Hydration States	32
2.2.8	QCM-D Analytical Investigation of the Collagen Fibrillation States	34
2.2.9	FT-IR Spectral Deconvolution for Analyzing the Collagen Adlayers	37
2.3	Results and Discussion	39
2.3.1	Characterization Results of the Silicate-Containing-Hydroxyapatite Particles	39
2.3.2	Hydration State Changes on the Poly(ethylene glycol)-Immobilized Silicate-Containing-Hydroxyapatite Particles with the Collagen Adsorption	43
2.3.3	Surface Modification Effect of the Hydroxyapatite Particles on Collagen Fibrillation via Interfacial Hydration States	48
2.4	Conclusion	56
	References	57

Chapter 3. Modification of Hydroxyapatite Particles with Mesoporous Silica and Poly(ethylene glycol) and Evaluation of Their Hydration States and Albumin Interactions

3.1	Introduction	62
3.2	Experimental Section	65
3.2.1	Chemicals	65

3.2.2 Synthesis of the Mesoporous Silica-Covered Hydroxyapatite Particles and Their Poly(ethylene glycol) Immobilization	65
3.2.3 Formation of Hydration Layers and Albumin Adlayers on the Particles	66
3.2.4 Characterization of the Particles	67
3.2.5 FT-IR Spectral Deconvolutions for Analyzing the Hydration States	70
3.2.6 Evaluation of the Albumin Adsorption Amounts	71
3.2.7 FT-IR Spectral Deconvolution for Analyzing the Albumin Adlayers	72
3.3 Results and Discussion	73
3.3.1 Characterization Results of the Mesoporous Silica-Covered Hydroxyapatite Particles	73
3.3.2 Hydration State Changes of the Mesoporous Silica-Covered Hydroxyapatite Particles with the Albumin Adsorption	82
3.3.3 Surface Modification Effect of the Hydroxyapatite Particles on Albumin Adsorption States by Interfacial Hydration States	88
3.4 Conclusion	92
References	92

Chapter 4. Summary and Future Perspectives

4.1 Summary	97
4.2 Future Perspectives	99
4.2.1 Novel Design of Bioceramic Particles with Both Substitution and Regeneration Properties	99
4.2.2 Prospect of Practical Application for Substituting Bone Defects	101
References	102

Chapter 1

General Introduction

Chapter 1

General Introduction

1.1 Issues of Bioceramic Particle Surfaces for Substituting Bone Defects

In the surgical procedures for treating osteoporosis and bone tumors in human bone tissue, bone defects sometimes occur.^{1,2} In order to repair and regenerate bone defects, autogenous bone and metallic implant grafting have been widely used. For the implantation of autogenous bone, ilium and fibula are excised, molded into the bone defect shape, and then implanted in the bone defect sites.³ However, it is very difficult to mold the excised bone into the bone defect shape, and the long-term surgery based on the subsequent collection and implantation of the living bones will bring a very heavy burden to patients.

Implantation of living bone generates an immune response in the human body. The tissue injury initiates two principal immune responses of both the inflammation and the response for repair (i.e., wound healing reaction).⁴ The successful repair and regeneration by the implanted bioceramic particles mainly depends on their ability to mimic the physiological conditions such as the repair processes that occur after injury and the control of reactions like inflammation responses.⁵ After the implantation, the bioceramic particles covered by blood-derived proteins immediately form a provisional matrix that determines the activation of the coagulation cascade, the complement system and the immune cells, which initiates the inflammatory response.⁶ The major inflammatory response caused by implantation has been reported as infection, large hematomas and reoperation.⁷

To safely and suitably serve the implant for a long period of time without rejection by human body, a metallic implant needs to possess the following essential characteristics, biocompatibility, corrosion resistance, high wear resistance and suitable mechanical properties.⁸ The metallic implants require the use of alloys with virtually inert and highly corrosion-resistant elements or those that exist as trace elements in the body. Although metallic implants can be molded for the bone defect shapes, it is difficult to mold very small shapes corresponding to the minute bone defects. It has also been reported that sufficient fixation cannot be obtained depending on the condition of the bone. In addition, the metallic implants may be damaged several months after the

implantation, requiring reoperation.^{7,9,10} The environment *in vivo* is physically and chemically distinct from ambient conditions. A properly functioning metal (inert material) in the air can undergo severe corrosion *in vivo*. Moreover, a metallic implant subject to a cyclic loading may undergo fatigue fracture, which is the major cause of premature failure of metallic implants.

Injecting bioceramic particles into the bone defect is currently being attempted for repair and regeneration of the bone defects. The bioceramic can be defined as one or more substances (non-drugs), which may have natural (animal tissues, proteins) or synthetic (metals, polymers or ceramics) origin. The bioceramics are suitable to be incorporated in living systems for the repairing or regeneration of partially or totally at any tissue, organ or body functions, with the purpose of maintaining or improving the quality of life of the patients.¹¹⁻¹³ Specific examples include alumina, hydroxyapatite (HA) and bioglass.¹⁴ On the other hand, the biological materials such as bones, skins, tissues, vessels produced by a living system are also used as bioceramics to be implanted in the body.¹⁵ If the bioceramic particles are used for implantation, the risk of inflammation is low. However the material strength is low and the patient needs long rest until the bioceramic particle pastes harden. From the problems, definitive bone defect filling material that promotes regeneration of surrounding tissue has not been created. In addition, the reaction of the bioceramic particle surfaces in biological solution is unclear. Thus, it is necessary to clarify the reaction of bioceramic particle surfaces and adjust the physicochemical properties by surface modification.

1.2 Surface Modification of Hydroxyapatite Particles with Tetraethoxysilane for Bone Regeneration

1.2.1 Properties and Applications of Hydroxyapatite Particles

The HA ($\text{Ca}_{10}(\text{PO}_4)_6(\text{OH})_2$) with a Ca/P ratio of 1.67 is an inorganic component contained in living tissues (bones and teeth), the crystal system is hexagonal, the space group is P63/m, and the unit cell is $0.94 \text{ nm} \times 0.94 \text{ nm} \times 0.68 \text{ nm}$.¹⁶ This material has a molecular weight of 1004.64 g/mol, a theoretical density of 3.156 g/cm^3 and a molar ratio of Ca/P of 1.67 related to its stoichiometry.¹⁷ The lattice constants of hexagonal HA are $a = 9.423 \text{ \AA}$ and $c = 6.875 \text{ \AA}$. The hexagonal HA has mirror planes at $z = 1/4$ and $3/4$ and the hydroxyl arrangement shows two-fold disorder.^{18,19} In the crystal structure, the four columnar Ca (*i.e.*, Ca (I) site) are aligned parallel to the c axis, and the six screw axis Ca (*i.e.*, Ca (II) site) surround the c -axis. Also, hydroxyl groups are present in the part surrounded by the screw Ca. The crystal structure of HA is shown in **Figure 1-1 (a,b)**. (100) and (001) have different surface structures, (100) is negatively charged and (001) is positively charged. Due to this property, the reactivity with proteins also differs in each plane.

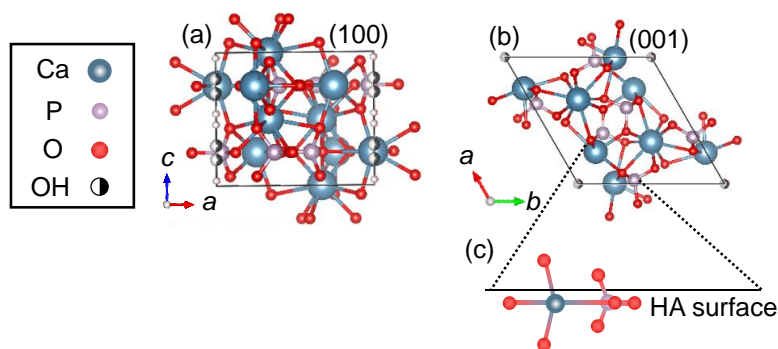


Figure 1-1. HA crystal structure at the view of (a) [100] and (b) [001] and (c) the HA surface cross-sectional image at the (001) surface.

It is reported that the amount of Ab adsorbed onto HA particles is strongly dependent upon the (100), lysozyme adsorption exhibited a minor dependence on the (100) area.^{20,21} Fiber-like and plate-like HA single crystals have been indicated that the (100) is selective for the adsorption of acidic proteins such as Ab, and the (001) is selective for the adsorption of basic proteins such as lysozyme.²² In both planes, the Ca site and P site exist as shown in **Figure 1-1** (c). The high biocompatibility due to a close composition to the hard tissues *in vivo* is an advantage, and the applied study as a biomaterial is being carried out.

HA has the great biocompatibility and presents bioactive properties. HA physiochemically bonds to the bone and promotes bone formation necessary for osseointegration of implant.²³ The property is required to minimize damage in the surrounding tissues and to increase the efficiency of implant. Even that HA can form a direct bond with neighboring bones, it should also be considered for its application as a biomaterial. HA has several attractive and useful properties in the medical field; the main characteristics are: it has very slow resorption and it allows a better new bone formation, it is osteoconductive, biocompatible, resorbable (10–30 %), osteophilic in the process of osseointegration and it has a highly porous structure; this porous structure allows better neovascularization of the formed bone.²⁴ HA can be processed into various shapes, such as particles, porous materials, coating materials, and monoliths. Therefore, it is important to select the suitable shape suitable for the biomedical purpose.

HA particles can be made into a bioceramic paste and used as a biomaterial. The uptake of HA particles with a size of 50–200 nm by the osteoblasts has been investigated, exhibiting excellent uptake efficiency without cytotoxicity.²⁵ HA particles have been demonstrated to have high biocompatibility, good bioactivity, flexible structure, are stable in the physiological environment, corrosion-resistant as well as remarkable higher specific surface area, volume ratio and contain more quantity of grain boundaries than the conventional counterparts offering better surface properties such as topography, energy and wettability that potentially favor the cell response.^{26,27} Besides, HA particles become more active with regard to dissolution and

recrystallization processes that are important characteristics in the bone biomineralization process.²⁸ HA particles can provide better ability suited to biological tissues to empower their regeneration through the natural signaling pathways and using the natural components such as cells, growth factors and proteins can adjust the interactions between the biological tissue and HA particles. The properties of HA particles have the potential applications in the biomedical field, and the detailed research has been required.

1.2.2 Reaction of Tetraethoxysilane with Hydroxyapatite Particles

1.2.2.1 Presence of Silicate Ions in Living Body and the Significance

To prepare the novel bioceramic particles with high biocompatibility, the mimetics of the structures and chemical compositions in the living body are thought to be very important.²⁹ The hard tissues *in vivo* mainly is consisted of the low crystalline HA.^{16,30} As the important points, the hard tissues *in vivo* contain a small amount of silicate as an inorganic subcomponent. In particular, 1–2 g of Si is contained in the living body of an adult and at the concentration of 36 ppm in the bone tissue.^{31,32} The existing form of the Si ion and the specific role in the living body has not been exactly elucidated in details. The state of the silica (SiO₂) has been suggested by an ion microscope analysis,³³ suggesting the importance of the silica for promoting the bone regeneration. In fact, silicate is abundant in the active bone mineralization process and the skeletal growth of a rat was inhibited in a silicate-free environment.^{34,35} There was also a report that the Si concentration increased 50 times after fracture.³⁶ From these backgrounds, the composites of calcium phosphate (e.g., HA) with silica glass have been studied.^{37,38} The formation of the disk between the HA and the silica indicated the partial replacement of PO₄³⁻ in HA with SiO₄⁴⁻ of silica at the interface and resulted in improved bioactive properties.³⁸ Bioglass® containing phosphorus oxide and calcium oxide had an excellent affinity with bone tissue,³⁹ and Kokubo *et al.* have developed the HA–Wollastonite glass (i.e., A–W glass), which has the better mechanical strength by a wet synthesis.⁴⁰ When A–W glass was implanted into the bone defects, the bioactive layer of bone-like apatite was spontaneously formed on the surfaces to induce the significant chemical integration with the bone tissues.⁴¹ However, there has been no reports on the bioceramic particles prepared by precisely hybridizing the low crystalline HA with silicate or silica phase. Thus, I proposed in the present thesis the importance of the precise design of the coexistence of HA with silicate (such as silica) and investigated the possibility of *in vivo* utilization for the novel bioceramic particles.

1.2.2.2 Possible Reactions

From the viewpoint of silicate in the living body, silicate-containing HA particles (SiHA) have been synthesized and discussed.⁴²⁻⁴⁵ In previous thesis, SiHA particles have been mainly synthesized. It is believed that SiO_4^{4-} substituted the PO_4^{3-} in the structure of HA. SiHA particles were mainly prepared by wet process or hydrothermal method, however stable substitution requires calcination at high temperature. The crystallinity of HA will improve with high calcination temperature however the biocompatibility will decrease. Therefore, when SiHA particles are synthesizing for use *in vivo*, it is necessary to prohibit the calcination process. Silicon alkoxide has been used as a silicate source for the synthesis. With the improvement of framework stability, the silicon alkoxide undergoes linear and three-dimensional condensation reactions under acidic and basic conditions, respectively, indicating the importance of the stable silica framework synthesis under the basic conditions (**Figure 1-2**).⁴⁶

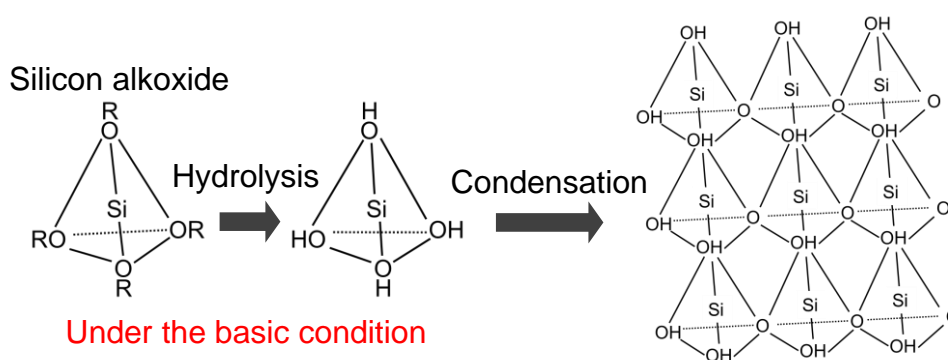


Figure 1-2. Illustration of the possible mesoporous silica formation process.

1.2.2.3 Mesoporous Silica Formation

Mesoporous silica (MS) particles have been prepared by the condensation reaction between silicon alkoxide at around the surfactant rod-like micelles as the supramolecular template to subsequently form the mesopores by a calcination process (**Figure 1-3 (a)**).^{47,48} MS particles indicate a high surface area ($>1000 \text{ m}^2/\text{g}$) and large pore volume ($>1.0 \text{ cm}^3/\text{g}$) by mesoporous structure and tunable pore size (2–30 nm).⁴⁹⁻⁵² In the previous thesis, MS particles have been studied by exploiting the regularly-arranged mesopores and specific adsorption properties for catalysis, separation, sensing, and drug delivery applications.⁵³ In order to precisely control the mesopore surface properties, the importance of both shapes and particle sizes, and silica framework stability of MS particles has been suggested.⁵⁴ As the shape control, a triblock copolymer comprising poly(ethylene glycol) (PEG) and poly(propylene glycol) (PPG) (e.g., Pluronic P123 (P123)) can be used for suppressing the grain growth and aggregation by a strong

steric repulsion force of the PEG to provide the monodispersed spheres.⁵⁵ For the framework stability improvement, the MS formation processes have been undergone under the basic condition. When we need to obtain MS-covered HA particles, it is necessary to be synthesized under the basic condition according to the previous reports.⁵⁶⁻⁵⁸

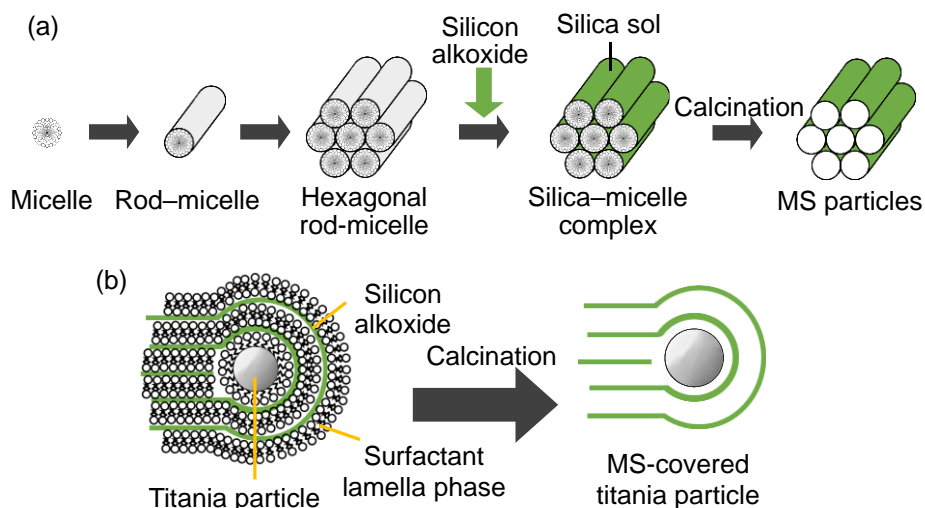


Figure 1-3. Illustration of (a) the MS particles formation process and (b) surfactant nanolayer structures on titania particles.

MS-covered HA particles for the development of new drug delivery systems have been synthesized.^{59,60} The particles have high biocompatibility and have been shown to be better particles for drug delivery systems. When bioceramic particles are coated with MS, the structure is thought to be formed as shown in **Figure 1-3 (b)**.⁶¹ Silicon alkoxide and surfactant are added to the aqueous solution in which the titania particles are dispersed, and after the surfactant micelles are regularly arranged and formed lamella phase around the titania particles. The silicon alkoxide enters the gaps of micelles and undergoes the condensation reaction. Then, the particles having a slit-like mesoporous phase around the bioceramic particles can be obtained by removing only the surfactant.⁶² In this way, it is necessary to consider the reaction between MS and HA particles.

1.3 Hydration States on Bioceramic Particles

1.3.1 Possible Formation Process of Cell-Bioceramic Interfaces

Cell adhesion is involved in a variety of natural phenomena such as embryogenesis, tissue structure maintenance, wound healing, immune response, metastasis, and tissue integration.⁶³ Consequently, in order to repair and regenerate the bone defects with HA particles, it is necessary

to consider the cell behavior in contact with the particles. In general, three processes show after implantation of bioceramic particles including HA are implanted into the body (**Figure 1-4**).^{64,65} First, ions and water molecules reach the bioceramic particle surfaces. Then, the substances interact and bind each together depending on the surface properties and the hydration layer is formed in the living body. Second, a protein adlayer is formed by recognizing the hydration layer, and cell adhesion and spreading are performed by recognizing the protein denaturation component ratios. Therefore, when considering the cell adhesion behavior, it is necessary to consider the formation of the hydration layer.

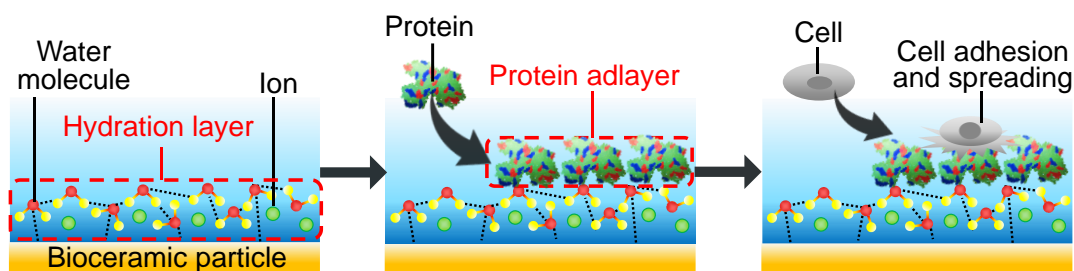


Figure 1-4. Illustration of the formation process of cell-bioceramic particle interfaces in the reactions: hydration layer formation, protein adsorption and cell adhesion.

From the background, the effective bone regeneration by the adsorption of bone morphogenetic proteins on bioceramic particles has been studied so far.^{66,67} In order to achieve the control of steric conformation (i.e., suppressing the denaturation) of the adsorbed proteins for efficient cell adhesion, it is necessary to investigate the hydration layers on the bioceramics.^{68,69} The various intermolecular water–water and water–ion interactions were worked in the hydration layers,⁷⁰ suggesting that the surface hydration structures can directly contribute to the adsorbed protein conformation.^{71–73} However, there is a lack of in-depth discussion about the relationship between the hydration layer and the protein adsorption on the bioceramic particles.

1.3.2 Type of Hydration States

In the main polymeric material fields, the hydration layers can be dominantly attributed to three water components of free, intermediate and nonfreezing states.⁷¹ **Table 1-1 (a)** shows the pattern diagram and properties of the hydration layers. Here, τ_c is relaxation time (sec) which was measured by NMR analysis and ν_{IR} is wavenumber (cm^{-1}) of adsorption band observed as O–H stretching vibration with Fourier transform infrared spectrophotometer (FT-IR) spectrum. The hydration layers can be formed and deposited on the polymers in the order of nonfreezing water, intermediate water, free water and bulk water.⁷⁴ The nonfreezing water strongly interacts and

hydrogen bonds with the polymers and proteins. The τ_c of nonfreezing water is 10^{-8} – 10^{-6} sec, and the ν_{IR} is observed at 3600 cm^{-1} . The intermediate water prevents the proteins from directly contact with the polymers, some water molecules are bonded with nonfreezing water. The τ_c of intermediate water is 10^{-10} – 10^{-9} sec, and the ν_{IR} is observed at 3400 cm^{-1} . The free water can be freely exchanged with bulk water to resultantly exhibit the properties such as the bulk state. Free water forms hydrogen bonds with free water. The τ_c of free water is 10^{-12} – 10^{-11} sec, and the ν_{IR} is observed at 3200 cm^{-1} .

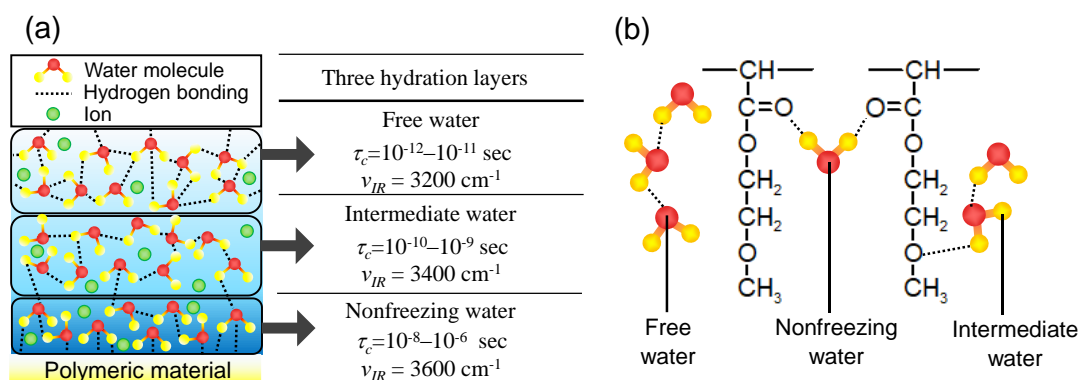


Table 1-1. (a) Classification of hydration layers, and relaxation time and vibration state. (b) representative hydration structures of poly(2-methoxyethyl acrylate).

The existential states of three water components in the polymeric material fields (e.g.: poly(2-methoxyethyl acrylate)) are illustrated in **Table 1-1 (b)**. The classification of hydration water depends on the number of hydrogen bonds between the polymer and the water molecules. It applies to both the water on polymer surface and the water between polymer chains. In the study of PEG, the oxygen atom of $-\text{CH}_2-\text{CH}_2-\text{O}-$ and the terminal $-\text{OH}$ group have preferentially formed the hydrogen bonding with water molecules,⁷⁵ suggesting that the hydration layers arising during cold crystallization may play an important role in the expressing blood compatibility.⁷⁶ This hydration layer was defined as the intermediate water that prevents the denaturation of adsorbed protein.^{77,78} The nonfreezing water and intermediate water can be totally defined and evaluated as bonding water, the weight of bonding water in the hydration layers of poly(2-methacryloyloxyethyl phosphorylcholine) has been reported.⁵³

1.3.3 Hydration Layers on Mesoporous Silica, Silicates, Hydroxyapatite Containing Silicates

The hydration layers on bioceramics including silicate particles have not been sufficiently discussed so far. The MS nanoparticles have been attracting attention in bioceramics for the uses

as sensors and drug delivery systems.^{53,79} It is thought that MS particles can be promising bioceramic particles to study the hydration layers based on the confined water molecules at the mesostructures.⁸⁰⁻⁸³ MS particles trap water in the pores and exhibit a strong interaction with the pore wall. It has been known that the melting point of water decreases in pore structures such as MS.⁴⁶ The water molecules on silica gels have strongly interacted with the pores and exhibited a lowered melting point like the nonfreezing water behavior.⁸⁴ The hydration layer structures of MS particles have been controlled by the introduction of heteroelements into silica frameworks and the water-interactive properties on the mesopores had been clearly changed.^{85,86}

One way to control the hydration layers is to introduce of heteroelements into the particles. In the previous thesis, the phosphorus-containing MS films were synthesized and the hydration layers formed on the films were investigated (**Figure 1-5**).⁸⁶ The functional groups on the outermost surfaces exist in the states of P-O^- , P-OH , Si-O^- and Si-OH .^{86,87} The water molecules would be irregularly hydrogen-bonded with two different binding sites (Si site and P site), so that the O-H stretching vibration became asymmetric and the hydrophilicity and hydrogen-bond ability of the film surfaces were enhanced. Therefore, the O-H stretching vibration became more asymmetric with increasing the P site. When synthesizing the SiHA particles, similar changes are expected. The functional groups of Si-O^- , Si-OH , P-O^- , P-OH , Ca-O^- and Ca-OH exist at the SiHA surfaces. It is quite possible that the different functional groups form irregular hydrogen bonds with water molecules, resulting in the irregular hydrogen bond network. On the other hand, HA has at least 35 mM/g hydration water.⁸⁸ When converting molar concentration to volume, the hydration water of HA particles is 1.9 times their volume. In our group, the hydration layers on the mesopores have been controlled by the hybridization of MS with HA nanocrystals,⁸⁹

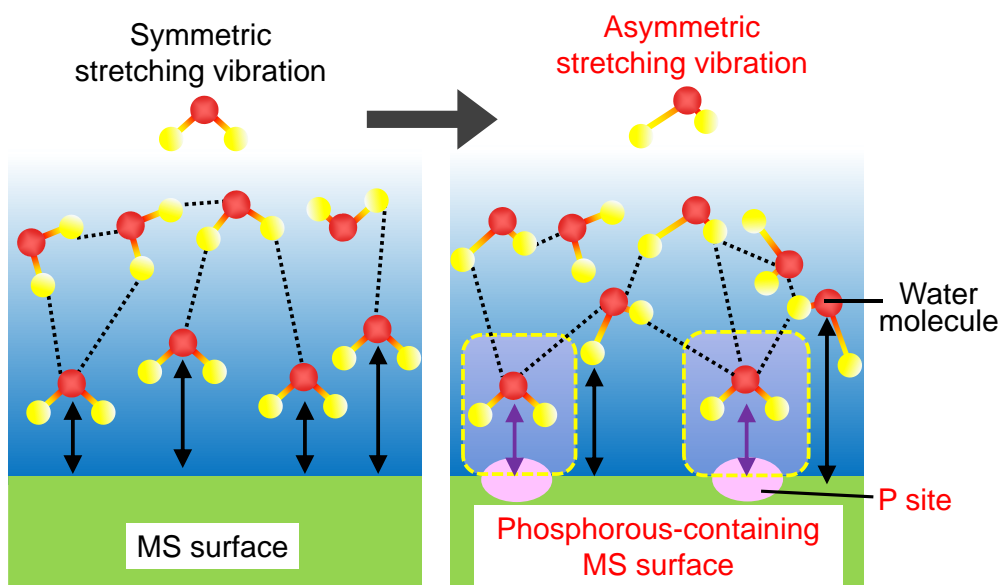


Figure 1-5. Illustration of the hydroxyl group stretching vibration mode of water molecules on the phosphate-containing MS surface.

suggesting that the component ratios of free water to bonding water on MS effectively affected the protein adsorption state. Therefore, it is considered that the hydration layers can be dynamically changed by controlling the introduction of silicate and the mesostructures of MS particles.

1.3.4 Poly(ethylene glycol) for Controlling Hydration States

As the candidate technique to control the hydration layers, the modification of the molecules by adding polymer chains can be considered.⁹⁰ The possible illustration is shown in **Figure 1-6**. It has been known that there is the technique for controlling the hydration state by polymer chains, and it has been reported that polymer chains can form the polymer-interactive layers to interact strongly with the hydration layers.⁹¹⁻⁹³ In particular, the PEG encloses the water molecules to form the polymer-interactive layers.^{91,94} In particular, PEG indicates the high biocompatibility and has been considered for the surface modification agent. The PEG in the polymer-interactive layer form hydrogen bonds with water molecules, and then water molecules are stabilized by highly irregular interactions with PEG, bioceramic particle surfaces, other water molecules, and ions. Since the water molecules in PEG cannot bond enough with each other molecules, the number of hydrogen bonds with other water molecule are maximized and a strong hydrogen bond network is formed inside the water cluster.⁹⁵ Moreover, the polymer-interactive layer induces specific protein adsorption⁹⁶ and also affects protein denaturation. Therefore, when the polymer-interactive layer is formed on the bioceramic surfaces, the changes in the hydrogen bonding state and the hydration state are expected, which are thought to affect the protein adsorption state.

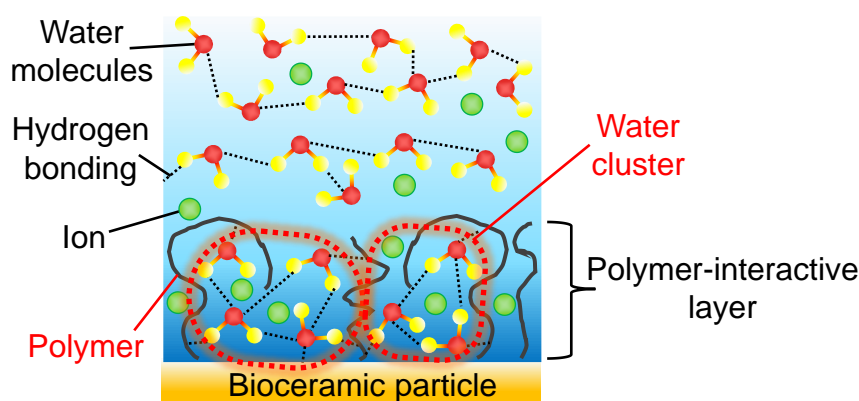


Figure 1-6. Possible illustration of the polymer-interactive layer of polymer chains and water molecules.

1.4 Proteins for Bone Regeneration and Their Preferential Adsorption States on Bioceramic Particles

1.4.1 Collagen

Col is the most abundant protein *in vivo*. More than one-third of body's protein tissue are consisted by Col.^{97,98} Col has been identified about 28 types so far. Among them, type I Col is the most common type found in the extracellular matrix (ECM), particularly in tissues like tendon and bone.^{99,100} Col is formed by the distinctive domain of *G-X-Y* polypeptide. Here, *G* is glycine, *X* is proline and *Y* is hydroxyproline. Hydroxyproline is normally not obtained in other proteins, while in Col it composes more than half of the total amino acid content.^{101,102} Col is composed of repetitions of the *G-X-Y* unit. The *G-X-Y* polypeptide repetition structure forms the α -chains. Three α -chains are linked to each other to build the distinctive triple helix of type I, II and III Col.¹⁰³ The triple helix of type I col which is commonly contained in living bone consists of two identical $\alpha 1$ and one $\alpha 2$ -chain with about 1000 amino acids (Mw: about 100 kDa), and is approximately 300 nm in length and 1.5 nm in diameter (**Figure 1-7 (a)**).¹⁰³ Therefore, the Col molecule has about 3000 residues of amino acids (Mw: about 300 kDa). Type I Col is synthesized as a monomeric precursor, which is secreted by exocytosis into the ECM.¹⁰⁴ The Col precursor contains noncollagenous C- and N-propeptides, which are linked to the triple-helical domain by short sequences called telopeptides.¹⁰⁵ After the enzymatic removal of propeptides, the solubility of Col monomers decreases, and they spontaneously form Col fibrils with the assistance of the remaining nonhelical telopeptides.^{106,107} Therefore, Col exists in a fibrous state (Col fibril) in the living body. Col has a carboxyl group ($-\text{COOH}$, acidic group) and amino group ($-\text{NH}_2$, basic

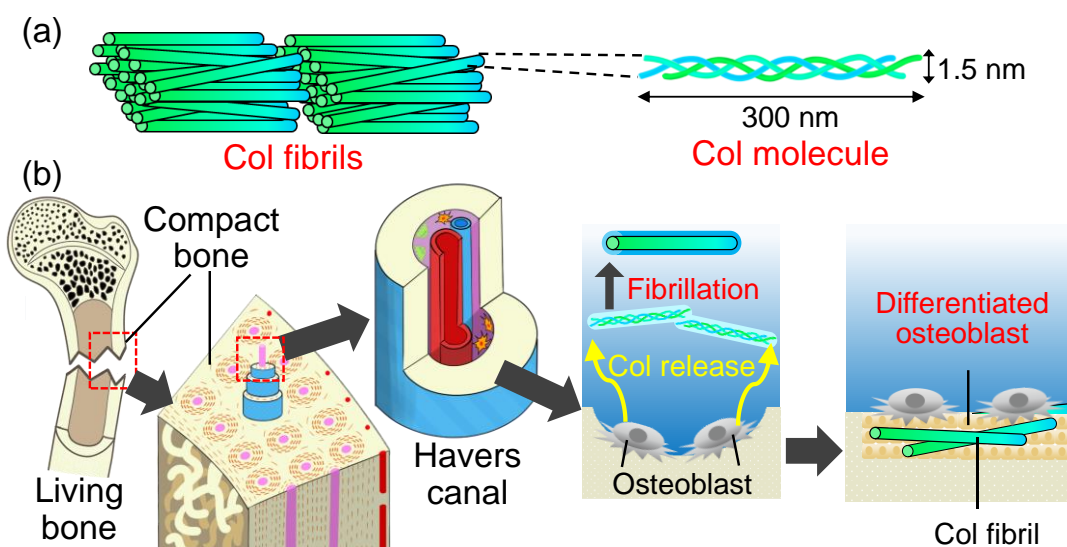


Figure 1-7. (a) Illustration of Col fibrils and molecule, (b) hierarchical structures of inorganic/organic hybrids cancellous bone tissue and effect of Col on osteoblasts.

group) in the *G-X-Y* polypeptide structure. Col has the amino terminus and the carboxyl terminus, so it has various adsorption sites. The carboxylate group of Col is assumed to play the main role in the bone regeneration.¹⁰⁸

Col plays an important role in bone regeneration. The Col contained in the bone defect site is shown in **Figure 1-7 (b)**. Bone tissue can be classified into the spongy bone and compact bone. The Col fibrils are organized in a lamella structure, which are parallel to each other in compact bone. The Col fibrils form a set of concentric layers of circular lamellae, called Havers canal.¹⁰⁹ Also, osteoblast and osteoclast exist on the scale of the Havers canal. During bone regeneration, osteoblasts release type I Col in addition to osteocalcin, bone sialoprotein and osteopontin. These proteins released by osteoblasts are collectively called extracellular matrix (ECM). In the bone regeneration process, the ECM is initially amorphous and non-crystalline. The osteoblasts create an environment for the concentration of calcium and phosphate,¹¹⁰ the ECM gradually transforms into more crystalline forms.¹¹¹ The following factors are speculated to be the cause of crystallization¹¹²; nucleation from solution by charged proteins other than collagen,^{113,114} ion accumulation by matrix vesicles,^{115,116} transient formation of amorphous mineral precursor and crystallization of hydroxyapatite (HA).^{117,118} The Col in ECM spontaneously aligns and fibrosis in the process. HA nanocrystals are regularly arranged on the Col fibrils to form cancellous bone tissue as the inorganic/organic composites. Col fibril plays as a template and may also initiate and propagate mineralization.^{119,120} Therefore, when synthesizing bioceramic particles for bone regeneration, it is important to promote the fibrillation of Col on the surface of the bioceramics.¹²¹ From the background of HA and Col composites in the living body, HA and Col composites are synthesized and expected for replacing bone defects. The HA and Col composite showed biocompatibility and better osteoconductive properties.^{122–124} As a scaffold materials, the composite had excellent biodegradability and osteogenic cells adhesion ability compared to polymer scaffolds.^{125,126} Thus, Investigation of HA and Col composite structure is useful in making better bioceramic particles to repair and regeneration of bone defects.

1.4.2 Albumin

Human serum contains water, saccharide, inorganic ions (Na^+ , K^+ , Ca^+ , Mg^+ , Cl^- , HCO_3^- , HPO_4^{2-} , SO_4^{2-}) and proteins ((Albumin (Ab), γ -globulin, transferrin and lactoferrin). Among them, Ab is an important protein that occupies 60 % of the total proteins. The PI of Ab is 4.7–4.9, so it is negatively charged in the biological fluid with $\text{pH}=7.4$.¹²⁷ Ab has an asymmetric heart-like structure in which three main domains are divided into the already mentioned six subunit domains. The molecular size of the hydrated Ab is $14 \times 3.8 \times 3.8$ nm (elliptical shape).¹²⁸ The Ab adsorption state is restricted to be a monolayer.¹²⁹ Adsorptive biomolecules have various functional groups including hydrophobic groups (aromatic rings, alkyl chains, etc.), hydrophilic groups ($-\text{OH}$, $-$

NH₂, etc.) and dissociation groups (–COO[–], –NH₃⁺, =PO₄[–], etc.). The hydrophilic and dissociation groups interact with hydrogen bonds of water molecules in an aqueous solution. Ab has high hydrogen-bonding properties, so it is necessary to consider the property for the reaction with water in the living body.

The effect of Ab on living bone is shown in **Figure 1-8**. Yamaguchi *et al.* have shown that Ab production increases locally after bone fracture.¹³⁰ They have shown that bone marrow-derived cells and osteoblasts also have the capability of Ab production.¹³¹ The supplementation of Ab increased the proliferation of osteoblasts in the cell culture. In addition, the Ab supplementation also reduced the alkaline phosphatase activity of osteoblasts via inhibition of the runt-related transcription factor 2 (Runx2) pathway. The suppression of the Runx2 pathway inhibits the differentiation of the osteoblasts, it is assumed that Ab indirectly supports the proliferation activity.¹³² There was also a report that hypoalbuminemia is associated with osteoporosis.¹³³

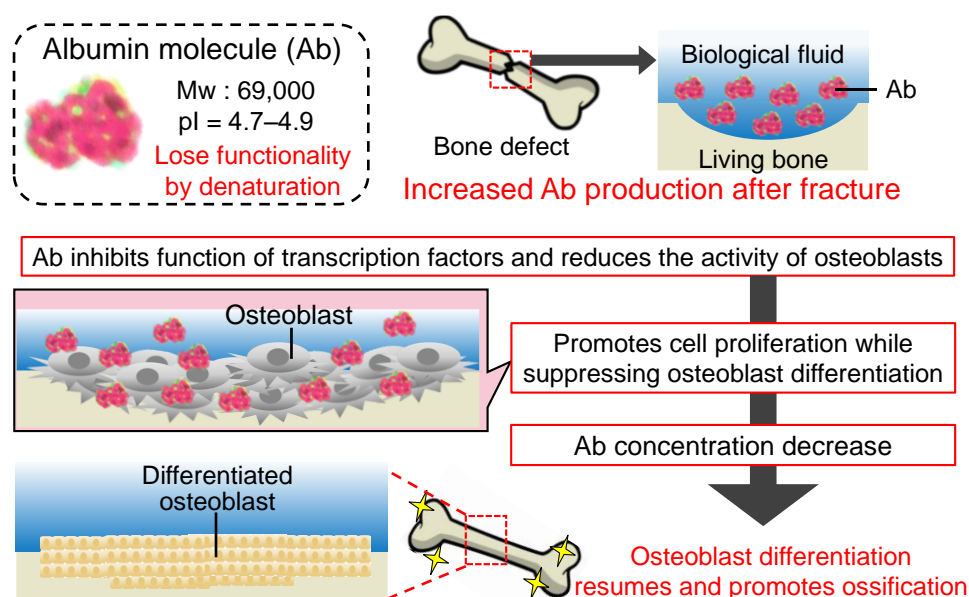







Figure 1-8. Overview and effect of Ab for bone regeneration.

The research of Ab-containing bioceramics for bone regeneration is underway. Ab coated bone allografts showed excellent remodeling characteristics.^{134,135} Bernard *et al.* investigated cell adhesion onto HA coated with bone sialoprotein and osteopontin, and Ab was used to block nonspecific binding sites.¹³⁶ The result showed that Ab promoted osteoblasts adhesion. The incorporation of Ab into HA scaffolds as biodegradable bone substitutes or drug delivery platforms has also been proposed.¹³⁷ These HA/Ab scaffolds *in vivo* indicated the highest bone formation and bone regeneration property. In this way, the combination of HA and Ab is thought to lead to the development of better materials for bone repair and regeneration. The interaction of

Ab with HA has been indicated to be dependent on electrostatic interaction between the carboxyl groups of Ab and the calcium ions exposed on the HA surface and/or ion exchange.¹³⁸ In addition, it is proposed that the interaction occurs through the participation of charged domains with specific surface sites and hydrogen bonding of neighbouring parts of the molecule with polar surfaces.¹³⁹ Thus, when designing biomaterial, it is necessary to consider of functional groups and charges of Ab and HA.

Proteins form a three-dimensional structure by forming peptide bonds between amino and carboxyl groups of amino acids. Proteins consist of the primary structure (sequence of polypeptide chain amino acid residues), secondary structure (local interactions between stretches of a polypeptide chain), tertiary structure (the overall the three-dimensional folding by the secondary structure) and quaternary structure (orientation and arrangement of subunits in a multi-subunit protein). When evaluating the three-dimensionality and degree of denaturation of Col and Ab, it is necessary to analyse the secondary structure. The main classifications of secondary structure are shown in **Table 1-2**. It has been known that the α -helix with helical shape is the most abundant and most stable ordered structure. The content of this structure has a strong effect on the three-dimensional conformation and subsequent biological activity.^{140,141} The β -sheet indicates a sheet-like structure formed by hydrogen bonds in which two or more linear parts of protein are arranged side by side. The predominant secondary structural elements (α -helix and β -sheet) provide the information about the protein conformational state.¹⁴² Random structure also called random coil, means denatured structure. Turn is a secondary structure component that does not form α -helix and β -sheet structure, and can be seen as a mainly irregular structure. β -Turn shows sharply bent part of peptide chain among the secondary structures of globular proteins. If the protein interacts strongly with material, the protein is denatured and lose its original function. When supporting Col or Ab on bioceramic particles, it is necessary to consider the adsorption state. Furthermore, the secondary structure of α -helix and β -sheet were detected at the Col fibril's

Table 1-2. Detailed information of the protein secondary structures.

	β -sheet	Random (coil)	α -helix	Turn	β -Turn
Shape diagram					
Structure	Regularly sheet-like	Denatured	Regularly helical	Irregular	Sharply bent of peptide chain
General attribution by FT-IR (cm^{-1})	1630	1645	1655	1665	1680 1690

surface by Raman microspectroscopy spectra.¹⁴³ The Col molecule is fibrillized through the formation of lysine derived intra- and inter-molecular cross-links.^{144–146} At the ends of adjacent Col fibrils, an amino acid called lysine contained in the α chain and lysine hydroxide in the α chain of another Col fibril is aldol-bonded (crosslinked) by lysyl oxydase. Therefore, Col fibrillation may cause denaturation of α -helix and β -sheet at the Col fibril's surface.

1.5 Purpose of This Study

In order to repair and regenerate bone defect, autogenous bone and metallic implant grafting have widely been used. However, there have been the problems mentioned above. The bioceramic particles are known to be useful for solving, and the desing for promoting the effective bone regeneration should be developed. In addition, it is necessary to synthesize the bioceramic particles that can support Ab and Col with *in vivo* protein structures and states which can promote the bone regeneration. As the protein-interactive bioceramic, HA can be raised and has the several attractive properties that are useful in the biomedical field (e.g.: biocompatibility, protein adsorption capacity and stability in the physiological environment). In order to adsorb the proteins with an ideal state for our body tissues, it is necessary to control the hydration layers of the particle surfaces. The thesis purpose is to prepare the novel bioceramic particles with high biocompatibility through the mimetics and optimization of the chemical compositions and hydration layers in living body bone. Based on a human bone mainly composed of HA and contain a small amount of silicate, the coexistence of HA with silicate was designed. Moreover, the hydration state on the surfaces was controlled by introducing heteroelements elements and forming polymer-interactive by PEG as shown in **Figure 1-9**. First, the HA particles with the similar concentrations of silicate to living bone

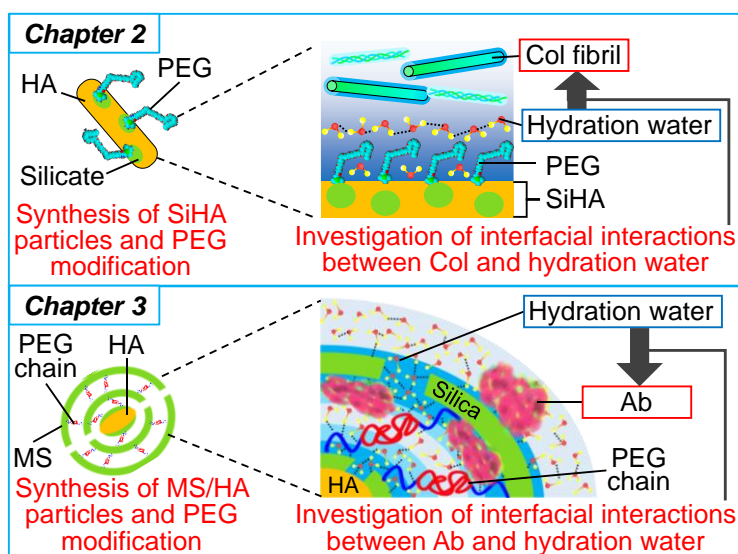


Figure 1-9. Outline of this study.

were synthesized and were immobilized PEG on the surfaces in **Chapter 2** (i.e., SiHA particle surfaces). Then, the interfacial effect of the surface hydration layers on Col fibrillation states was investigated. Second, the HA particles covered with the MS phase were synthesized in the presence of PEG chain in **Chapter 3** (i.e., MS/HA particles). Then, the interfacial effect of the surface hydration layers on the adsorbed Ab states were investigated.

1.6 Contents of This Thesis

In this thesis, it was investigated about “Study on Surface Modification of Hydroxyapatite Particles and Evaluation of Their Hydration States and Protein Interactions”. Hydroxyapatite (HA) particles containing silicate that mimics the living bone were synthesized, these HA particles were immobilized by poly(ethylene glycol) (PEG), evaluated and clarified the hydration layers and protein adlayers. This thesis consists of four chapters. (Figure 1-10).

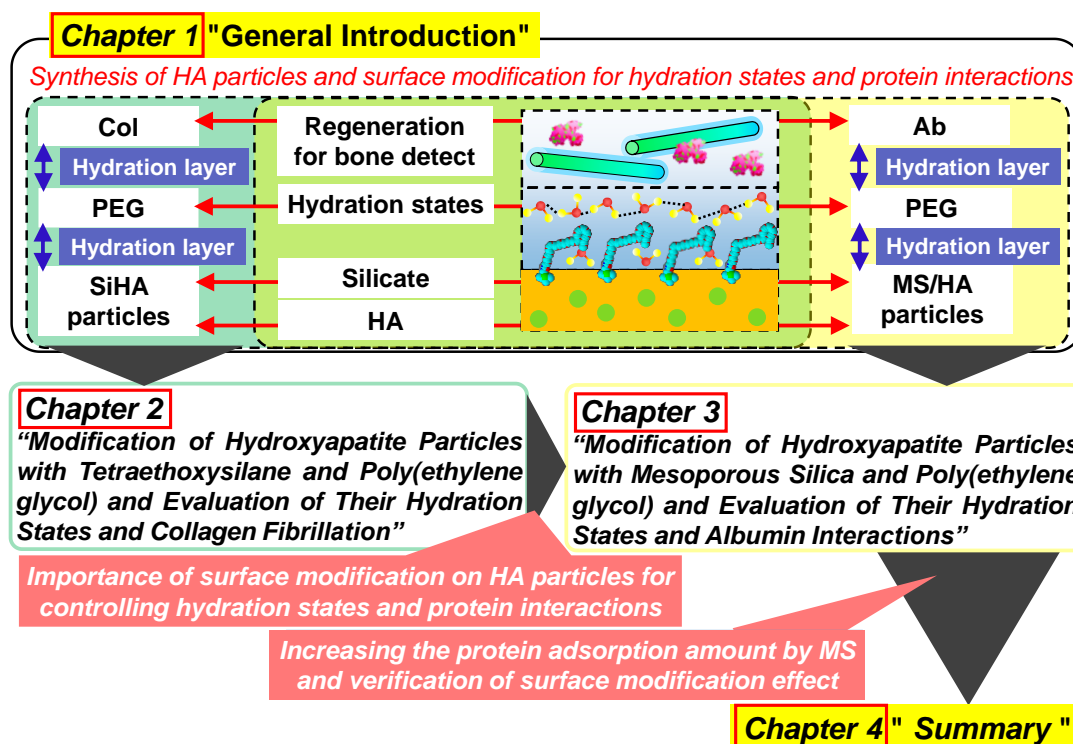


Figure 1-10. Chapter contents and their constructions of this thesis.

In **Chapter 1**, "General Introduction", conventional types, problems and issues with the bioceramics for bone defects were explained, and the necessity to synthesize a new bioceramic particles for bone defects was described. The necessity of synthesizing particles that can support collagen (Col) and albumin (Ab) that promotes bone regeneration with ideal protein structures was proposed. Then, it was shown the importance of designing the

coexistence of HA with silicate for mimetic compositions in the living body. Furthermore, it was described the hydration layer affects protein secondary structures and explained how the PEG affect the hydration layers, and showed the significance and purpose of the thesis.

In **Chapter 2**, “*Modification of Hydroxyapatite Particles with Tetraethoxysilane and Poly(ethylene glycol) and Evaluation of Their Hydration States and Collagen Fibrillation*”, the silicate-containing HA (SiHA) particles were synthesized, and the SiHA particles were immobilized by PEG. The hydration layers before and after Col adsorption were evaluated, and the secondary structures of the subsequently-adsorbed Col were also evaluated. The effects of silicate and PEG in SiHA particles on the hydration and Col adlayers were evaluated.

In **Chapter 3**, “*Modification of Hydroxyapatite Particles with Mesoporous Silica and Poly(ethylene glycol) and Evaluation of Their Hydration States and Albumin Interactions*”, aiming to increase the Ab adsorption amounts and verify the results of **Chapter 2**, the HA particles were covered with the mesoporous silica (MS) phase in the presence of PEG chain to synthesize the novel mesoporous bioceramic particles. The control of hydration layers by the addition of PEG chain was proposed and investigated. Moreover, Ab adsorption amounts and the interfacial effect of the hydration layers on the Ab adsorption was investigated.

In **Chapter 4**, “*Summary*”, it was summarized the usefulness of the HA particles containing silicate and PEG of the thesis for control of hydration layers and protein adlayers. It was found that PEG promote Col fibrillation in **Chapter 2**, MS phase and PEG chain affect hydration state in **Chapter 3**.

References

- 1 O. Johnell and J. A. Kanis, *Osteoporos. Int.*, 2006, **17**, 1726–1733.
- 2 A. Sobti, P. Agrawal, S. Agarwala and M. Agarwal, *Arch. bone Jt. Surg.*, 2016, **4**, 2–9.
- 3 N. A. Ebraheim, H. Elgafy and R. Xu, *J. Am. Acad. Orthop. Surg.*, 2001, **9**, 210–218.
- 4 S. H. Kelly, L. S. Shores, N. L. Votaw and J. H. Collier, *Adv. Drug Deliv. Rev.*, 2017, **114**, 3–18.
- 5 C. J. Kirkpatrick, V. Krump-Konvalinkova, R. E. Unger, F. Bittinger, M. Otto and K. Peters, in *Biomolecular Engineering*, 2002, vol. 19, pp. 211–217.
- 6 S. Franz, S. Rammelt, D. Scharnweber and J. C. Simon, *Biomaterials*, 2011, **32**, 6692–6709.
- 7 E. M. Younger and M. W. Chapman, *J. Orthop. Trauma*, 1989, **3**, 192–195.
- 8 Q. Chen and G. A. Thouas, *Mater. Sci. Eng. R Reports*, 2015, **87**, 1–57.
- 9 J. C. Banwart, M. A. Asher and R. S. Hassanein, *Spine.*, 1995, **20**, 1055–1060.
- 10 E. D. Arrington, W. J. Smith, H. G. Chambers, A. L. Bucknell and N. A. Davino, *Clin. Orthop. Relat. Res.*, 1996, **329**, 300–309.

- 11 D. Shi, *Introduction to Biomaterials*, CO-PUBLISHED WITH TSINGHUA UNIVERSITY PRESS, 2005.
- 12 S. H. Teoh, in *Engineering Materials for Biomedical Applications*, 2004, pp. 1-1-1–16.
- 13 R. Article, M. Kheirallah, H. Almeshaly and M. Kheirallah, *Int. J. Dent. Oral Sci. Int J Dent. Oral Sci*, 2016, **03**, 247–257.
- 14 L. L. Hench, *J. Am. Ceram. Soc.*, 1991, **74**, 1487–1510.
- 15 J. B. Park and R. S. Lakes, *Biomaterials : an introduction*, Springer, 2007.
- 16 S. Koutsopoulos, *J. Biomed. Mater. Res.*, 2002, **62**, 600–612.
- 17 H. Aoki, *Science and Medical Applications of Hydroxyapatite*, Ishiyaku Euroamerica, 1992.
- 18 S. Bierbaum, V. Hintze and D. Scharnweber, *Biomatter*, 2012, **2**, 132–141.
- 19 M. Al-Jawad, A. Steuwer, S. H. Kilcoyne, R. C. Shore, R. Cywinski and D. J. Wood, *Biomaterials*, 2007, **28**, 2908–2914.
- 20 K. Kandori, A. Fudo and T. Ishikawa, *Colloids Surfaces B Biointerfaces*, 2002, **24**, 145–153.
- 21 G. Kawachi, S. Sasaki, K. Nakahara, E. H. Ishida and K. Ioku, *Key Eng. Mater.*, 2006, **309–311**, 935–938.
- 22 Z. Zhuang and M. Aizawa, *J. Mater. Sci. Mater. Med.*, 2013, **24**, 1211–1216.
- 23 D. A. Puleo, *Biomaterials*, 1999, **20**, 2311–2321.
- 24 R. Z. Legeros and R. G. Craig, *J. Bone Miner. Res.*, 2009, **8**, S583–S596.
- 25 Z. Shi, X. Huang, Y. Cai, R. Tang and D. Yang, *Acta Biomater.*, 2009, **5**, 338–345.
- 26 E. Pepla, L. K. Besharat, G. Palaia, G. Tenore and G. Migliau, *Ann. Stomatol. (Roma)*, 2014, **5**, 108–14.
- 27 M. P. Ferraz, F. J. Monteiro and C. M. Manuel, *J. Appl. Biomater. Biomech.*, 2018, **2**, 74–80.
- 28 M. M. Stevens, *Mater. Today*, 2008, **11**, 18–25.
- 29 H. Shin, S. Jo and A. G. Mikos, *Biomaterials*, 2003, **24**, 4353–4364.
- 30 W. R. Walsh and N. Guzelsu, *Biomaterials*, 1994, **15**, 137–145.
- 31 R. Jugdaohsingh, *J. Nutr. Heal. Aging*, 2007, **11**, 99–110.
- 32 S. J. Whiting and H. H. Draper, *J. Nutr.*, 1981, **111**, 1721–1726.
- 33 W. J. Landis, D. D. Lee, J. T. Brenna, S. Chandra and G. H. Morrison, *Calcif. Tissue Int.*, 1986, **38**, 52–59.
- 34 E. M. Carlisle, *Ciba Found. Symp.*, 1986, **121**, 123–39.
- 35 E. M. Carlisle, *Science.*, 1972, **178**, 619–621.
- 36 M. Chirita, *J. Bionic Eng.*, 2008, **5**, 149–158.
- 37 I. R. Gibson, S. M. Best and W. Bonfield, *J. Biomed. Mater. Res.*, 1999, **44**, 422–428.

- 38 F. Balas, J. Pérez-Pariente and M. Vallet-Regí, *J. Biomed. Mater. Res. Part A*, 2003, **66A**, 364–375.
- 39 P. Saravanapavan and L. L. Hench, *J. Non. Cryst. Solids*, 2003, **318**, 1–13.
- 40 T. Kokubo, M. Shigematsu, Y. Nagashima, M. Tashiro, T. Nakamura, T. Yamamuro and S. Higashi, *Bull. Inst. Chem. Res.*, 1982, **60**, 260–268.
- 41 H. M. Kim, T. Himeno, T. Kokubo and T. Nakamura, *Biomaterials*, 2005, **26**, 4366–4373.
- 42 K. Nakata, T. Kubo, C. Numako, T. Onoki and A. Nakahira, *Mater. Trans.*, 2009, **50**, 1046–1049.
- 43 S. H. Kim, *Biomaterials*, 2003, **24**, 1389–1398.
- 44 A. M. Pietak, J. W. Reid, M. J. Stott and M. Sayer, *Biomaterials*, 2007, **28**, 4023–4032.
- 45 J. L. Xu and K. A. Khor, *J. Inorg. Biochem.*, 2007, **101**, 187–195.
- 46 D. R. Ulrich, in *Transformation of Organometallics into Common and Exotic Materials: Design and Activation*, Springer Netherlands, Dordrecht, 1988, pp. 207–235.
- 47 C. T. Kresge, M. E. Leonowicz, W. J. Roth, J. C. Vartuli and J. S. Beck, *Nature*, 1992, **359**, 710–712.
- 48 Y. Tsuneto, S. Toshio, K. Kazuyuki and K. Chuzo, *Bull. Chem. Soc. Jpn.*, 1990, **63**, 988–992.
- 49 M. Kruk, M. Jaroniec and A. Sayari, *Langmuir*, 1997, **13**, 6267–6273.
- 50 D. Zhao, J. Feng, Q. Huo, N. Melosh, G. H. Fredrickson, B. F. Chmelka and G. D. Stucky, *Science*, 1998, **279**, 548–552.
- 51 K. Schumacher, M. Grün and K. K. Unger, *Microporous Mesoporous Mater.*, 1999, **27**, 201–206.
- 52 H. Takahashi, B. Li, T. Sasaki, C. Miyazaki, T. Kajino and S. Inagaki, *Chem. Mater.*, 2000, **12**, 3301–3305.
- 53 I. I. Slowing, J. L. Vivero-Escoto, C. W. Wu and V. S. Y. Lin, *Adv. Drug Deliv. Rev.*, 2008, **60**, 1278–1288.
- 54 M. Grün, I. Lauer and K. K. Unger, *Adv. Mater.*, 1997, **9**, 254–257.
- 55 A. Sugawara-Narutaki, *Bull. Chem. Soc. Japan*, 2017, **52**, 15–19.
- 56 A. Borówka and A. Szcze, 2011, **65**, 175–178.
- 57 S. Ng, J. Guo, J. Ma and S. C. J. Loo, *Acta Biomater.*, 2010, **6**, 3772–3781.
- 58 L. S. Mendes, S. Saska, M. A. U. Martines and R. Marchetto, *Mater. Sci. Eng. C*, 2013, **33**, 4427–4434.
- 59 A. Sousa, K. C. Souza and E. M. B. Sousa, *Acta Biomater.*, 2008, **4**, 671–679.
- 60 Z. Song, Y. Liu, J. Shi, T. Ma, Z. Zhang, H. Ma and S. Cao, *Mater. Sci. Eng. C*, 2018, **83**, 90–98.
- 61 K. Inumaru, M. Yasui, T. Kasahara, K. Yamaguchi, A. Yasuda and S. Yamanaka, *J. Mater. Chem.*, 2011, **21**, 12110–12116.

- 62 S. Yamada, M. Nishikawa and M. Tagaya, *Mater. Lett.*, 2018, **211**, 220–224.
- 63 R. Ma, S. Tang, H. Tan, J. Qian, W. Lin, Y. Wang, C. Liu, J. Wei and T. Tang, *ACS Appl. Mater. Interfaces*, 2014, **6**, 12214–12225.
- 64 M. Tagaya, T. Ikoma, N. Hanagata and J. Tanaka, *Mater. Express*, 2012, **2**, 1–22.
- 65 B. Kasemo, *Surf. Sci.*, 2002, **500**, 656–677.
- 66 C. T. Laurencin, M. A. Attawia, L. Q. Lu, M. D. Borden, H. H. Lu, W. J. Gorum and J. R. Lieberman, *Biomaterials*, 2001, **22**, 1271–1277.
- 67 M. I. Alam, I. Asahina, K. Ohmamiuda and S. Enomoto, *J. Biomed. Mater. Res.*, 2001, **54**, 129–138.
- 68 H. Frauenfelder, P. W. Fenimore and B. H. McMahon, *Biophys. Chem.*, 2002, **98**, 35–48.
- 69 B. Bagchi, *Chem. Rev.*, 2005, **105**, 3197–3219.
- 70 J. Israelachvili and H. Wennerström, *Nature*, 1996, **379**, 219–225.
- 71 M. Tanaka and K. Sato, *Netsu Sokutei*, 2012, **39**, 151–157.
- 72 M. Tanaka, A. Mochizuki, T. Shiroya, T. Motomura, K. Shimura, M. Onishi and Y. Okahata, *Colloids Surfaces A Physicochem. Eng. Asp.*, 2002, **203**, 195–204.
- 73 M. Tanaka and A. Mochizuki, *J. Biomed. Mater. Res. - Part A*, 2004, **68**, 684–695.
- 74 M. Tanaka, T. Hayashi and S. Morita, *Polym. J.*, 2013, **45**, 701–710.
- 75 R. W. Michelmore and F. Franks, *Cryobiology*, 1982, **19**, 163–171.
- 76 M. Tanaka, T. Motomura, N. Ishii, K. Shimura, M. Onishi, A. Mochizuki and T. Hatakeyama, *Polym. Int.*, 2000, **49**, 1709–1713.
- 77 M. Tanaka, *J. Adhes. Soc. Japan*, 2015, **51**, 423–433.
- 78 T. Hoshiba, M. Nikaido and M. Tanaka, *Adv. Healthc. Mater.*, 2014, **3**, 775–784.
- 79 C. Bharti, N. Gulati, U. Nagaich and A. Pal, *Int. J. Pharm. Investig.*, 2015, **5**, 124.
- 80 S. Kittaka, S. Ishimaru, M. Kuranishi, T. Matsuda and T. Yamaguchi, *Phys. Chem. Chem. Phys.*, 2006, **8**, 3223.
- 81 S. Kittaka, K. Sou, T. Yamaguchi and K. Tozaki, *Phys. Chem. Chem. Phys.*, 2009, **11**, 8538.
- 82 A. Schreiber, I. Ketelsen and G. H. Findenegg, *Phys. Chem. Chem. Phys.*, 2001, **3**, 1185–1195.
- 83 J. Sjöström, J. Swenson, R. Bergman and S. Kittaka, *J. Chem. Phys.*, 2008, **128**, 154503.
- 84 M. Oguni, S. Maruyama, K. Wakabayashi and A. Nagoe, *Chem. - An Asian J.*, 2007, **2**, 514–520.
- 85 B. Siboulet, I. Charles and G. Montpellier, *J. Phys. Chem. B*, 2011, **115**, 7881–7886.
- 86 T. Kobashi, Y. Chai, I. Yamada, S. Yamada and M. Tagaya, *Mater. Chem. Phys.*, 2019, **227**, 134–137.
- 87 D. L. Childers, J. Corman, M. Edwards and J. J. Elser, *Bioscience*, 2011, **61**, 117–124.
- 88 W. F. Newman and M. W. Newman., *Arthritis Rheum.*, 1958, **1**, 473–474.

- 89 S. Yamada and M. Tagaya, *Mater. Lett.*, 2017, **209**, 441–445.
- 90 O. Tirosh, Y. Barenholz, J. Katzhendler and A. Priev, *Biophys. J.*, 1998, **74**, 1371–1379.
- 91 I. Sugiyama and Y. Sadzuka, *Drug Deliv. Syst.*, 2016, **31**, 275–282.
- 92 S. Schöttler, G. Becker, S. Winzen, T. Steinbach, K. Mohr, K. Landfester, V. Mailänder and F. R. Wurm, *Nat. Nanotechnol.*, 2016, **11**, 372–377.
- 93 B. Thierry, L. Zimmer, S. McNiven, K. Finnie, C. Barbé and H. J. Griesser, *Langmuir*, 2008, **24**, 8143–8150.
- 94 T. J. Daou, L. Li, P. Reiss, V. Josserand and I. Texier, *Langmuir*, 2009, **25**, 3040–3044.
- 95 T. Sekine, S. Asatyas, T. Nyu, G. Lkhamsuren, A. Tsunoi, C. Sato, S. Morita, M. Tanaka and T. Hayashi, *Hyomen Kagaku*, 2015, **36**, 424–429.
- 96 J. V. Jokerst, T. Lobovkina, R. N. Zare and S. S. Gambhir, *Nanomedicine*, 2011, **6**, 715–728.
- 97 A. M. Ferreira, P. Gentile, V. Chiono and G. Ciardelli, *Acta Biomater.*, 2012, **8**, 3191–3200.
- 98 M. G. Patino, M. E. Neiders, S. Andreana, B. Noble and R. E. Cohen, *Implant Dent.*, 2002, **11**, 280–285.
- 99 K. Gelse, E. Pöschl and T. Aigner, *Adv. Drug Deliv. Rev.*, 2003, **55**, 1531–1546.
- 100 B. Brodsky and E. F. Eikenberry, in *Methods in Enzymology*, 1982, vol. 82, pp. 127–174.
- 101 M. J. Olszta, X. Cheng, S. S. Jee, R. Kumar, Y. Y. Kim, M. J. Kaufman, E. P. Douglas and L. B. Gower, *Mater. Sci. Eng. R Reports*, 2007, **58**, 77–116.
- 102 B. Brodsky and J. A. M. Ramshaw, *Matrix Biol.*, 1997, **15**, 545–554.
- 103 P. Fratzl, *Curr. Opin. Colloid Interface Sci.*, 2003, **8**, 32–39.
- 104 J. Jokinen, E. Dadu, P. Nykvist, J. Käpylä, D. J. White, J. Ivaska, P. Vehviläinen, H. Reunanen, H. Larjava, L. Häkkinen and J. Heino, *J. Biol. Chem.*, 2004, **279**, 31956–31963.
- 105 M. Van Der Rest and R. Garrone, *FASEB J.*, 1991, **5**, 2814–2823.
- 106 D. J. Prockop and K. I. Kivirikko, *Annu. Rev. Biochem.*, 1995, **64**, 403–434.
- 107 N. Kuznetsova and S. Leikin, *J. Biol. Chem.*, 1999, **274**, 36083–36088.
- 108 L. J. Zhang, X. S. Feng, H. G. Liu, D. J. Qian, L. Zhang, X. L. Yu and F. Z. Cui, *Mater. Lett.*, 2004, **58**, 719–722.
- 109 B. Basu, in *Biomaterials for Musculoskeletal Regeneration: Concepts*, Springer Singapore, Singapore, 2017, pp. 45–85.
- 110 R. H. Barckhaus and H. J. Höhling, *Cell Tissue Res.*, 1978, **186**, 541–549.
- 111 A. L. Boskey, *Connect. Tissue Res.*, 2003, **44**, 5–9.
- 112 J. Mahamid, A. Sharir, D. Gur, E. Zelzer, L. Addadi and S. Weiner, *J. Struct. Biol.*, 2011, **174**, 527–535.
- 113 M. J. Glimcher, *Philos. Trans. R. Soc. London. B, Biol. Sci.*, 1984, **304**, 479–508.
- 114 A. Veis and A. Perry, *Biochemistry*, 1967, **6**, 2409–2416.

- 115 S. Y. Ali, S. W. Sajdera and H. C. Anderson, *Proc. Natl. Acad. Sci.*, 1970, **67**, 1513–1520.
- 116 H. C. Anderson, R. Garimella and S. E. Tague, *Front. Biosci.*, 2005, **10**, 822–837.
- 117 J. Mahamid, A. Sharir, L. Addadi and S. Weiner, *Proc. Natl. Acad. Sci.*, 2008, **105**, 12748–12753.
- 118 J. Mahamid, B. Aichmayer, E. Shimoni, R. Ziblat, C. Li, S. Siegel, O. Paris, P. Fratzl, S. Weiner and L. Addadi, *Proc. Natl. Acad. Sci. U. S. A.*, 2010, **107**, 6316–6321.
- 119 S. C. Marks and P. R. Odgren, in *Principles of Bone Biology*, Elsevier, 2002, pp. 3–15.
- 120 A. J. Salgado, O. P. Coutinho and R. L. Reis, *Macromol. Biosci.*, 2004, **4**, 743–765.
- 121 D. A. Wahl and J. T. Czernuszka, *Eur. Cells Mater.*, 2006, **11**, 43–56.
- 122 R. Z. Wang, F. Z. Cui, H. B. Lu, H. B. Wen, C. L. Ma and H. D. Li, *J. Mater. Sci. Lett.*, 1995, **14**, 490–492.
- 123 C. M. Serre, M. Papillard, P. Chavassieux and G. Boivin, *Biomaterials*, 1993, **14**, 97–106.
- 124 J. Xie, M. J. Baumann and L. R. McCabe, *J. Biomed. Mater. Res. - Part A*, 2004, **71**, 108–117.
- 125 K. D. Johnson, K. E. Frierson, T. S. Keller, C. Cook, R. Scheinberg, J. Zerwekh, L. Meyers and M. F. Sciadini, *J. Orthop. Res.*, 1996, **14**, 351–369.
- 126 S. F. El-Amin, H. H. Lu, Y. Khan, J. Burems, J. Mitchell, R. S. Tuan and C. T. Laurencin, *Biomaterials*, 2003, **24**, 1213–1221.
- 127 A. Salis, M. Boström, L. Medda, F. Cugia, B. Barse, D. F. Parsons, B. W. Ninham and M. Monduzzi, *Langmuir*, 2011, **27**, 11597–11604.
- 128 X. M. He and D. C. Carter, *Nature*, 1992, **358**, 209–215.
- 129 Y. L. Jeyachandran, E. Mielczarski, B. Rai and J. A. Mielczarski, *Langmuir*, 2009, **25**, 11614–11620.
- 130 M. Yamaguchi, A. Igarashi, H. Misawa and Y. Tsurusaki, *J. Cell. Biochem.*, 2003, **89**, 356–363.
- 131 K. Ishida, N. Sawada and M. Yamaguchi, *Int. J. Mol. Med.*, 2004, **14**, 891–895.
- 132 K. Ishida and M. Yamaguchi, *Int. J. Mol. Med.*, 2005, **16**, 689–694.
- 133 F. Afshinnia and S. Pennathur, *J. Clin. Endocrinol. Metab.*, 2016, **101**, 2468–2474.
- 134 T. Klára, L. Csöngé, G. Janositz, Z. Csernátóny and Z. Lacza, *Cell Tissue Bank.*, 2014, **15**, 89–97.
- 135 K. Schandl, D. B. Horváthy, A. Doros, E. Majzik, C. M. Schwarz, L. Csöngé, G. Abkarovits, L. Bucsi and Z. Lacza, *Int. Orthop.*, 2016, **40**, 2097–2104.
- 136 M. T. Bernards, C. Qin and S. Jiang, *Colloids Surfaces B Biointerfaces*, 2008, **64**, 236–247.
- 137 B. Mueller, D. Koch, R. Lutz, K. A. Schlegel, L. Treccani and K. Rezwani, *Mater. Sci. Eng. C*, 2014, **42**, 137–145.

- 138 G. Rolla, J. E. Ciardi and W. H. Bowen, *Surf. Colloid Phenom. Oral Cavity; Methodol. Asp.*, 1982, 203–210.
- 139 K. Kandori, T. Shimizu, A. Yasukawa and T. Ishikawa, *Colloids Surfaces B Biointerfaces*, 1995, **5**, 81–87.
- 140 Q. Yang, Y. Zhang, M. Liu, M. Ye, Y. Zhang and S. Yao, *Anal. Chim. Acta*, 2007, **597**, 58–66.
- 141 A. Monkawa, T. Ikoma, S. Yunoki, T. Yoshioka, J. Tanaka, D. Chakarov and B. Kasemo, *Biomaterials*, 2006, **27**, 5748–5754.
- 142 D. C. Lee, P. I. Haris, D. Chapman and R. C. Mitchell, *Biochemistry*, 2005, **29**, 9185–9193.
- 143 C. Gullekson, L. Lucas, K. Hewitt and L. Kreplak, *Biophys. J.*, 2011, **100**, 1837–1845.
- 144 S. Deshmukh, A. Dive, R. Moharil and P. Munde, *J. Oral Maxillofac. Pathol.*, 2016, **20**, 276.
- 145 W. Traub, A. Yonath and D. M. Segal, *Nature*, 1969, **221**, 914–917.
- 146 T. J. Wess, A. P. Hammersley, L. Wess and A. Miller, *J. Mol. Biol.*, 1998, **275**, 255–267.

Chapter 2

Modification of Hydroxyapatite Particles with Tetraethoxysilane and Poly(ethylene glycol) and Evaluation of Their Hydration States and Collagen Fibrillation

Chapter 2

Modification of Hydroxyapatite Particles with Tetraethoxysilane and Poly(ethylene glycol) and Evaluation of Their Hydration States and Collagen Fibrillation

2.1 Introduction

The relationship between osteoblasts and osteoclasts, proteins, inorganic ions plays important role in bone regeneration.^{1,2} Bone regeneration is known to be achieved by the complex combined reactions such as the cell-released inorganic ions as well as the cell activation mediated by the protein interactions, particularly, by collagen (Col) molecules.¹ Generally, Col molecules are released by osteoblasts, and spontaneously are fibrillated and aligned to be Col fibril. Then, hydroxyapatite (HA, $\text{Ca}_{10}(\text{PO}_4)_6(\text{OH})_2$) nanocrystals are newly precipitated from the inorganic ions in the hole zone of the aligned to be Col fibrils.³ Thus, the Col fibrils can be regarded as an important matrix for initiating and propagating the HA mineralization.^{4,5} In order to precisely mimic the biological reactions in the bone regeneration, we suggested that focusing on the hydration waters at the interfaces between the biological inorganic components (i.e., bone-like HA) and the Col fibrillation states is very important. Although the simple hybridization reaction between the HA and Col has widely been reported, the interfacial interaction between Col and hydration water, and interfacial structure have not been investigated so far. The main inorganic component in bone is HA,⁶ which has been widely used as the bone filling material because of high biocompatibility.^{7,8} As the important point for mimicking the biological reactions, the fact is that the adult body contains the Si components and the components interacted with living bone are the ion states at the concentration of 36 ppm.^{9,10} Although the existence state of the Si

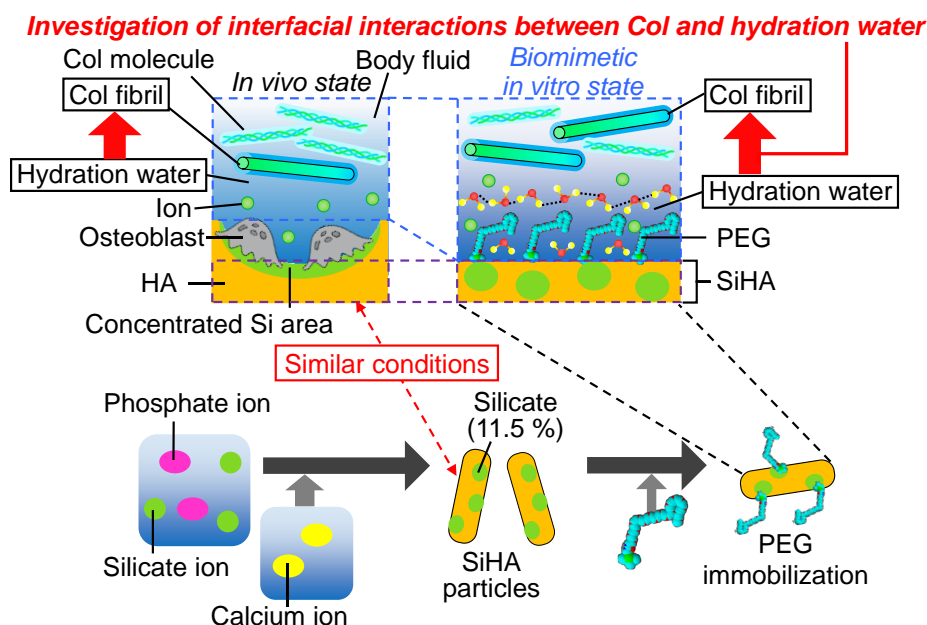
components as well as the role in the living bone has not been clarified, the possible state as silicate was suggested by an ion microscope analysis,¹¹ suggesting the importance of the study regarding the silicate for the bone regeneration. Moreover, it has been reported that the Si-elemental concentration dramatically increased 50 times at the living bone fracture part,¹² and the Si elements induced the angiogenesis and osteogenesis.¹³ Accordingly, the interactions of calcium phosphate (e.g., HA) with silicate were investigated.^{14,15} For example, the bulk bodies of HA–Wollastonite glass and Bioglass® were practically used for the bone regeneration.^{16–18} The HA particles coated with silicate layers^{19–21} and the silicate-containing HA (SiHA)^{22–25} were synthesized and evaluated. In the SiHA particles, the PO_4^{3-} in the HA structure was mainly replaced with silicate ion (SiO_4^{4-}) and simultaneously some amorphous SiO_2 was segregated.²⁶ However, the high temperature calcination for efficient substitution in the SiHA particles was required after wet synthetic processes.²⁷ For achieving the biomimetics, it is necessary to avoid the high temperature calcination process in the synthesis. Moreover, the interaction of water molecules with SiHA particles should be investigated to further clarify the reactions with the Col fibril matrix.

In order to investigate the SiHA-related bone regeneration, it is necessary to consider the cellular behavior on contact with the particles. Here, the following processes have been suggested after the implantation of bioceramic particles into the living body.^{28,29} First, ions and water molecules reach the bioceramic particle surfaces. Then, the substances interact and bound together depending on the surface properties, and the hydration layer is formed in the living body. Second, a protein adlayer is formed by its recognition of the hydration layer state. Finally, cell adhesion and extension are performed by recognizing the hydration layer states and protein denaturation degree. For controlling the adhered cell behavior, it is necessary to investigate the hydration layer states on the particle surfaces. In fact, the HA particles have been reported to have the hydration water at least $35 \text{ mM} \cdot (\text{g of HA})^{-1}$ on the particle surfaces.³⁰ However, there were few reports on the hydration layer states on bioceramics. In the biopolymer fields, the hydration layer structures can be dominantly attributed to three water components of free, intermediate and nonfreezing states.³¹ The hydration layers can be formed and deposited on the polymers in order of nonfreezing water, intermediate water, free water and bulk water,³² indicating the strongly interactive water molecules close to the surfaces. For achieving the steric conformation (i.e., suppressing the denaturation) of the adsorbed proteins, it is necessary to investigate the hydration layer states on the bioceramics.^{33,34} The various interactions such as intermolecular water–water and water–ions were operative in the hydration layers,³⁵ suggesting that the bioceramic hydration layers can directly contribute to the adsorbed protein conformation.^{31,36,37} In our previous reports, the hydrogen bonding formation among the water molecules on the nanostructured bioceramics was not disrupted very much by the interfacial interactions and was not strongly constrained by the material surfaces.^{38,39} For achieving the biomimetics, it is important to effectively control of

the hydration layer structures on the particles, which can be achieved by the immobilization of polymer chains.⁴⁰ For example, poly(ethylene glycol) (PEG) can interact with the water molecules to form the specific hydration layers.^{41–43} Thus, it is considered that the PEG-immobilized SiHA particles can control the hydration layer states and optimize the Col fibrillation degrees. In particular, the PEG can enclose the water molecules to form the PEG–interactive layers.^{41,44} In the PEG–interactive layers, the hydrogen bonds among the water molecules was formed and stabilized with PEG through the irregular interactions. Moreover, the PEG-interactive layers induce the specific protein adsorption and denaturation. Therefore, the PEG immobilized layer formed on the bioceramic surfaces can effectively change the hydrogen bonding states of the water molecules, which will subsequently affect the protein adsorption layer state.

Col is the most abundant protein in vivo. More than one-third of the whole body protein content consists of Col.^{2,45} The Col molecules in extracellular matrix were spontaneously aligned and fibrillated.^{4,5} Therefore, when synthesizing bioceramic particles for bone regeneration, it is important to control the bioceramic surface states in order to promote the Col fibrillation.⁴⁶ From the background, the composites of HA and Col can be synthesized, which were expected to replace bone defects because of their biocompatibility and better osteoconductive properties.^{47–49} As a scaffolds, the composites also had the excellent biodegradability and osteogenic cell adhesion ability.^{50,51} Thus, the investigation of HA and Col composite structure is useful for making better bioceramic particles to repair the bone defect. The Col molecule is fibrilized through the intermolecular aldol cross–links.^{52–54} At the ends of adjacent Col fibrils, the lysine contained in the α chain and the lysine hydroxide in the α chain of another Col fibril are aldol-bonded (crosslinked) by lysyl oxidase.⁵⁵ Since the adsorption states of the proteins are affected by the hydration layer states, it is possible that the hydration layer states involve in the formation of Col fibrils in the present study. In other words, it is necessary to approach the question how much the hydration layer state correlates with the fibril formation. However, there was no studies about the hydration layer on the surface of bioceramics. Therefore, it was proposed here to realize the hydration layer states that can promote the Col fibrillation using the PEG-immobilized SiHA particles.

In this study, the SiHA particles were synthesized, and the particles were immobilized by PEG (**Scheme 2-1**). The hydration layer and Col adlayer states on the particles were investigated. The relationship between the hydration layer and Col adlayer states was evaluated to suggest the importance of the hydration layer for the Col fibrillation.



Scheme 2-1. Outline of this study for preparing the SiHA particles and investigating the interfacial interactions between the hydration layer and the Col adlayers for effectively forming the Col fibrils.

2.2 Experimental Section

2.2.1 Chemicals

Dipotassium hydrogen phosphate (K_2HPO_4), 25 wt% of tetramethylammonium hydroxide (TMAOH, $C_4H_{13}NO$), calcium chloride dehydrate ($CaCl_2 \cdot 2H_2O$) and ethanol (99.5 vol%) were purchased from Wako Chemical Co. Ltd. The type I Col from tilapia fish skin was purchased from Nippi. Inc. The type I Col was diluted with acetic acid (5 mM) aqueous solution to be the Col concentration at 3 mg/mL. According to the information provided by the manufacturer, the denaturation temperature of Col is known to be 30–36 °C. Tetraethoxysilane (TEOS, $Si(OCH_2CH_3)_4$) was purchased from Tokyo Chemical Industry Co., Ltd. PEG-silane (PEG) ($CH_3O(CH_2CH_2O)_nC_6H_{12}N_2OSi(OC_2H_5)_3$, $n=16$) was purchased from Creative PEGWorks. Dulbecco's phosphate-buffered saline (PBS) without calcium and magnesium was purchased from DS pharma biomedical Co., Ltd. Silicon (100) wafer (size: 2.4 cm \times 2.4 cm, p-type, resistivity: 16.1–18.7 Ω) was purchased from Mitsubishi Materials Trading Co., Ltd. All of the chemicals were used as received without further purification.

2.2.2 Synthesis of Silicate-Containing Hydroxyapatite Particles and Their Poly(ethylene glycol) Immobilization

4.61 mmol of K_2HPO_4 was dissolved in 40.0 mL of ultrapure water. 20.0 mL of ultrapure water dissolving $CaCl_2 \cdot 2H_2O$ (10.0 mmol) was added into the K_2HPO_4 solution at the drop rate

of 1.0 mL/min. Then, 1.39 mmol of TEOS was added into the solution, and the solution was stirred at 60 °C for 24 h. The pH value was adjusted to be 13 using TMAOH, and the solution was stirred at 80 °C for 3 h. The white-colored precipitation was centrifuged, washed by ultrapure water (once) and ethanol (once). Then, the solid product was dispersed in ethanol and then washed by ethanol 3 times to obtain the completely-dispersed particles in ethanol, which was partially used for the electrophoretic deposition described later. The dispersion was partially centrifuged and dried at 100 °C for 12 h and 250 °C for 6 h and the solid products were donated as SiHA. The particles synthesized without TEOS were denoted as HA.

PEG was dissolved in 40 mL of ethanol at the theoretical molecular occupancy of 25 % (conc. 0.62mM), 50 % (conc. 1.23 mM) and 100 % (conc. 2.47 mM) for 400 mg of SiHA particles, which were pre-dried at 100 °C for 2 h, added into the solution and stirred at 37 °C for 2 h. The particles were centrifuged, washed by ethanol once, and were dried at 65 °C for 12 h and 120 °C for 6 h. The resulting particles with the molecular occupancy of PEG at 25 %, 50 % and 100 % were donated as SiHA-P25, SiHA-P50 and SiHA-P100, respectively.

2.2.3 Characterization of the Particles

The evaluation of the chemical bonding states of P atoms in the particles were performed by a solid-state NMR spectroscopy (Avance 300wbs, BRUKER Co., Ltd.) with a dipolar decoupling magic angle spinning (DD-MAS) method. This measurement was performed under 7.05 T wide-bore magnet system using a standard Bruker 7-mm-MAS-probe. At this magnetic field, the frequency and rotation speed were 59.62 MHz. The chemical shift in the solid state ³¹P-NMR spectra was adjusted by referencing the peak position of ammonium dihydrogen phosphate at an accumulation time of 4.

X-ray diffraction (XRD) patterns were recorded with an X-ray diffractometer (Smart Lab, Rigaku Co., Ltd.) and were measured with an X-ray source of CuK α line ($\lambda = 0.15418$ nm), a voltage/current of 40 kV/30 mA, a scan speed of 1.0 °/min and a sampling width of 0.01°. The crystallite sizes were calculated from full width at half maximum (FWHM) of the 002 and 300 diffraction peaks using the following Scherrer equation (2-1).

$$D = \frac{K\lambda}{\beta \cos\theta} \quad (2-1)$$

where D is the crystallite size, K is the shape function value (0.9), λ is the radiation wavelength, β is the FWHM, and θ is the angle of incidence. Lattice parameters were determined by Rietveld refinement of the diffraction profiles with a PDXL2 program (Rigaku Co., Ltd.). In the calculation of hexagonal cell parameters (i.e., lattice constants of a and c) in the HA crystallographic system, the relationship between the distance (d -spacing) between two adjacent net planes and the ($h k l$) Miller indices in the diffraction planes^{56,57} as the following equation (2-2) was used.

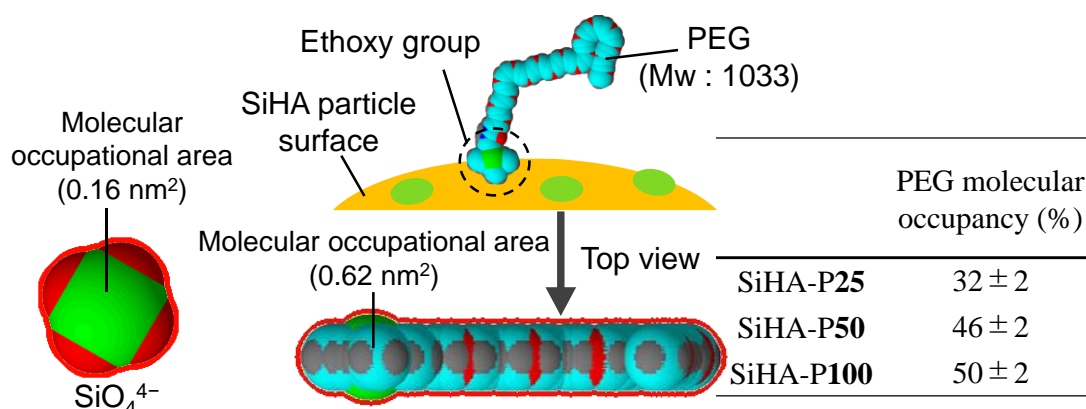
$$d = \frac{1}{\sqrt{\frac{4h^2 + hk + k^2}{3a^2} + \frac{l^2}{c^2}}} \quad (2-2)$$

The morphologies were observed using a field emission scanning electron microscope (FE-SEM: SU8000, Hitachi High-Technologies, Japan) at an accelerating voltage of 5 kV and current of 10 mA. 30 particles obtained from the image were measured, and the long and short axis lengths of the particles were calculated. Transmission electron microscope (TEM) images for the observation of particle interfaces were taken with a JEM-1400 (JEOL Co., Ltd.) at an accelerating voltage of 120 kV. The particle shapes were observed on a carbon-coated Cu grid.

The evaluation of the chemical bonding states of the Si atoms in the particles were performed by a solid-state NMR spectroscopy (AS300, BRUKER Co., Ltd.) with a dipolar decoupling magic angle spinning (DD-MAS) method. This measurement was performed under 7.05 T wide-bore magnet system using a standard Bruker 7-mm-MAS-probe. At this magnetic field, the frequency and cumulative number were 59.62 MHz and 1000–5000 times, respectively. The chemical shift was adjusted by referencing the peak position of tetramethylsilane (TMS) at the accumulation times of 1000. The solid state ^{29}Si -NMR spectra was deconvoluted into four components of Q_0 (i.e., SiO_4^{4-} substituted with HA crystalline lattice or spherical silicate clusters in HA structure) at -73 ± 2 ppm,^{58,59} Q_2 (i.e., two Si–O–Si and two Si–OH bonds) at -95 ± 2 ppm,⁶⁰ Q_3 (i.e., three Si–O–Si and one Si–OH bonds) at -100 ± 2 ppm and Q_4 (i.e., four Si–O–Si bonds) at -111 ± 2 ppm. Here, the exact locations of the silicate entities inside or outside the HAp structure can be determined by the NMR spectra, and the silicon atom state incorporated into the HAp lattice indicated the form of Q_0 (SiO_4^{4-}),⁵⁸ which was related with the excess hydrogen or a OH vacancy of HA lattice.⁶¹

The Si concentration (wt%) and SiO_4^{4-} molecular occupancy (%) were calculated by an X-ray fluorescence analysis (XRF: Rigaku ZSX Primus II). The fundamental parameter method was carried out using a semi quantitative analysis software (EZ Scan Program, Rigaku Co., Ltd.). Q_2 , Q_3 and Q_4 were defined as existing on the HA particle surfaces, and calculated the ratio of adsorption states on the particles (i.e., coverage rate (%)). Here, all the components were defined as the individual SiO_4^{4-} unit to calculate the molecular occupational area. The schematic diagram and molecular occupational area of SiO_4^{4-} was shown in **ESM, Scheme S1**. ACD/ChemSketch (Advanced Chemistry Development Inc.) was used for drawing the SiO_4^{4-} molecule and the molecular occupational area was calculated as 0.16 nm^2 . Then, the BET surface area was determined using a nitrogen (N_2) adsorption and desorption instrument (BELSORP-mini, MicrotracBEL Co., Ltd.). The SiHA particles were pre-treated at $120 \text{ }^\circ\text{C}$ for 2 h under vacuum using BELPREP-vac II, Microtrac Bell Co., Ltd. As a result, the BET surface area of the SiHA particles was $91.5 \text{ m}^2/\text{g}$. When the SiO_4^{4-} molecules were adsorbed on the particles at the monolayer-state, the molecular occupancy of SiO_4^{4-} on the particles (%) was calculated by dividing the molecular occupational area (0.16 nm^2) by the BET surface area.

The resultant PEG molecular occupancy was calculated from the Si concentration in the SiHA particles measured by an XRF. Here, the Si concentration in the SiHA particles was subtracted from that in the PEG-immobilized particles. As the same procedure as the case in SiO_4^{4-} , the PEG molecular occupancy was calculated by dividing the molecular occupational area of PEG by the BET surface area. Since the PEG has very flexible structure and molecular occupational area in aqueous solution, the molecular occupational area in air was used for convenience. Here, the molecular occupational area in the top view was calculated as 0.62 nm^2 in **Scheme 2-2**. The bond lengths and angles were standardized while the relative dislocations of all the inter-bonded atoms and fragments in the drawn structure were minimally changed in the schematic diagram. The resultant PEG molecular occupancy (%) and adsorption amount of hydration and Col ($\mu\text{g}/\text{cm}^2$) on the particles. PEG molecular occupancy was 32–50 % with increasing the added amount.



Scheme 2-2. Schematic diagram and molecular occupational area of SiO_4^{4-} and PEG on the particle. The molecular occupational areas were used to calculate the coverage rate (%). The table indicate resultant PEG molecular occupancy (%) on the particles.

2.2.4 Fabrication of Silicate-Containing-Hydroxyapatite Particle Films and the Poly(ethylene glycol) Immobilization

The SiHA particle films were obtained as follows. The SiHA particles dispersed in ethanol at the concentration of 2 wt% were deposited on the Au sensor (QSensor QSX 301 Gold, Biolin Scientific AB) by an electrophoretic deposition. The Au sensor and aluminium foil plate were used as the working and counter electrodes, respectively. The Au sensor was cleaned by an exposure to UV/OZONE (ASUMI GIKEN, Limited, ASM401N) for 3 min. Then, the Au sensor was immersed in the dispersion, and a DC voltage of 100 V at the distance of 1 cm between the electrodes was applied. The surplus particles were removed by ultrasonic treatment (40 kHz, 65 W) for 3 min in ethanol and washed by ethanol.

The SiHA particle films were immobilized by PEG. The films were dried at $100 \text{ }^\circ\text{C}$ for 2 h.

Then, the PEG-silane was dispersed in 33.25 μL of ethanol at the molecular occupancy of 25 %, 50 % and 100 % for the SiHA particles of films, which corresponded to the experiment of the powder state, and the solution was dropped on the films. The circumference of the films were surrounded by an O-ring to prevent the solution from turning to the back side. After the reaction, the films were dried at 37 $^{\circ}\text{C}$ for 2 h. Then, the films were dried at 120 $^{\circ}\text{C}$ for 6 h.

2.2.5 Basic Characterization of the Particle Films

The deposited weight of the particle films on the Au sensors was measured in air using the Quartz Crystal Microbalance with Dissipation (QCM-D, Qsense, Biolin scientific) technique. The deposited amount ($\mu\text{g}/\text{cm}^2$) change was calculated by the Sauerbrey equation (2-3).⁶²

$$\Delta f = \frac{-2\Delta m f_0^2 n}{A\sqrt{\mu\rho}} \quad (2-3)$$

where Δf is the frequency shift of the quartz, f_0 is the fundamental frequency, A is metallic electrode area on the quartz, μ is elasticity of quartz (2.95×10^{11} dyn/cm²), ρ is density of quartz (2.65 g/cm³), Δm is deposited weight of the particle films and n is the overtone number ($n = 5$). Then, the deposited particle films on the Au sensors were dried at 65 $^{\circ}\text{C}$ for 12 h and 250 $^{\circ}\text{C}$ for 6 h.

The surface morphologies for the Au sensors were analyzed in air using atomic force microscopy (AFM: Nanocute, SII Investments, Inc.) in an observation area of 1×1 μm^2 (**Figure 2-2**). The surface roughness was calculated using the root mean square (R_{ms}) value in the height profiles of the topographic images. The SiHA particle films were also measured by the same method. 30 particles obtained from the image were measured, and the long and short axis lengths of the particles were calculated.

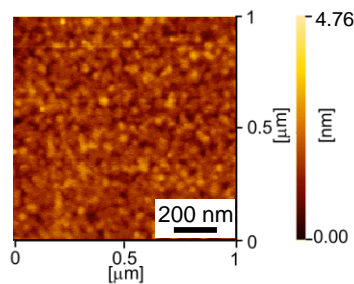


Figure 2-2. AFM topographic image of the Au substrate (i.e., QCM-D Au sensor). The R_{ms} value was 3.8 nm.

2.2.6 Formation of Hydration Layers and Collagen Adlayers on the Particle Surfaces

In order to evaluate the hydration layer, the particles were dispersed at the particle

concentration of 1.0 mg/mL in PBS (pH=7.4). The particles were stirred at 37 °C for 2.5 h. After stabilizing the hydration, the particles were centrifuged and washed by an ultrapure water in which the pH was controlled at 7.4, and freeze-dried for 12 h. Here, the FT-IR spectra were measured before and after the freeze-drying to evaluate the difference in the hydration layer states by the drying. The particles coated on the silicon (100) wafer were measured by the FT-IR transmittance method described later.

To evaluate the Col adlayers, the Col molecules were dispersed in PBS (pH=7.4) at the concentration of 50 µg/mL. Then, the particles were dispersed in the solution at the particle concentration of 1.0 mg/mL and stirred at 37 °C for 2.5 h. After the reaction, the solids were centrifuged and washed by a 70 vol% ethanol/water solution, and freeze-dried for 12 h. In general, the conversion of Col molecules to gelatin state is related to the condition at the temperature more than 75 °C, or the gradual changing procedure from acidic to neutral condition at physiological temperature. Accordingly, the conditions were eliminated in this experiment to prevent the Col gelatinization.

2.2.7 FT-IR Spectral Deconvolutions for Analyzing the Hydration States

The hydration layer structures on the particles were investigated by the Fourier transform infrared spectrometer (FT-IR, FT/IR-4600, JASCO Co., Ltd.) spectral deconvolution technique at the wavenumber regions between 3850–2800 cm⁻¹ under the accumulation times of 128 and the resolution of 1 cm⁻¹. The spectra were recorded after subtracting a spectrum of pristine KBr as the background. The diffuse reflection method was applied for obtaining the transmittance spectra and then was converted to the absorbance based Kubelka-Munk function. In particular, the O–H stretching band broadened by Fermi resonance was deconvoluted into three components of (I) 3200 ± 20 cm⁻¹, (II) 3400 ± 20 cm⁻¹ and (III) 3600 ± 20 cm⁻¹, belonging to (I) free, (II) intermediate and (III) nonfreezing water molecules,³¹ respectively. This deconvolution was performed by fitting with the Gaussian function, and has been examined by our previous papers.^{38,39,63} For evaluating the difference in the hydration layer states by the drying, the spectra before and after freeze-drying are shown in the **Figure 2-2**. When the FT-IR spectra of the SiHA and SiHA-P100 particles before and after drying were measured, no significant change was observed with a residual errors less than 9 % in the spectral difference. From the results, the FT-IR spectra after the freeze-drying were used for the evaluation and discussion of this study. Furthermore, (IV) N–H stretching vibration of Col (3300 ± 20 cm⁻¹) due to the attribution of the Col adsorbed particles was added into the spectral deconvolution after the Col adsorption. The three component hydration states of the Col adsorbed particles in addition to the existence of the N–H stretching vibration of Col were discussed.

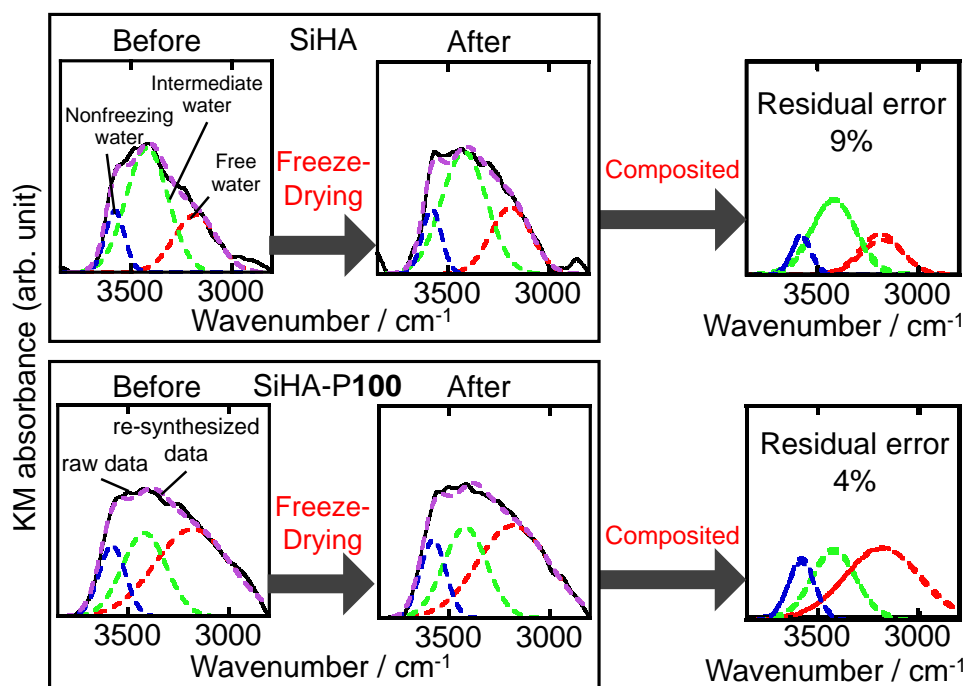


Figure 2-2. FT-IR spectral deconvolution results of three hydration layers formed on the particles before and after freeze-drying.

In order to clarify the detailed hydration layer structures and hydroxy group in HA of the particles, the spectra were deconvoluted into six components. In particular, the O–H stretching band was deconvoluted into six components of (1) $3190 \pm 20 \text{ cm}^{-1}$, (2) $3260 \pm 20 \text{ cm}^{-1}$, (3) $3410 \pm 20 \text{ cm}^{-1}$, (4) $3460 \pm 20 \text{ cm}^{-1}$, (5) $3600 \pm 20 \text{ cm}^{-1}$ and (6) $3571 \pm 1 \text{ cm}^{-1}$, belonging to “(1) asymmetric O–H stretching vibration between water molecules”,⁶⁴ “(2) O–H bending vibration of water molecules”,⁶⁵ “(3) symmetric O–H stretching vibration of water molecules”,⁶⁶ “(4) stretching and bending O–H vibration of water on Si–OH”,^{64,67–69} “(5) hydrogen bonded stretching O–H vibration of water molecules and stretching O–H vibration of water on Si–OH”,^{70–72} and “(6) structural OH[−] groups of HA,⁷³ respectively, which were tabled in the **Table 2-1**. The component ratio of (7) N–H stretching vibration of Col was considered using the results of the deconvolution at the three component system mentioned above. In the deconvolution, the vibrations derived from the liquid (i.e., hydration layer structures) and solid (i.e., hydroxy group in HA) states were deconvoluted by the Pseudo-Voigt and Gaussian functions, respectively, using the SOLVER option in the software (Excel 2013). In the SOLVER calculation, the generalized reduced gradient method was used until all the constraints and optimization conditions were satisfied, and has been examined in our previous papers.^{38,63} Here, all the residual values by the deconvolutions were less than 5.2%. In the exception of the N–H stretching vibration, the assignments of the deconvolution of three and six components were referred to the techniques of the polymer research field³¹ and the absorption bands of silicate and HA^{64–73}, respectively.

Table 2-1. Assignments of the six water-interactive states formed on the particles.

■ (1)	Asymmetric O–H stretching vibration between water molecules	Free water
■ (2)	O–H bending vibration of water molecules	
■ (3)	Symmetric O–H stretching vibration of water molecules	Intermediate water
■ (4)	Stretching and bending O–H vibration of water on Si–OH	
■ (5)	Hydrogen-bonded stretching O–H vibration of water molecules Stretching O–H vibration of water on Si–OH	Nonfreezing water
■ (6)	Structural OH ⁻ groups of HA	–
■ (7)	N–H stretching vibration of Col	–

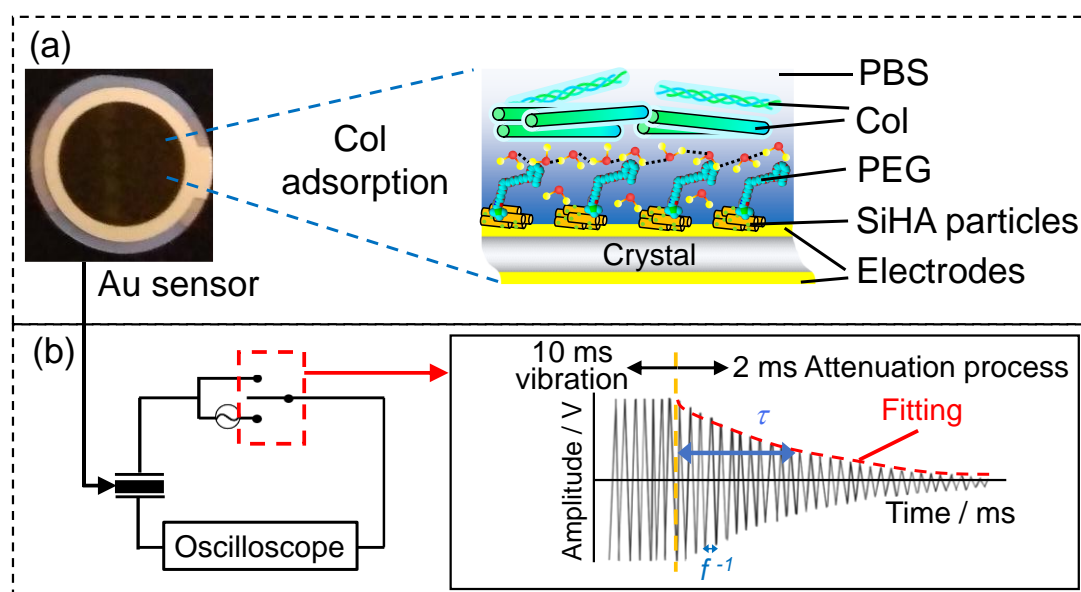
In order to evaluate the hydration layer states in detail, the ratio of the asymmetric stretching vibration component ratio (R_{as}) was determined with the component ratio of “(1) asymmetric O–H stretching vibration among water molecules” (compo(1)) by that of “(3) symmetric O–H stretching vibration of water molecules” (compo(3)) as shown in the following equation (2-4).

$$R = \frac{\text{compo}(1)}{\text{compo}(3)} \quad (2-4)$$

The asymmetric stretching vibration component ratio for the particles reacting with PBS and the PBS solution containing Col were evaluated and were abbreviated as R_{as} and $R_{as}(\text{Col ad})$.

2.2.8 QCM-D Analytical Investigation of the Collagen Fibrillation States

The adsorption behavior with forming the Col adlayers was investigated by the QCM-D technique. An illustration of the QCM-D measurement is shown in **Scheme 2-3**. The sensor contains a thin disc of crystalline AT-cut quartz sandwiched between two gold electrodes, and the top one is the sensor surface. In this study, the Col solution is introduced on the PEG-immobilized SiHA particles deposited on the sensor. When the Col molecules are adsorbed on the sensor (**Scheme 2-3 (a)**), the quartz crystal creates slightly changes in the frequency (f) of oscillation and its duration (**Scheme 2-3 (b)**). A control program tracks the frequency and excites the crystal through a signal generator with an applied AC voltage for 10 ms. By switching off the signal generator for 2 ms, the oscilloscope records the exponentially damped response of the oscillation from the quartz crystal. The computer repeatedly excites the crystal and records the changes in f and the decay time (τ) as shown in **Scheme 2-3 (c)**. From this, the frequency change (Δf) and the energy dissipation change (ΔD) were obtained. Δf and ΔD were detected simultaneously by driving the crystal at 25 MHz (overtone number: $n = 5$), and the Δf value was divided by the overtone number to be $\Delta f_{n=5} / 5$.

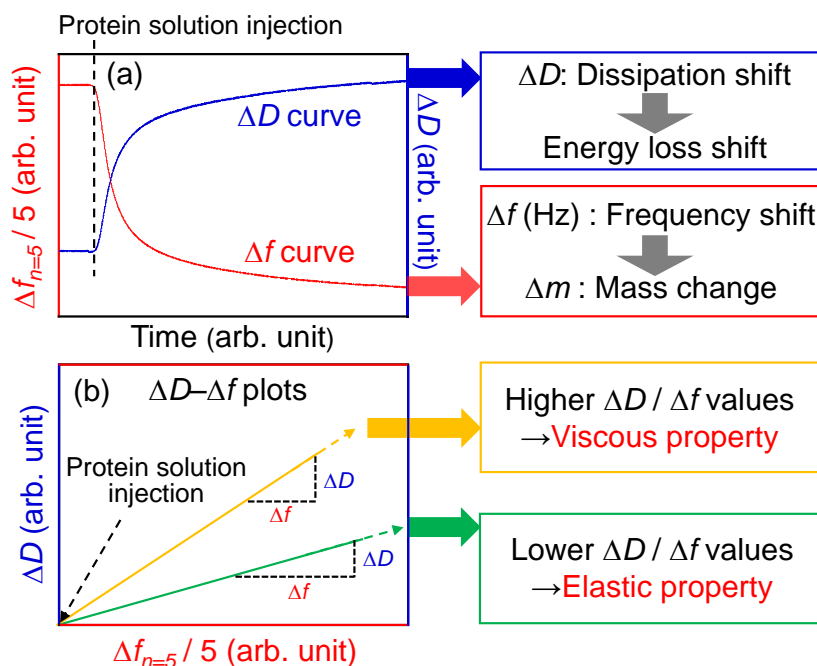


Scheme 2-3. Illustrations of (a) measurement of Col adsorption behavior on the PEG-immobilized SiHA particles using QCM-D sensor, and (b) typical rapid excitation of the QCM-D near resonance, followed by an exponentially damped sinusoidal wave after the rapid disconnection, which can be fitted to calculate the τ .

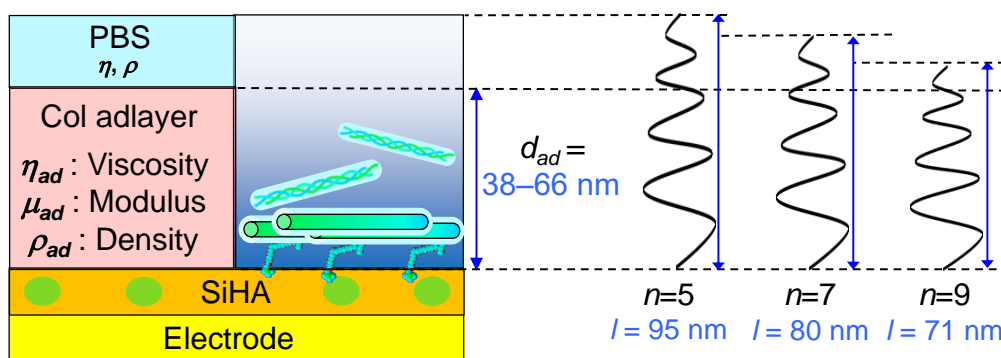
QCM-D measurements were performed by monitoring the Δf and ΔD . PBS (pH=7.4) was introduced on the sensor at the flow rate of 77 mL/min and the Δf and ΔD variations were stabilized at 37 °C for 30 min. Then, the Col/PBS solution was introduced at the flow rate of 77 mL/min and the Δf and ΔD curves were measured at 37 °C for 2 h. The ΔD - Δf plot, which is utilized with Δf and ΔD as the horizontal and vertical axes, was used for evaluating the Col fibrillation behavior. Here, the examples of the Δf and ΔD curves (**Scheme 2-4 (a)**) and the ΔD - Δf plot (**Scheme 2-4 (b)**) were indicated. In injecting protein solution, the Δf generally decreases and ΔD increases. The changes indicate the increasing of protein adsorption mass and energy loss, respectively (**Scheme 2-4 (a)**). The Δf and ΔD values change depending on the protein adsorption amount and adsorption state. The ΔD - Δf plots drawn from the Δf and ΔD values (**scheme 2-4 (b)**) have different slope ($\Delta D/\Delta f$) for each sample. The $\Delta D/\Delta f$ value indicates the change in the energy loss shift per unit weight, it is one of the excellent variables to evaluate the viscoelasticity and structure of the adlayer. When the $\Delta D/\Delta f$ value is high, the adlayer has a viscous property, and when it is low, the adlayer has an elastic property. The ΔD - Δf plot is not always straight, the $\Delta D/\Delta f$ value may change or loop during adsorption depending on the material. Investigating the $\Delta D/\Delta f$ value changes will lead to understanding of the protein adlayer states.

Voinova *et al.* reported that the measured Δf and ΔD curves by the QCM-D technique have been fitted by a Voigt-based viscoelastic model to characterize the viscoelastic properties of the adlayers as a Newtonian fluid as shown in **Scheme 2-5**.⁷⁴⁻⁷⁶ The nonfreezing water components

were not included in the Newtonian fluid because it has the same properties as a solid.



Scheme 2-4. Description of (a) the ΔD and Δf curves, and (b) the ΔD - Δf plots.



Scheme 2-5. Scheme of the geometry and parameters used to simulate the hydration layers and Col adlayers on PEG-immobilized SiHA particle film in contact between the QCM-D sensor surface and a semi-infinite Newtonian liquid. The Col adlayer thickness (d_{ad}) and detectable height (l) of D in the QCM-D system ($n = 5, 7, 9$) were represented.

The viscoelastic parameters, such as viscosity (η_{ad}), elastic modulus (μ_{ad}), density (ρ_{ad}), adlayer thickness (d_{ad}) were fitted by Δf and ΔD curves. From the values, the hydrated Col adlayers ($\mu\text{g}/\text{cm}^2$) formed on the surfaces in PBS were calculated. The fitting was performed by the simplex method, and the optimum solution was derived. The calculation was done using software (Dfind, Biolin scientific).⁷⁴ The detectable height (l) in the QCM-D system can be represented by the following equation (2-5).

$$l = \sqrt{\frac{\eta}{\pi \rho f}} \quad (2-5)$$

It was calculated using the measurement results at 25–45 MHz (overtone number: $n = 5, 7, 9$), and the resultant l was 71–95 nm, which was higher than the d_{ad} value of 38–66 nm by the actual measurement described later. Then, the viscoelastic property is represented by a complex shear modulus G^* given by equation (2-6) based on the Voigt-based model.

$$G^* = G' + iG'' = \mu_{ad} + i2\pi f \eta_{ad} \quad (2-6)$$

where G' is the real part of G^* (storage modulus), G'' is the imaginary part of G^* (loss modulus), f is the oscillation frequency, μ_{ad} is the elastic shear modulus, and η_{ad} is the shear viscosity. The ratio of G'' to G' can be calculated as a loss tangent delta ($\tan\delta$, G''/G') to evaluate the viscoelasticity of the adlayer as shown in equation (2-7).

$$\tan\delta = \frac{G''}{G'} \quad (2-7)$$

Here, it is possibly assumed that the higher concentrated macromolecular solution show the viscoelastic behavior in the boundary layer attached on the sensor surface.⁷⁷ In this study, the Col solution was regarded as the lower concentration and higher viscous, and the boundary viscous resistance was ignored for the calculation.

The surface morphology was observed using a desktop-type scanning electron microscope (SEM, TM3030Plus, Hitachi Co., Ltd.) under an accelerating voltage of 15 kV and a current of 50 mA. The Col adlayers on the sensor was sputter-coated with a 10 nm gold layer by a sputter coater (SC-701MC, Sanyu Electron Co., Ltd.). From the SEM images, the Col fibril coverage (%) was calculated using the software (ImageJ, National Institutes of Health, 2013) and Col fibril density ($\times 10^4 \text{ mm}^{-2}$) was by counting 10–60 Col fibrils.

2.2.9 FT-IR Spectral Deconvolution for Analyzing the Collagen Adlayers

For evaluating the secondary structures of the Col-adsorbed on the particles, the FT-IR spectra of the particles were measured at the wavenumber between 1720–1600 cm^{-1} and deconvoluted as described above. The obtained FT-IR spectra were secondarily differentiated shown in **Figure 2-3**, and the six components were significantly confirmed in the range of the amide I (C=O stretching) band. Using the average values in each peak wavenumber range, the amide I band was deconvoluted into six components of (i) 1634.9, (ii) 1645.8–1649.8, (iii) 1655.1–1659.9, (iv) 1668.8–1167.5, (v) 1684.3–1684.5 and (vi) 1692.7–1699.7 cm^{-1} belonging to (i) β -sheet,^{78,79} (ii) random, (iii) α -helix, (iv) turn, (v, vi) β -turn, respectively. Here, in order to eliminate the influence of the O–H bending vibration of water molecules (1635 cm^{-1}), the difference spectrum could be obtained and used in this study by subtracting the spectrum before Col adsorption from that after Col adsorption, and then was deconvoluted into six components as mentioned above. The deconvolution was performed by fitting with the Gaussian function. In all

the deconvolution, the SOLVER option was used. The residual values by the deconvolutions were less than 1.0 %.

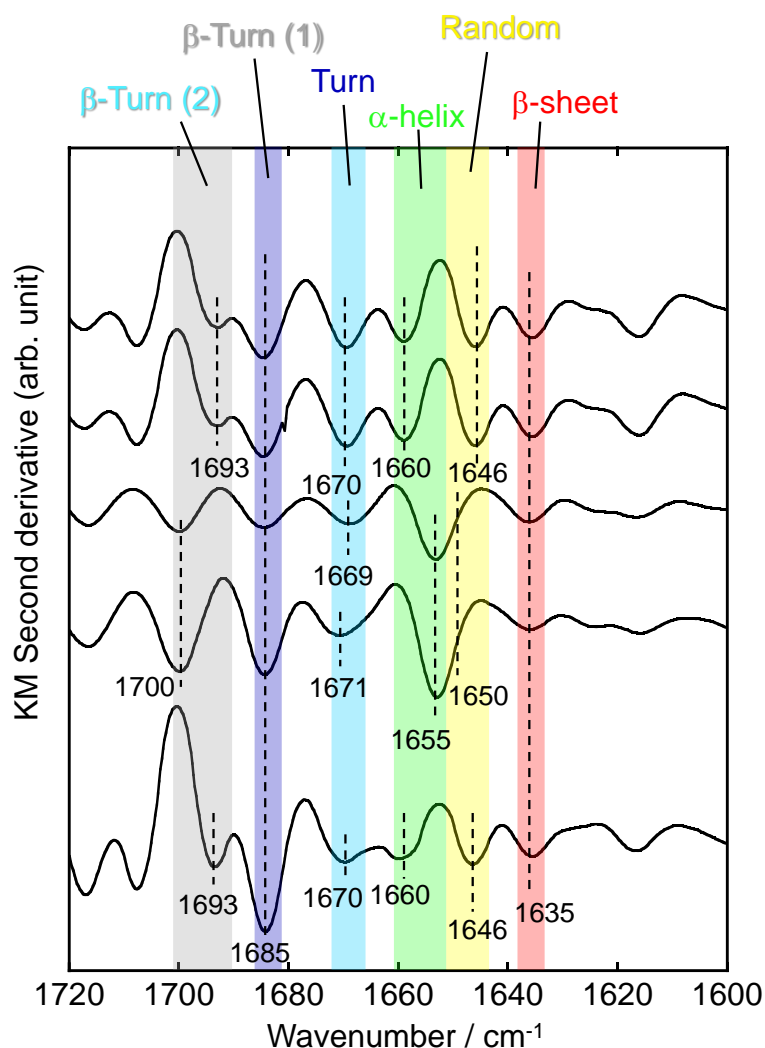
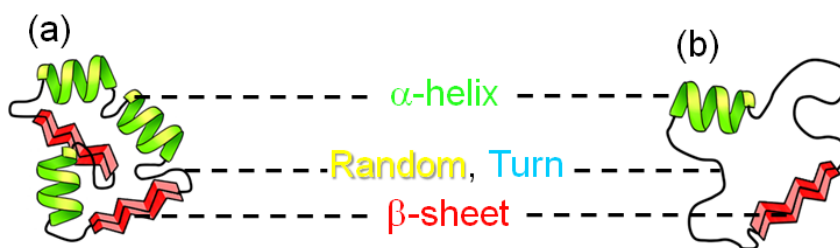


Figure 2-3. The second derivatives of the FT-IR spectra in the Col adlayer of the amide I on the particles.

According to our previous report,³⁸ the possible folded protein structures were investigated and shown in **Scheme 2-6**. In particular, (iii) α -helix and (i) β -sheet can be attributed to native state components, whereas (iv) turn and (ii) random to denatured state components. Accordingly, the components of turn, random, α -helix and β -sheet (compo(turn), compo(random), compo(α -helix), compo(β -sheet)) were calculated and suggested here that the denaturation degree (i.e., Col fibrillation degree) could be evaluated by the following equation (2-8).

$$\text{Col fibrillation degree} = \frac{\text{compo}(\text{turn}) + \text{compo}(\text{random})}{\text{compo}(\alpha\text{-helix}) + \text{compo}(\beta\text{-sheet})} \quad (2-8)$$



Scheme 2-6. Possible illustration of folding protein structures at the (a) native state and (b) denatured states.

2.3 Results and Discussion

2.3.1 Characterization Results of the Silicate-Containing-Hydroxyapatite Particles

Figure 2-4 shows solid-state ^{31}P -NMR DD/MAS spectra of the particles. The chemical shift of ammonium dihydrogen phosphate as the reference was detected at 1.0 ppm. The spectra of the HA and SiHA exhibited the shifts at 2.80 and 2.86 ppm, respectively. The shifts can be assigned to the low crystalline and distorted HA structure.⁸⁰

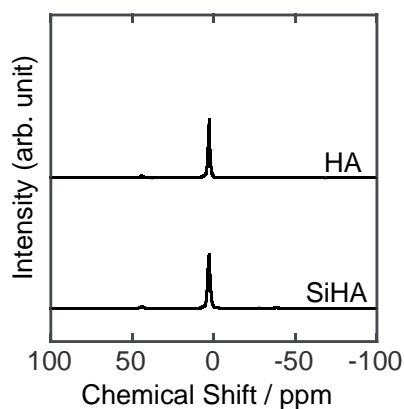


Figure 2-4. Solid-state ^{31}P -NMR DD/MAS spectra of the HA and SiHA particles.

XRD patterns were acquired to evaluate the low crystallinity particles (**Figure 2-5 (a)**). The patterns of the particles were attributed to a single phase of HA ($\text{Ca}_{10}(\text{PO}_4)_6(\text{OH})_2$, ICDD No. 00-009-0432), and exhibited low crystallinity. No diffraction pattern due to silicate was observed in SiHA. The morphological investigation was performed using FE-SEM (**Figure 2-5 (b)**). In the images, the primary particle shapes and the presence of the particle agglomerates was confirmed as the dotted lines indicated. The plate-like shapes were observed and there was no difference in the shape between the samples. The sizes of the HA and SiHA for one particle was about $33 \pm 17 \times 107 \pm 37 \text{ nm}^2$ and $28 \pm 9 \times 88 \pm 33 \text{ nm}^2$, respectively.

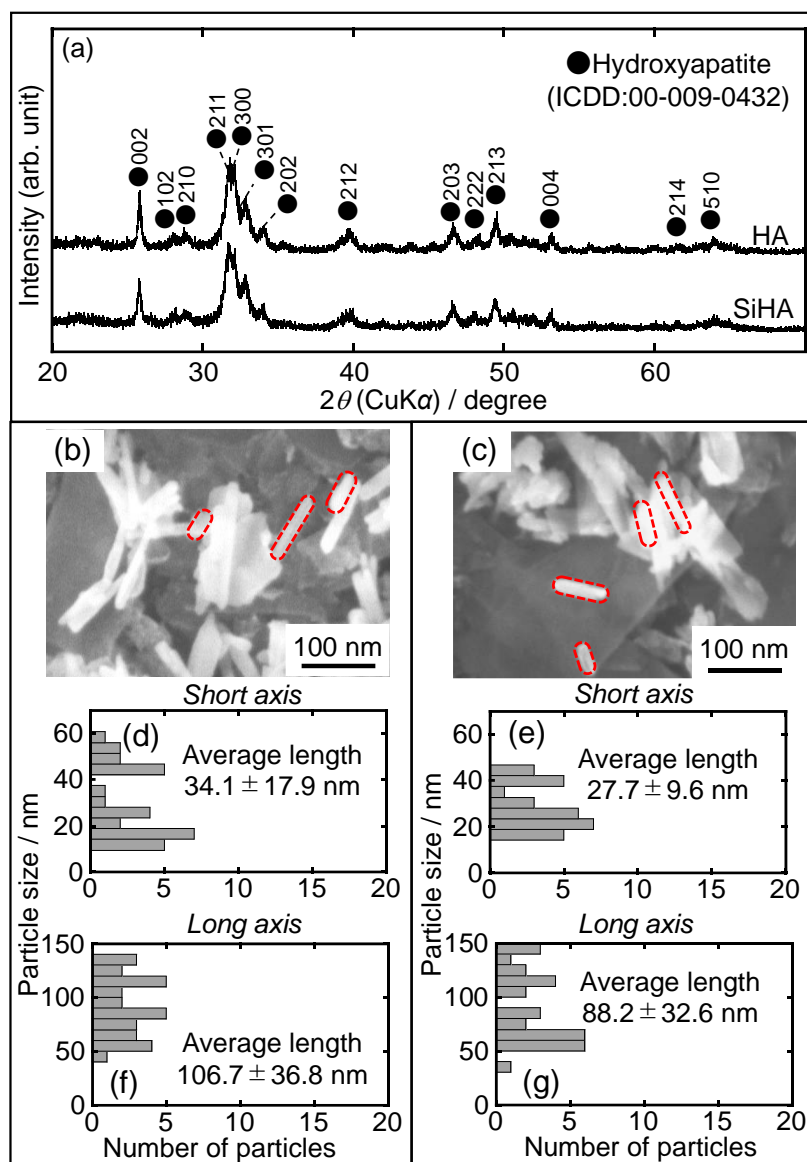


Figure 2-5. (a) XRD patterns and FE-SEM images of (b) HA and (c) SiHA particles, which can be attributed to a single crystalline phase of HA ($\text{Ca}_{10}(\text{PO}_4)_6(\text{OH})$, ICDD:00-009-0432). In the images, the dotted lines indicate the primary particles. (d–g) The (d,e) short and (f,g) long axis length distributions of (d,f) HA and (e,g) SiHA particles.

In order to evaluate the state of silicate, the TEM images confirmed the grain-grown particles (**Figure 2-6**). Only plate-like particles were confirmed in HA, but the rough surface HA particles and the silica phase covering the HA particle surfaces were confirmed in SiHA.

Figure 2-7 shows the solid-state ^{29}Si -NMR spectra of the SiHA particles. The chemical shift of hexamethylcyclotrisiloxane as the reference was detected at -9.4 ppm. The chemical shift of the particle was observed at -50 to -130 ppm, which would be attributed to tetracoordinated silicon atom states (i.e., Q_0 , Q_2 , Q_3 , and Q_4). In order to investigate the shift ratios of Q_0 , Q_2 , Q_3 , and Q_4 , the spectra were deconvoluted as shown in **Figure 2-7 (a)**. The component ratios from

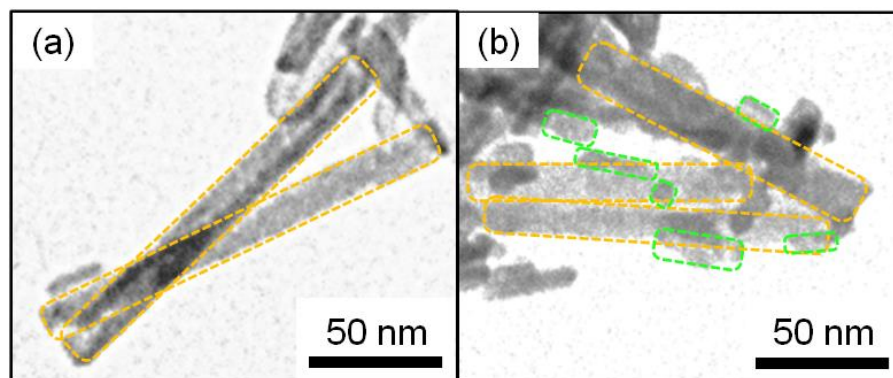


Figure 2-6. TEM images of the (a) HA and (b) SiHA particles. In the images, the orange and green dotted lines indicate the HA and silicate particles, respectively.

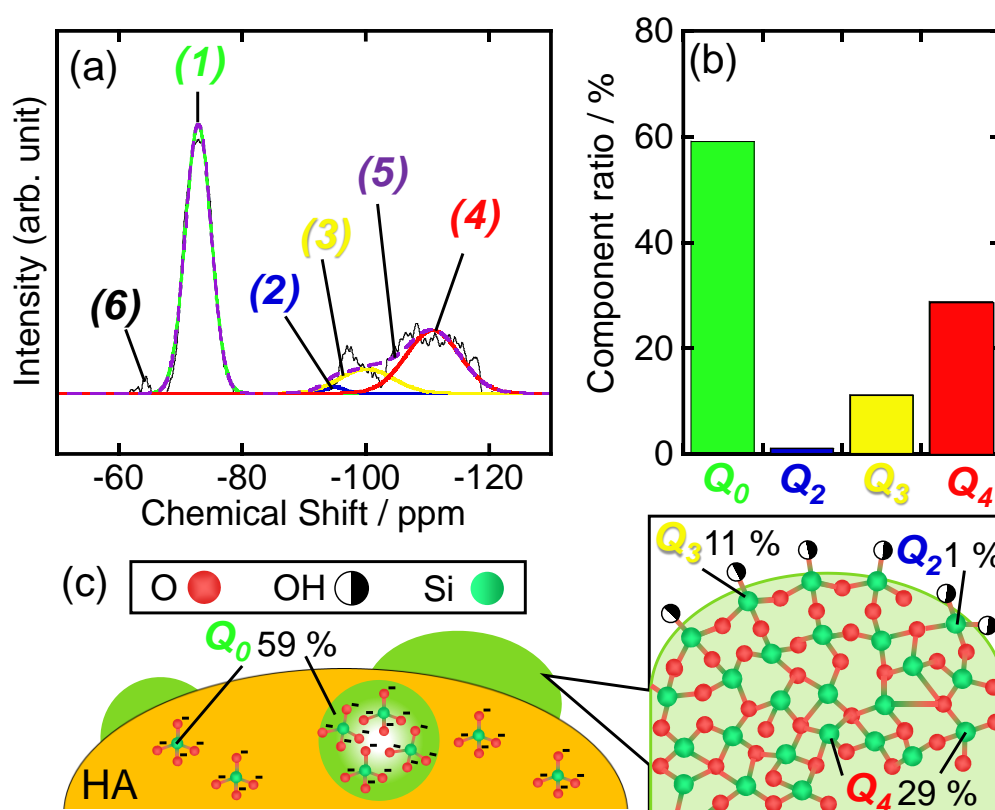


Figure 2-7. (a) Curve-fitting deconvolution result of solid-state ^{29}Si -NMR spectra of the SiHA particles, indicating the spectral peaks of (1) Q_0 (i.e., SiO_4^{4-} substituted with HA crystalline lattice or spherical silicate clusters in HA structure) at -73 ppm, (2) Q_2 (i.e., two Si–O–Si and two Si–OH bonds) at -95 ppm, (3) Q_3 (i.e., three Si–O–Si and one Si–OH bonds) at -100 ppm and (4) Q_4 (i.e., four Si–O–Si bonds) at -111 ppm, and their (5) re-synthesized and (6) raw spectra. (b) Component ratios of Q_0 , Q_2 , Q_3 and Q_4 based on the curve-fitting deconvolution results. (c) Illustration of the possible state of silicate on the SiHA particles.

the results (**Figure 2-7 (b)**) of Q_0 , Q_2 , Q_3 , and Q_4 were 59, 1, 11 and 29 %, respectively. It is considered that SiO_4^{4-} substituted with HA crystalline lattice or spherical silicate clusters in HA structure (Q_0) is derived from the inside of particles and silica phases (Q_2 , Q_3 , and Q_4) are present

on the particle surfaces (**Figure 2-7 (c)**), indicating the effective inclusion of silicate with forming the SiHA particles. Thus, SiO_4^{4-} could be partially replaced with HA. The structural replacement and amorphous silica states of the SiO_4^{4-} units exhibits the biosafety, leading to the possibility of the *in vivo* usage of the SiHA particles.

Table 2-2 shows the various parameters of the particles. From the XRD patterns, the *a*-axis lattice constant increased and the crystalline size decreased due to the TEOS addition. It was suggested that the phosphorous sites were replaced with part of silicate components on the surfaces and the silica phases on the particle surfaces inhibited the particle growth. The *c*-axis lattice constant did not change, it was suggested that the part of CO_3^{2-} introduced to the HA crystalline instead of PO_4^{3-} . As a result, the P content decreased and the Ca/P molar ratio increased by adding TEOS. The total Si concentration in SiHA was 0.47 ± 0.03 wt%, which was measured using XRF analysis. Accordingly, the SiO_4^{4-} molecular occupancy on the particle surfaces (i.e., surface silicate component) was calculated to be $11.5 \pm 1.2\%$ using the component ration of $Q_2 \sim Q_4$ in the NMR result.

Table 2-2. Lattice parameters, crystalline sizes and Ca/P molar ratios of the HA and SiHA particles. As extrapolation parameters, total Si concentration (wt%) and SiO_4^{4-} molecular occupancy (%) of the SiHA surfaces were described.

	Lattice parameter (Å)		Crystalline size (nm)		Ca/P molar ratio
	<i>a</i>	<i>c</i>	D_{300}	D_{002}	
HA	9.423 ± 0.002	6.890 ± 0.001	13.1 ± 0.4	38.1 ± 1.5	1.88 ± 0.02
SiHA	9.437 ± 0.004	6.890 ± 0.001	11.7 ± 2.7	33.8 ± 2.9	2.15 ± 0.16

* Total Si concentration of SiHA: 0.47 ± 0.03 wt%

* SiO_4^{4-} molecular occupancy of SiHA surfaces: 11.5 ± 1.2 %

The AFM topographic and phase-shift images of the particle films were shown in **Figure 2-8**. The R_{ms} values and deposited thickness of the films were 11.2 nm and 6.9 ± 0.4 nm for HA, and 5.2 nm and 7.4 ± 0.6 nm for SiHA. The higher R_{ms} values of the films as compared with the Au substrate (3.8 nm) suggests that the particles were deposited. The deposited shapes were different among the samples, and the sizes were $41.3 \pm 10.4 \times 124.8 \pm 29.4$ nm² for HA and $29.0 \pm 8.2 \times 95.4 \pm 30.9$ nm² for SiHA, indicating the deposited particle shapes and sizes were suppressed by the addition of TEOS. The particle sizes were equivalent to the results derived from the FE-SEM images.

The adsorption amount of hydration layer and Col adlayers was 5.98–8.69 $\mu\text{g}/\text{cm}^2$ and was irrespective of the immobilization amount of PEG, implying the importance of the investigation regarding the adsorption states of the water and Col with immobilization amount of PEG. Although the PEG immobilization has been conventionally considered to inhibit the protein adsorption,⁸¹ and the PEG immobilization density and molecular weight in the PEG had been

demonstrated to play a key role in protein adsorption.⁸²⁻⁸⁴ The protein adsorption amount on PEG-immobilized poly(lactic acid) nanoparticles (weight-average molecular weight (Mw): 2000) was

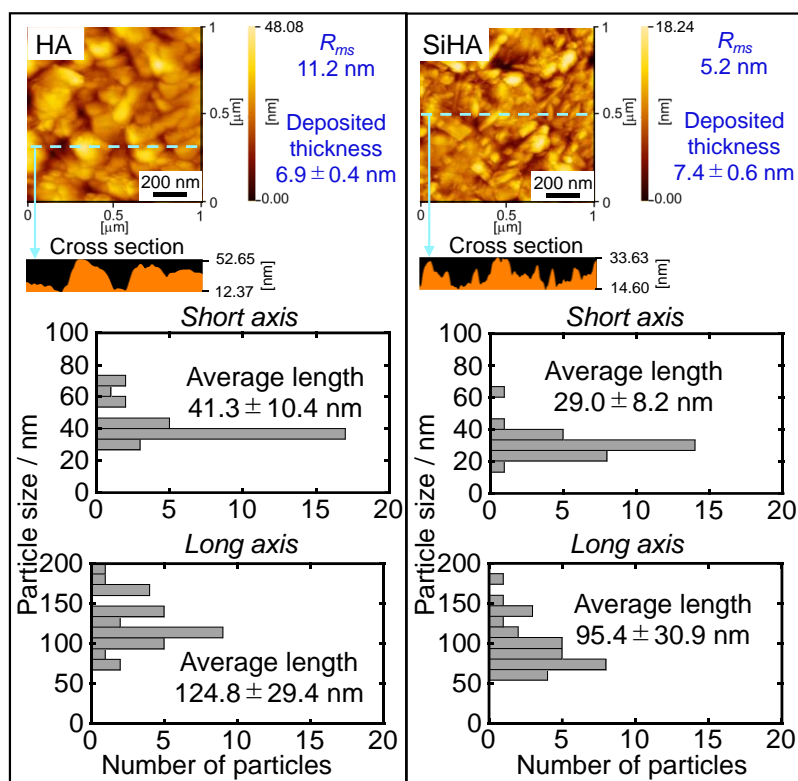


Figure 2-8. AFM topographic images, and the short and long axis length distributions of the deposited particles.

reduced by 43% with the immobilization, and the reduction was by 77% when Mw was 5000.⁸² In the present study, the Mw was 1033 and lower to easily induce the Col adsorption, even though it is implied in our group that the conformation of PEG on the solid surface is very important for the protein adsorption. Additionally, the protein adsorption amount depends on the surface densities of PEG chain,⁸⁵ and that on poly(l-lysine)-graft-poly(ethylene glycol) (MW: 2 kDa) immobilized on Nb₂O₅ decreased by 32–57 % at 0.2 chain/nm² and that was completely suppressed by 100 % at 0.5 PEG/nm². Therefore, the PEG chain immobilization state of the present study likely to prompt the Col adsorption.⁸⁶

2.3.2 Hydration State Changes on the Poly(ethylene glycol)-Immobilized Silicate-Containing-Hydroxyapatite Particles with the Collagen Adsorption

The hydration states on the particles were investigated using FT-IR spectra. The FT-IR spectral deconvolution results of three hydration layers (**Figure 2-9**) and of six water-interactive

states (**Figure 2-10**) formed on the particles, and the resultant component ratios (%) of the six water-interactive states were shown in **Figure 2-10 (a)**. These spectral deconvolutions were performed with high accuracy. In **Figure 2-10 (b)**, the component ratios of (1) Asymmetric O–H stretching vibration between water molecules and (3) Symmetric O–H stretching vibration of water molecules were clearly changed with immobilizing PEG, indicating that the asymmetric stretching vibration component ratio (R_{as}) would be useful for evaluating the reactivity with the Col molecules.

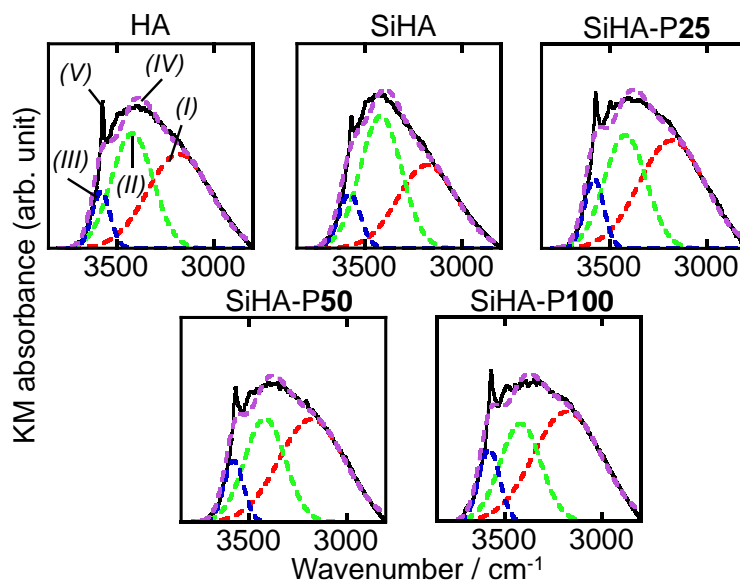


Figure 2-9. FT-IR spectral deconvolution results of three hydration layers formed on the particles. The separated (I), (II) and (III) peaks are attributed to free, intermediate and nonfreezing water molecular states, respectively, and their (IV) re-synthesized and (V) raw spectra are represented.

Figure 2-11 (a) shows the resultant component ratios of three hydration layers formed on the particles and their ratios of intermediate water to free water. By the reaction with TEOS, the component ratio of (I) free water decreased and that of (II) intermediate water increased. The component ratio of (I) increased and that of (II) decreased with increasing the PEG molecular occupancy. As a result, the ratio of free water to intermediate water decreased by the reaction with TEOS and increased with increasing the PEG molecular occupancy. The tendency for the PEG was similar to that for amphiphilic poly(ethylene oxide)–poly(propylene oxide)–poly(ethylene oxide) triblock copolymer modified nanostructured silica/HA hybrid particles.³⁸ In our laboratory, the HA particles similar to the SiHA particles of this thesis had 3.7 wt% of the hydration water measured by TG-DTA (Thermogravimetry-Differential Thermal Analysis). Using the content, it can be assumed that the SiHA particles contain 1.7 wt% of the intermediate water, which is lower than that of the polymers. Thus, it is indicated that the bioceramic particles would contain the smaller hydration amount on the surfaces.^{31,88,89} Furthermore, the R_{as} increased

with increasing the PEG molecular occupancy (**Figure 2-11 (b)**), suggesting that the PEG immobilization enhanced the asymmetric stretching vibration component ratio in free water on the SiHA particles.

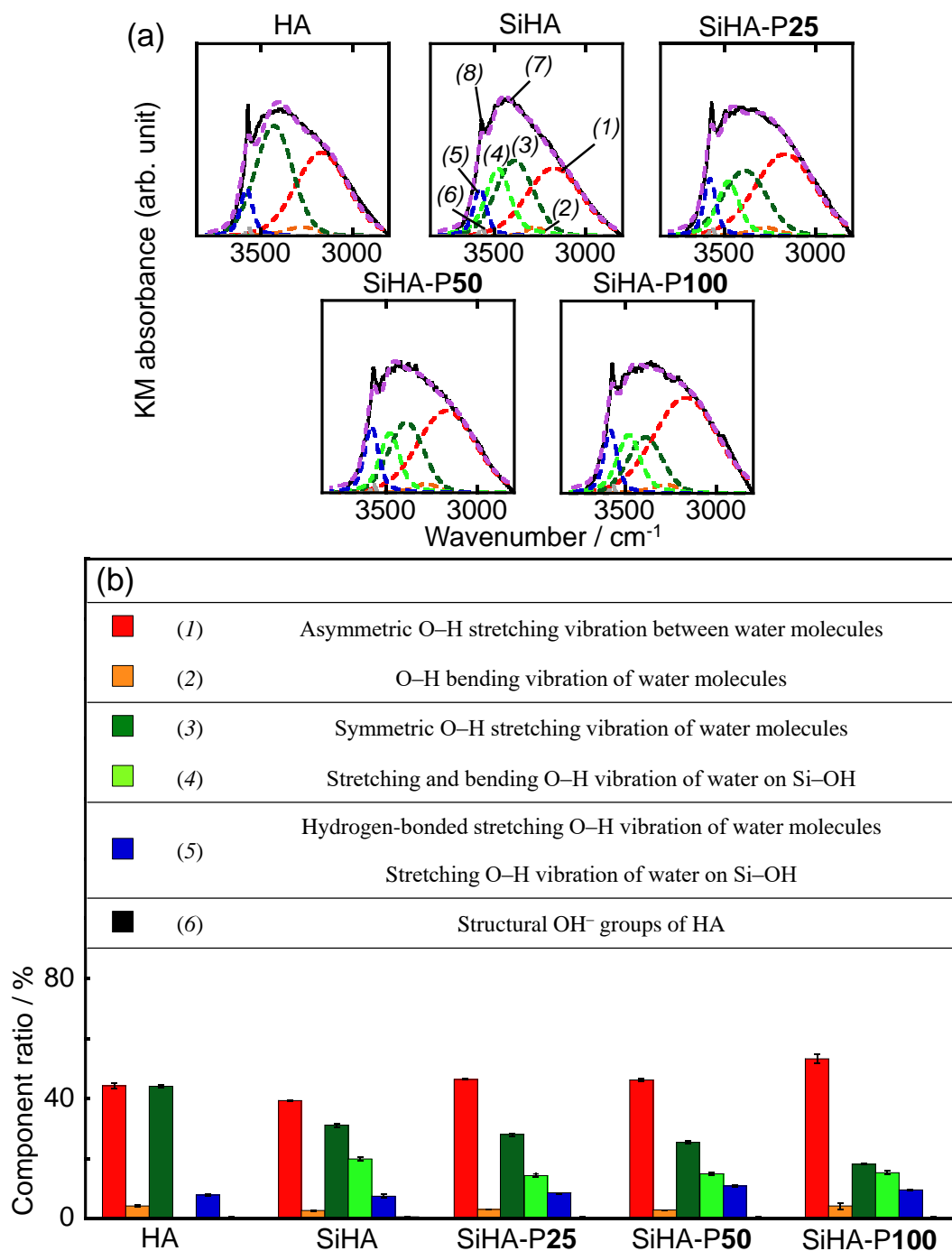


Figure 2-10. (a) FT-IR spectral deconvolution results of six water-interactive states formed on the particles, indicating the separated spectra of (1) asymmetric O–H stretching vibration between water molecules, (2) O–H bending vibration of water molecules, (3) symmetric O–H stretching vibration of water molecules, (4) stretching and bending O–H vibration of water on Si–OH, (5) hydrogen-bonded stretching O–H vibration of water molecules and stretching O–H vibration of water on Si–OH, and (6) structural OH⁻ groups of HA, respectively, and (7) their re-synthesized and (8) raw spectra. (b) Assignments of the six water-interactive states formed on the particles and resultant six component ratios.

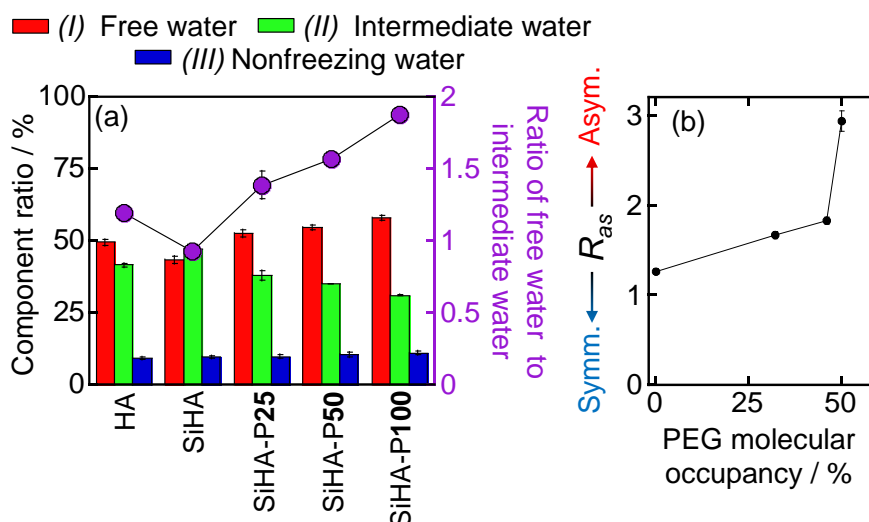


Figure 2-11. (a) Resultant component ratios of three hydration layers formed on the particles and their ratios of free water to intermediate water. (b) R_{as} value change with the PEG molecular occupancy.

The hydration states after the Col adsorption were also investigated. The FT-IR spectral deconvolution results of three hydration layers (**Figure 2-12**) and of six water-interactive states (**Figure 2-13**) formed on the Col-adsorbed particles, and the resultant component ratios (%) of the six water-interactive states and N–H stretching vibration of Col were shown in **Figure 2-13** (a). These spectral deconvolutions were performed with high accuracy, which were evaluated by the same method as for the before the Col adsorption case in **Figure 2-13** (b).

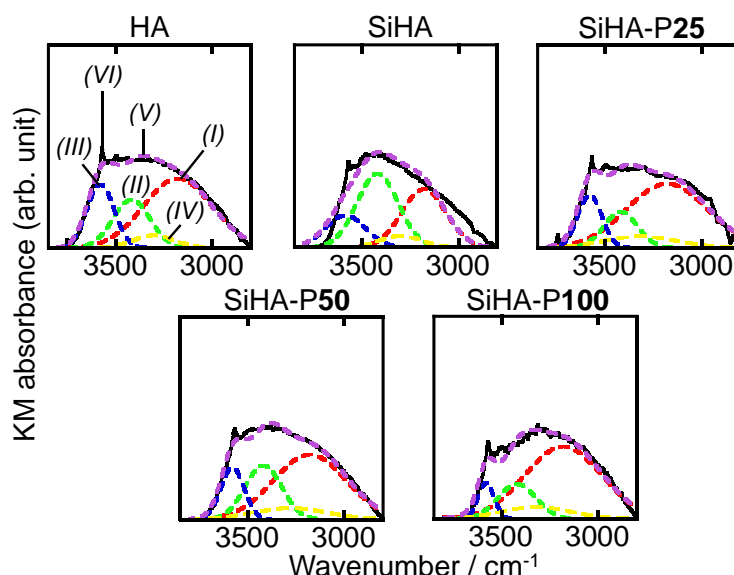


Figure 2-12. FT-IR spectral deconvolution results of three hydration layers formed on the Col-adsorbed particles. The separated (I), (II), (III) and (IV) peaks are attributed to free, intermediate, nonfreezing water molecular states and N–H stretching vibration of Col, and their (V) re-synthesized and (VI) raw spectra are represented.

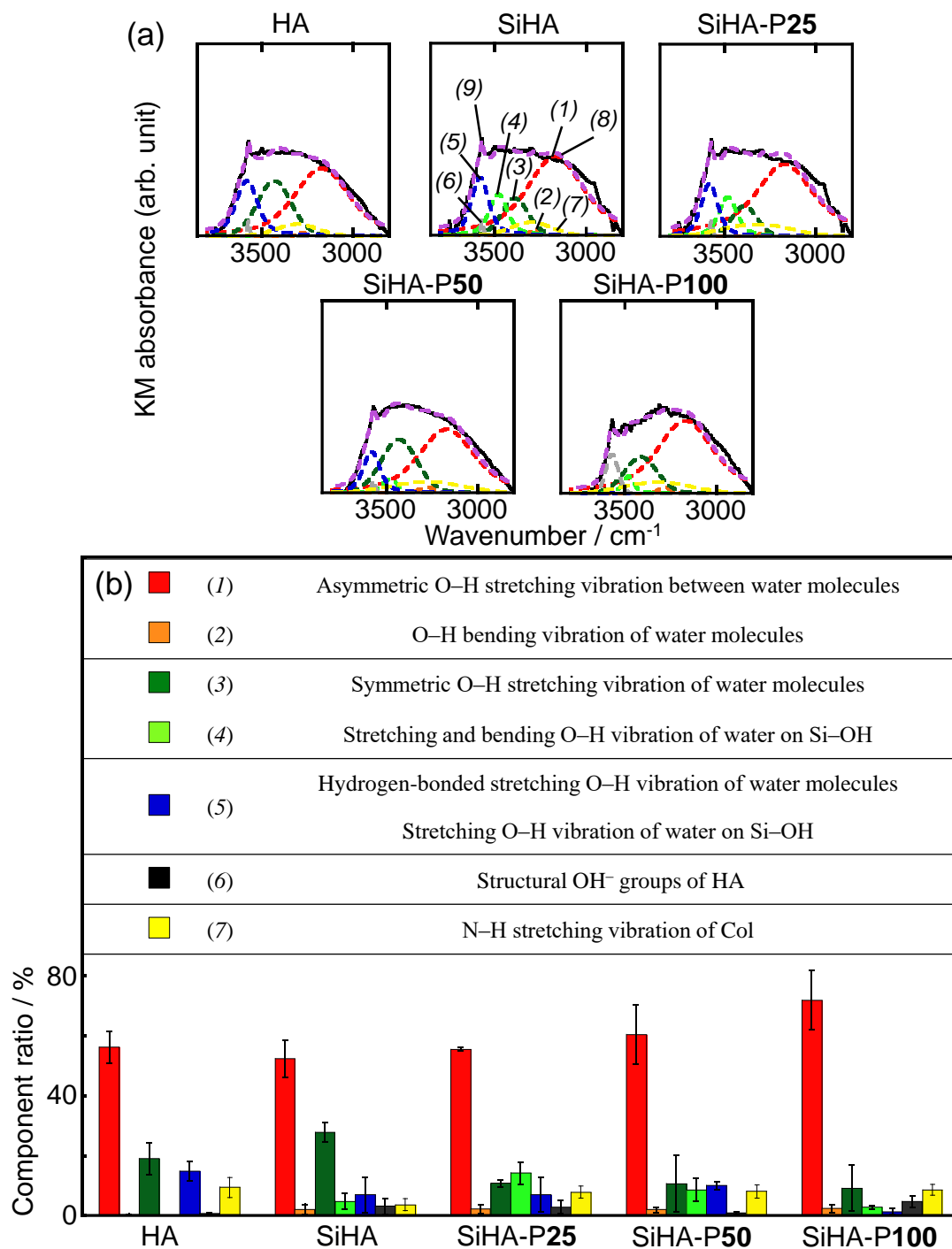


Figure 2-13. (a) FT-IR spectral deconvolution results of six water-interactive states formed on the Col-adsorbed particles, indicating the separated spectra of (1) asymmetric O–H stretching vibration between water molecules, (2) O–H bending vibration of water molecules, (3) symmetric O–H stretching vibration of water molecules, (4) stretching and bending O–H vibration of water on Si–OH, (5) hydrogen-bonded stretching O–H vibration and stretching O–H vibration of water on Si–OH, (6) structural OH^- groups of HA and (7) N–H stretching vibration of Col, respectively, and (8) their re-synthesized and (9) raw spectra. (b) Assignments of the six water-interactive states formed on the particles and resultant six component ratios.

Figure 2-14 (a) shows the resultant component ratios of three hydration layers formed on the Col-adsorbed particles and their ratios of intermediate water to free water. In the HA particles

of our previous paper,⁸⁷ the hydration layer states after fibrinogen adsorption was evaluated, and the component ratios of free, intermediate and nonfreezing water states were 53 %, 27 % and 20 %, respectively, which were almost same to the case in the present HA after the Col adsorption (54 %, 28 %, and 18 %) in this thesis. By the reaction with TEOS, the component ratio of (II) intermediate water increased. The component ratio of (I) free water increased and that of (II) decreased with increasing the PEG molecular occupancy. As a result, the ratio of free water to intermediate water decreased by the reaction with TEOS and increased with increasing the PEG molecular occupancy, and the ratios were lower all around as compared with the case before the Col adsorption (**Figure 2-11 (a)**). No significant difference was found in the component ratio of N–H stretching vibration in each particle, which was consistent with the tendency that there was no correlation between the adsorption amount of Col adlayers and the PEG immobilization. On the other hand, **Figure 2-14 (b)** shows $R_{as (Col ad)}$ with the PEG molecular occupancy. Surprisingly, the $R_{as (Col ad)}$ was higher all around than the R_{as} (**Figure 2-11 (b)**) and that increased by the immobilization of PEG. In the presence of the adsorbed Col molecules, the water molecules of free water became abundant and the intermediate water decreased and the asymmetric stretching vibration component ratio in the free water increased, and these were effectively enhanced with the PEG immobilization.

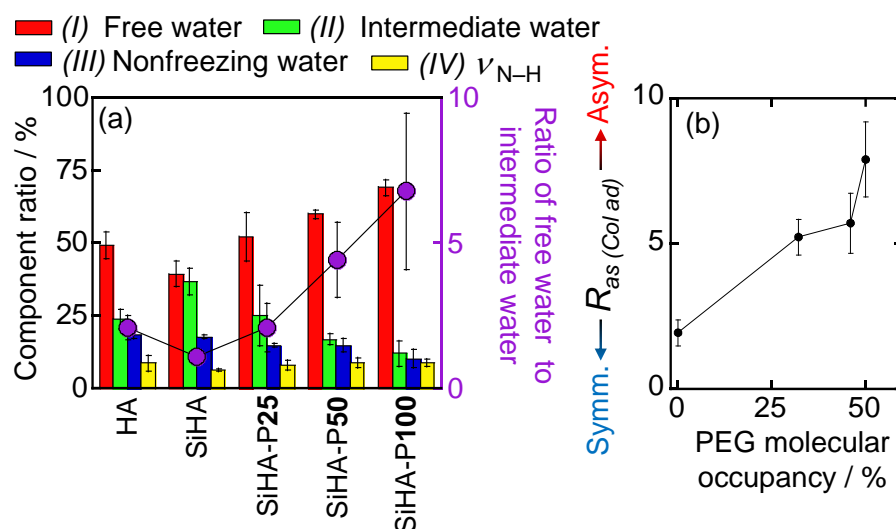


Figure 2-14. (a) Resultant component ratios of three hydration layers formed on the Col-adsorbed particles and N–H stretching vibration of Col, and their ratios of free water to intermediate water. (b) $R_{as (Col ad)}$ value change with the PEG molecular occupancy.

2.3.3 Surface Modification Effect of the Hydroxyapatite Particles on Collagen Fibrillation via Interfacial Hydration States

Figure 2-15 shows the ΔD and Δf curves with the Col adsorption process on the particle films. It was observed that Col was effectively adsorbed on the films with the adsorption time. Δf

(i.e., adsorbed amount) clearly increased with the reaction with TEOS and ΔD (energy dissipation change) increased with the immobilization of PEG.

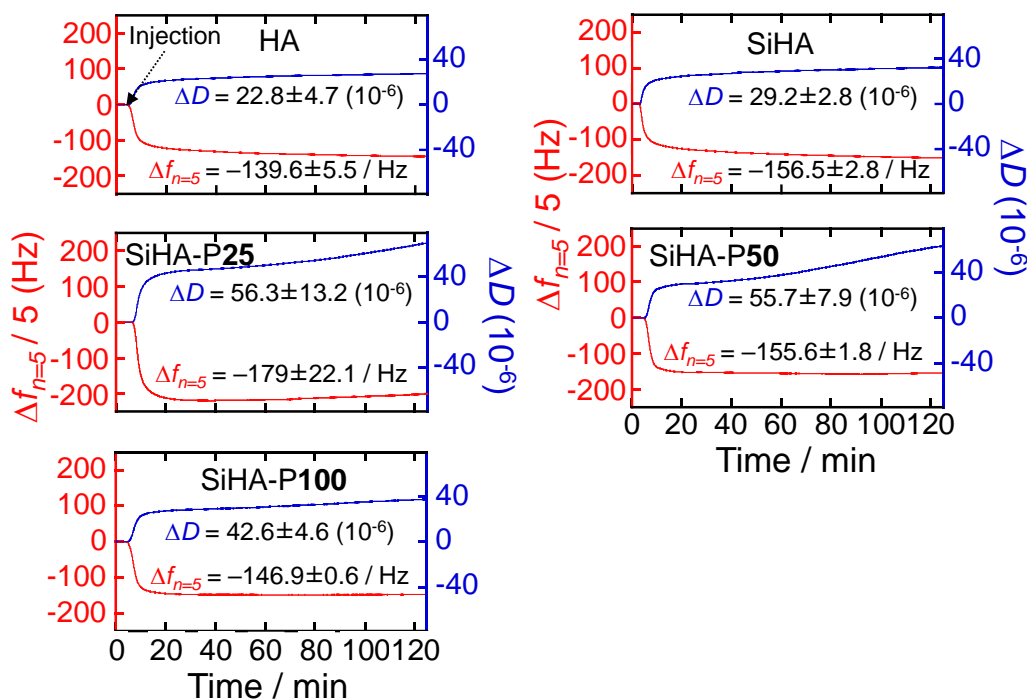


Figure 2-15. ΔD and Δf curves with the Col adsorption process on the particle films.

ΔD – Δf plots with the Col adsorption process (**Figure 2-16 (a–e)**) were drawn and evaluated using ΔD and Δf curves for investigating the PEG immobilization effect on the ΔD change. In HA and SiHA, there was tendency of the slight increase in the ΔD – Δf slope at around 35–40 min, which would be attributed to the mild denaturation and/or fibrillation of the Col molecules with the adsorption process. In SiHA-P25, SiHA-P50 and SiHA-P100 (**Figure 2-16 (c–e)**), the Δf values slightly increased (or stopped increasing) from the inflection points at around 32–34 min, and the ΔD values sharply increased, indicating the effective fibrillation among the Col molecules lead to a decrease in the adsorption amount. In other words, the ΔD – Δf changes demonstrated the interfacial reactions with the Col adsorption as well as the hydration water behavior. Thus, we proposed the water molecular changes with the adsorption and fibrillation of the Col molecules as shown in **Figure 2-16 (f)**. The illustration shows the possible interfacial reactions with the Col molecular adsorption and subsequent fibril formation, indicating the dynamic mobility of water molecules in the adlayer. Therefore, it is probable that the water molecules hydrated in Col were moved to the PEG on the particles and Col surfaces as the unrestricted conditions, causing a decrease in Δf and an increase in ΔD .

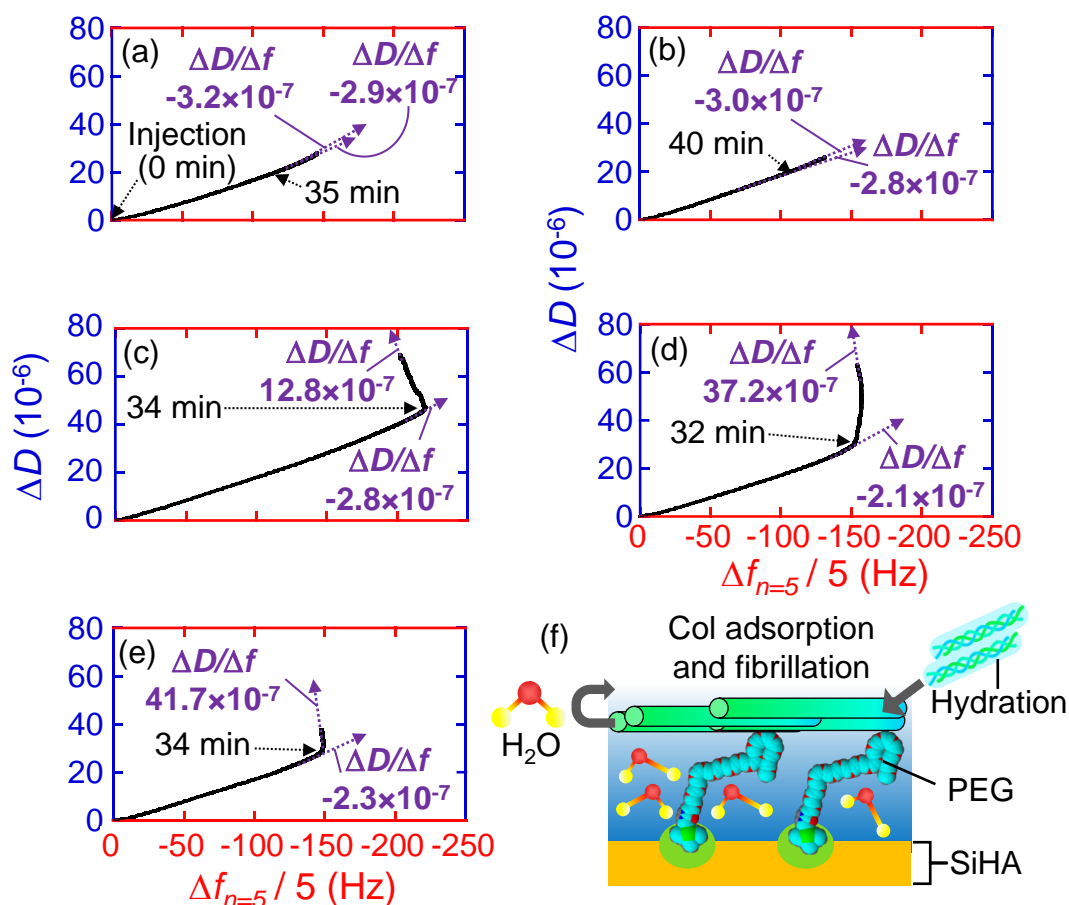


Figure 2-16. ΔD - Δf plots with the Col adsorption process on (a) HA, (b) SiHA, (c) SiHA-P25, (d) SiHA-P50 and (e) SiHA-P100 particle films. (f) Illustration of the possible interfacial reactions with the Col molecular adsorption and subsequent fibril formation, indicating the dynamic mobility of hydrated water molecules.

In order to evaluate the Col adsorption behaviors, the FT-IR spectral deconvolution results of the amide I bands and their secondary structural component ratios (%) were shown in **Figure 2-17 (a)**. The spectral shapes were different among each sample. The component ratios obtained from the deconvolution results were summarized as shown in the **Figure 2-17 (b)**. There was difference in the component ratios involved in the Col fibrillation degree.

The Col fibrillation degrees were calculated as described in the experimental section (**Scheme 2-6**). **Figure 2-18 (a)** shows the Col fibrillation degree based on the component ratio for the secondary structures of the adsorbed Col. The degree decreased with the reaction with TEOS, and significantly increased with increasing the PEG molecular occupancy. The degree also increased with increasing the R_{as} (**Figure 2-18 (b)**). From the results, the Col fibrillation degree was effectively and positively correlated with the asymmetric stretching vibration

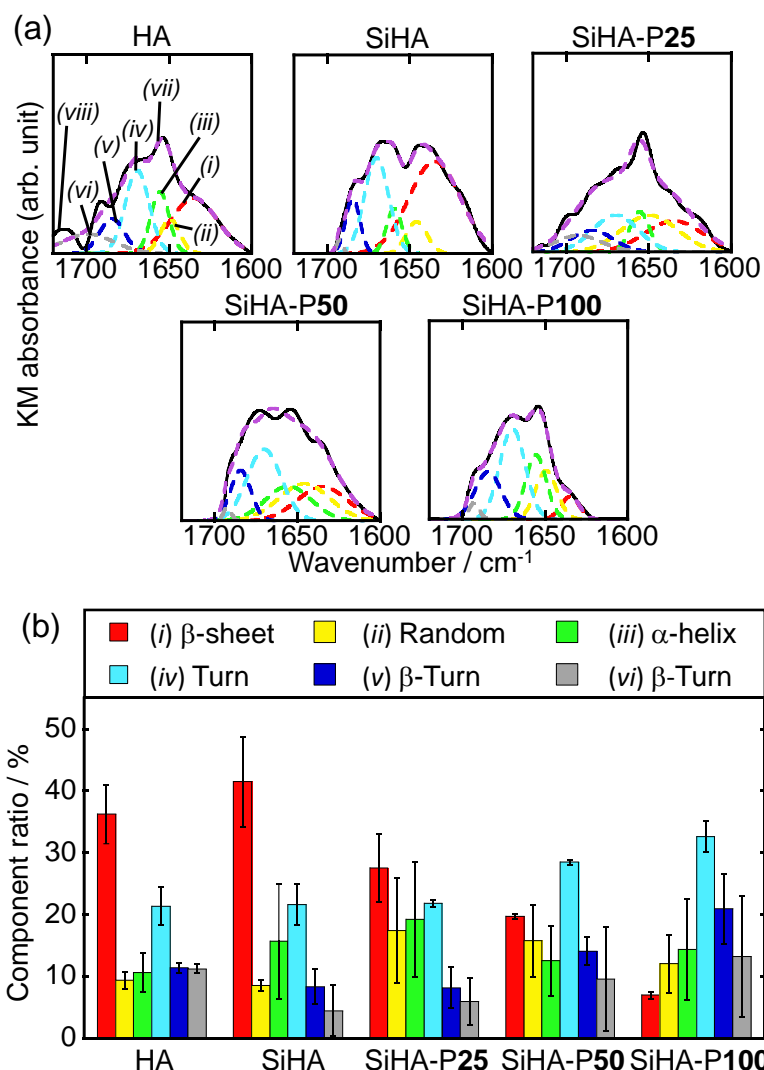


Figure 2-17. (a) FT-IR spectral deconvolution results of the amide I bands of the adsorbed Col on the particles to provide the secondary structural components ((i) β -sheet, (ii) random, (iii) α -helix, (iv)(v) β -turn, (vi) turn), and their (vii) re-synthesized and (viii) raw spectra. (b) Component ratios on the secondary structures of the amide I bands in the adsorbed Col on the particles.

component ratio in free water on the particles. Here, the schematic illustration and chemical reaction with the aldol condensation and dehydration among the Col molecules is shown in **Figure 2-18 (c)** to explain the changes of the Col fibrillation degree and R_{as} . The Col molecules (tertiary structure) is composed of three chains (secondary structure), and there are many compo(α -helix) and compo(β -sheet) on the chains, and the components would be decreased when the fibrillation based on an aldol condensation reaction was promoted.⁹⁰ Therefore, it is presumed that the Col fibrillation as well as the denaturation simultaneously appeared with the adsorption process on the present particle surfaces. By the aldol condensation reaction, the dehydrated free water molecules derived from the intermediate water states existing in the Col molecules would be produced,⁹¹ and interacted with the surrounding environment (e.g., Col fibril surfaces,

PEG group, etc.), which can explain the results of the change in the component ratio of free to intermediate water and R_{as} .

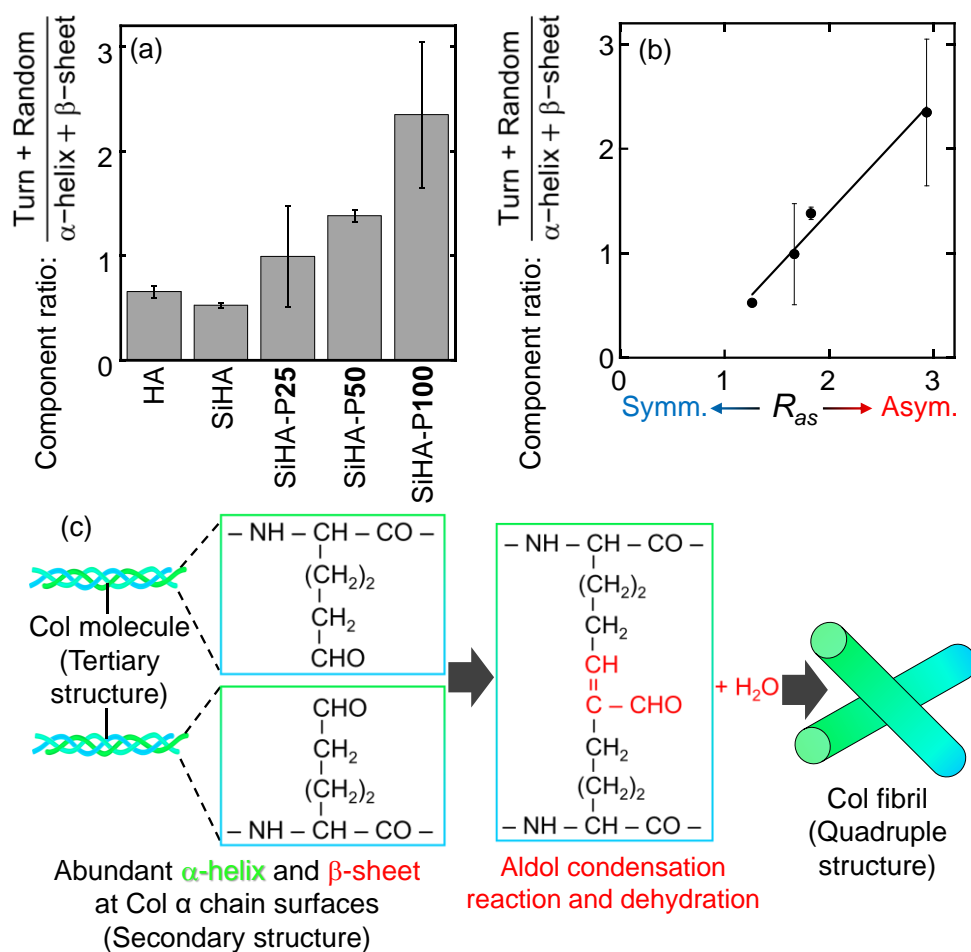


Figure 2-18. (a) Col fibrillation degrees based on the component ratio for the secondary structures of the adsorbed Col, and (b) change in the component ratio with R_{as} , indicating the linear correlation ($R^2=0.97772$). (c) Schematic illustration and chemical reaction of the aldol condensation and dehydration among the Col molecules.

Figure 2-19 shows the viscoelastic properties of the hydration layer and Col adlayers of viscosity, elastic modulus and $\tan\delta$, and their changes with asymmetric component ratio (R_{as}). There was no significant difference in the η_{ad} among the particles. The μ_{ad} value decreased with the reaction with TEOS and effectively increased with the PEG immobilization. It has been reported the increase in μ_{ad} would be attributed to the fibrillation.⁹² The elastic modulus of adsorbed Ab and fibronectin measured by QCM-D in the previous paper were 1.1–1.8 kPa, indicating that the measured values are correct.⁹³ Here, elastic modulus of the bulk Col fibrils was 1–2 GPa⁹⁴ and 5–11.5 GPa⁹⁵ by an AFM measurement under dry condition in air, and the hydration layer states in water reduced ~ 2 – 3 orders of magnitude.^{96,97} The monomeric Col molecule (i.e., tropocollagen) is not solely responsible for the elasticity in neutral pH buffer, and the interactions with the fluid phase outside/within the fibrils are a significant contributor.⁹⁸ In

this thesis, the SiHA particle films immobilized with PEG provided the lower elastic modulus of the water and Col fibril adlayers, suggesting the novel water-interactive Col adlayer. From the equation (2-7), $\tan\delta$ increased with the reaction with TEOS and decreased with the PEG immobilization. The $\tan\delta$ indicates viscous body ($\tan\delta > 1$) and elastic ($\tan\delta < 1$), it is shown that the Col adsorption layer becomes elastic body (Col fibrillation) by the PEG. Therefore, the reaction of TEOS suppressed the Col fibrillation and the PEG immobilization promoted. From these results, it is inferred that the hydration layer states on bioceramics significantly play a role in the viscoelastic properties of the subsequently-formed adlayers.

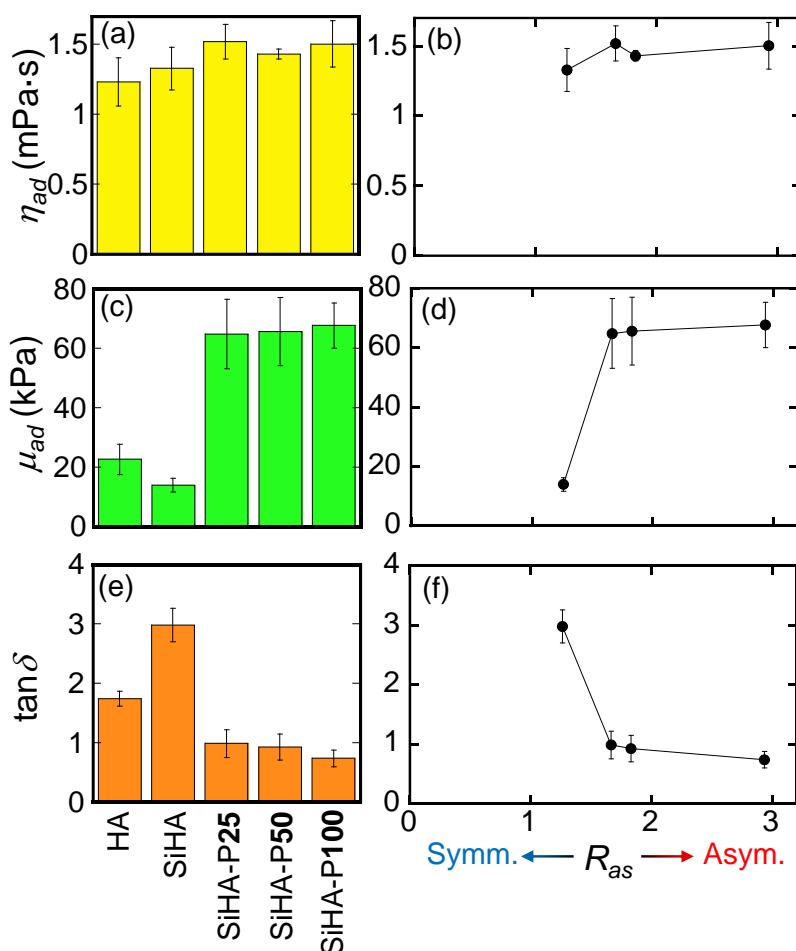


Figure 2-19. Viscoelastic properties of the hydration and Col adsorption layers of (a, b) η_{ad} , (c, d) μ_{ad} and (e, f) $\tan\delta$, and (b, d, f) their changes with R_{as} .

To evaluate the Col fibrillation states, the SEM images of the Col fibrils formed on the PEG-immobilized particles were investigated, and their coverages and densities were calculated as shown in **Figure 2-20**. The Col fibrillation was confirmed in all the particles. The inset plots indicated the Col fibril coverage and density changes with the PEG molecular occupancy. As compared with HA, SiHA suppressed the Col fibrillation. The fibril coverage and density

increased by the PEG immobilization, and increased with increasing the PEG molecular occupancy. Therefore, it suggested that the PEG immobilization enhanced the Col fibrillation.

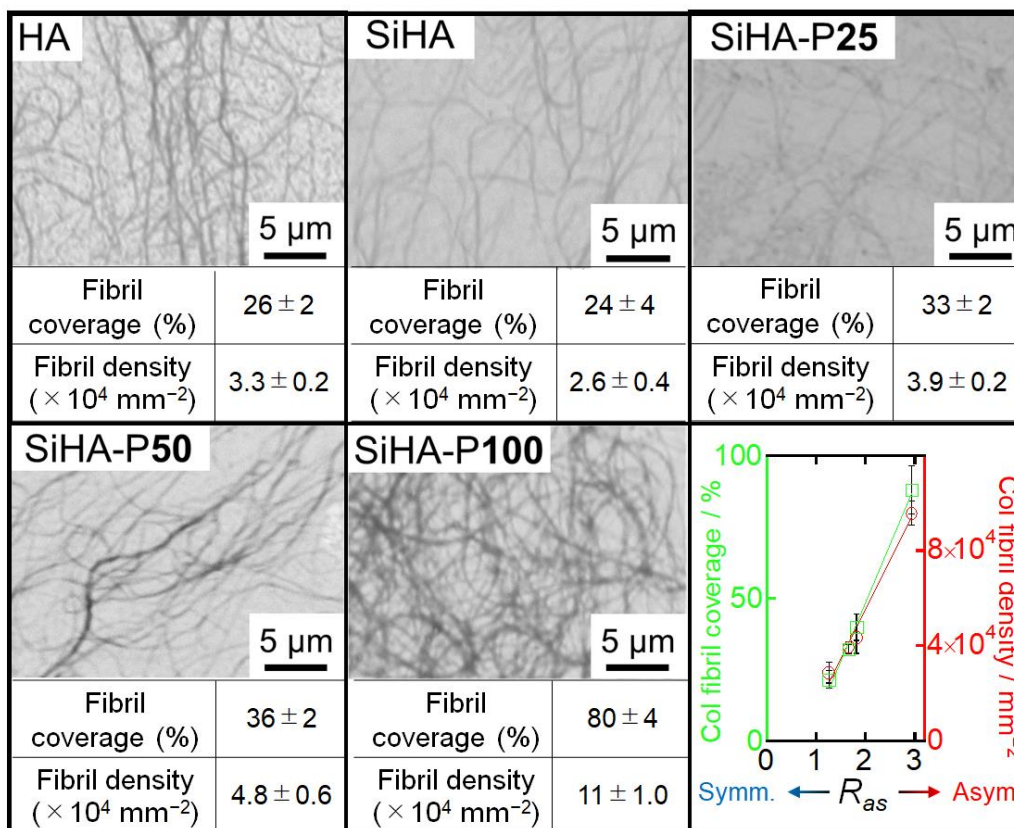


Figure 2-20. SEM images of the Col fibrils formed on the PEG-immobilized particles, and their coverages and densities. The inset plots indicate the Col fibril coverage and density changes with the R_{as} . The liner correlation is $R^2=0.98315$ and $R^2=0.99186$, respectively.

The possible interfacial reactions based on the above results is shown in **Figure 2-21**. In the reaction between the Col molecules and the HA or SiHA particle surfaces, the binding of the carboxylate group of Col to a calcium ion of HA is important for the initial adsorption process.⁹⁹ By the Si ion substitution into HA, it has been reported that the Col adsorption amount increased and the biological activity was improved,¹⁰⁰ indicating the preferential Col affinity with the Si-substituted HA. In the presence of silicate on the particles as SiHA, the water molecules would form the hydrogen bond networks, forming the abundant intermediate water states.^{38,39} Here, it is thought that the nonfreezing water does not participate in the reaction because it can be regarded as the same properties of the solid state. Then, the intermediate water on the SiHA particles would repel the intermediate water hydrated with Col molecules,¹⁰¹ and the mobility of the water molecules does not occur with the adsorption process. the repulsive force (F_{hyd}) is shown in equation (2-9).¹⁰²

$$F_{hyd} = 2\pi RW_0 e^{-D/\lambda_0} \quad (2-9)$$

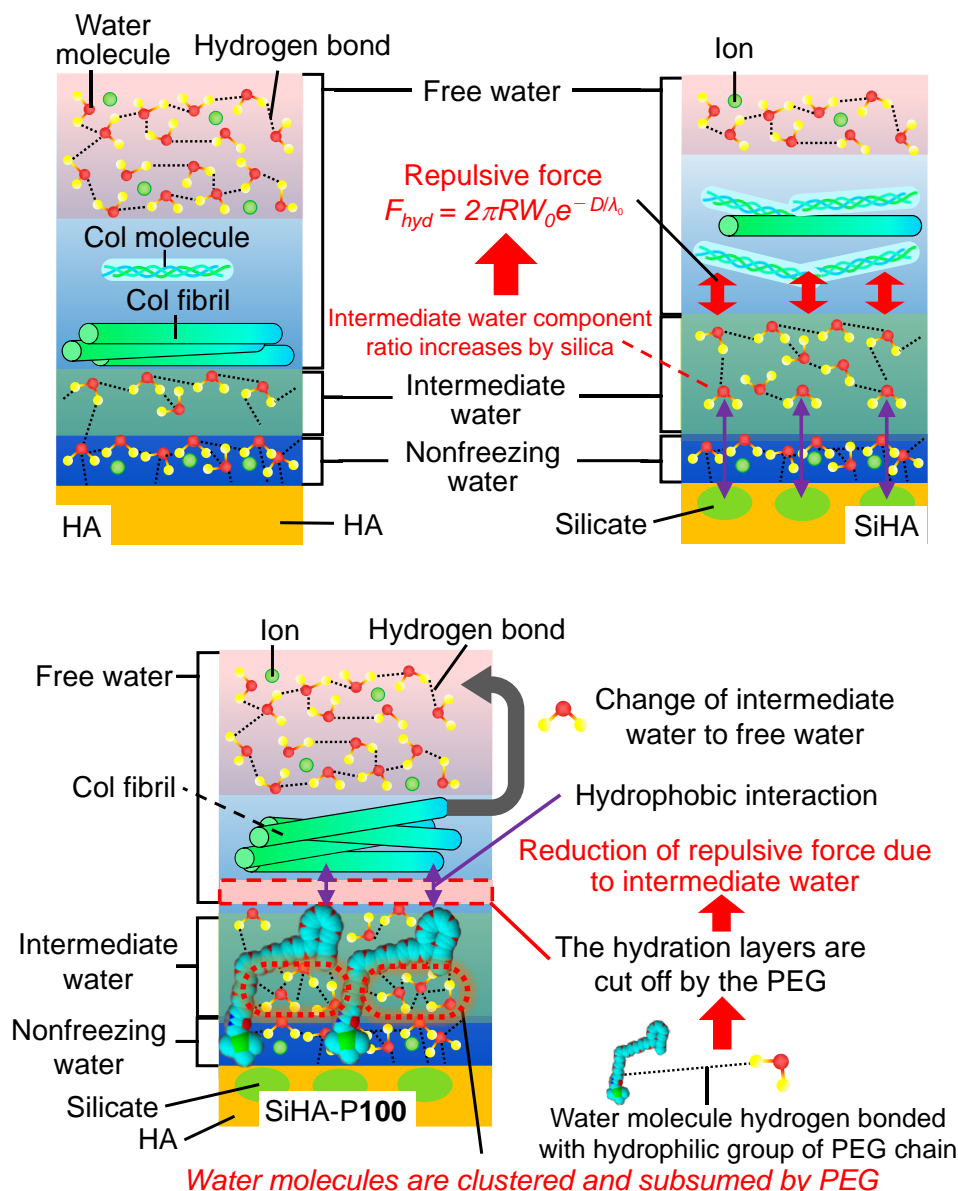


Figure 2-21. Illustration of the possible interfacial reactions between the Col molecules and the HA, SiHA and SiHA-P100 particle surfaces.

R is Col molecule reaction site radius [m], W_0 is surface energy [J/m^2], λ_0 is the distance between Col molecule and water molecule [m]. The repulsive force inhibited the excessive adsorption on the particle surfaces, and the adsorption states of the Col molecules were preserved upon suppression the Col fibrillation. In fact, the Col on SiHA significantly contained the higher compo(α -helix) and compo(β -sheet) ratios, indicating the three-dimensionally- and natively-adsorbed states.

In the reaction between the Col molecules and SiHA-P100, with the Col adsorption, the Col molecules were dehydrated to produce the water molecules through the condensation reaction to be Col fibrils. The hydrogen atoms of water molecules bind to the oxygen atoms of PEG, and resultantly the water molecular clusters are formed,¹⁰³ which has dominantly been attributed to

ether oxygen as hydrogen bonding basicity in PEG chains.¹⁰⁴ Since the water molecules in the PEG cannot sufficiently bond with each other, the number of hydrogen bonds with the other water molecules is maximized. When there are no other molecules, a strong hydrogen bond network is formed inside the water cluster.¹⁰⁵ Then, the other water molecules were moved to the Col fibril surfaces as the free water states. Accordingly, the intermediate water molecules of Col were changed to be free water in the surrounding environment. In the absence of the repulsive force among the intermediate water molecules at two sides, the Col molecules directly interact with the hydrophobic parts in the PEG chains based on the hydrophobic interactions, promoting the denaturation of Col molecule (i.e., fibrillation). Here, the hydration layer on SiHA forms a regular network structure with continuously long-period hydrogen bonds via nonfreezing water, intermediate water, and free water. The PEG chains interacting with the clustered water molecules interrupted or weakened the repulsive force between the intermediate water molecules at the Col–PEG interfaces. In general, the polymer chains generate the hydrogen bond defects in the surrounding water networks.¹⁰⁶ Therefore, it is assumed that the PEG chains on the SiHA-P100 particles formed the irregular hydrogen bonding networks at the Col–PEG. After this, the intermediate water molecules of the Col fibril would be moved to the surfaces. Subsequently, the Col molecules adsorbed on the hydrophilic Col molecular sides that hydrophobically interacted with the PEG chain, resulting in the quick fibrillation under the small repulsive force. Accordingly, the hydration layer on the SiHA-P100 particles become the driving force of the Col fibrillation in the early reaction stage. And then, the Col fibrils with the smaller amount of the intermediate water promote the fibrillation preferentially interacting with the absorptive Col molecules. In this way, it is thought that the hydration layer and Col molecules interact with each other to provide the effective fibrillation. From the results, the PEG-immobilized SiHA particle surfaces can effectively and quickly produce the Col fibril states, suggesting the importance of the control of hydration layer states on the HA of the living body. In particular, the importance of the R_{as} value can significantly affect the Col fibrillation states (degree, coverage and density).

2.4 Conclusion

The SiHA particles were synthesized and were immobilized by PEG for clarifying the effect of bioceramic surface hydration layer states on the Col fibrillation degree. The plate-like SiHA particles containing SiO_4^{4-} ions inside or/and outside the particles were obtained. PEG was successfully immobilized on the SiHA particles, and the hydration layer and Col adlayer states on the particles were investigated for exemplifying the importance of the water molecular states at the interface. The ratio of free to intermediate water on the particles decreased by containing silicate component, and that increased with increasing the PEG molecular occupancy, where the R_{as} increased with increasing the occupancy. Surprisingly, all the $R_{as (Col. ad)}$ values were higher

than the cases in R_{as} , indicating the hydration layer state and interaction changes by the Col adsorption. In the QCM-D measurement, the Δf and ΔD values of the PEG immobilized SiHA particles increased with the Col adsorption for 32–34 mins and then Δf slightly increased (or stopped increasing) and ΔD dramatically increased, indicating the effective water mobility and state changes by the Col adsorption and subsequent fibrillation on the PEG-immobilized particles. The Col fibrillation degree, which was evaluated by $\tan\delta$ and protein secondary structure of the adlayers, clearly increased by the PEG-immobilization, and the tendency was supported by the fibril density under the SEM observation. Although the stereoscopic states of the Col on the SiHA particles were preserved with the adsorption, SiHA-P100 can widely and effectively induce the Col fibrillation by the PEG-immobilization. In particular, the Col fibrillation degree based on the protein secondary structure was significantly correlated with the asymmetric stretching vibration component ratio in free water molecules of the hydration layer on the particles, suggesting the importance of the hydration layer states on bioceramics for controlling the efficient Col fibrillation.

References

- 1 H. C. Anderson, *J. Cell Biol.*, 1969, **41**, 59–72.
- 2 A. M. Ferreira, P. Gentile, V. Chiono and G. Ciardelli, *Acta Biomater.*, 2012, **8**, 3191–3200.
- 3 S. J. Jones, A. Boyde and J. B. Pawley, *Cell Tissue Res.*, 1975, **159**, 73–80.
- 4 S. C. Marks and P. R. Odgren, in *Principles of Bone Biology*, Elsevier, 2002, pp. 3–15.
- 5 A. J. Salgado, O. P. Coutinho and R. L. Reis, *Macromol. Biosci.*, 2004, **4**, 743–765.
- 6 A. S. Posner, A. Perloff and A. F. Diorio, *Acta Crystallogr.*, 1958, **11**, 308–309.
- 7 R. Z. LeGeros, *Clin. Orthop. Relat. Res.*, 2002, 81–98.
- 8 P. V. Giannoudis, H. Dinopoulos and E. Tsiridis, *Injury*, 2005, **36**, S20–S27.
- 9 R. Jugdaohsingh, *J. Nutr. Heal. Aging*, 2007, **11**, 99–110.
- 10 S. J. Whiting and H. H. Draper, *J. Nutr.*, 1981, **111**, 1721–1726.
- 11 W. J. Landis, D. D. Lee, J. T. Brenna, S. Chandra and G. H. Morrison, *Calcif. Tissue Int.*, 1986, **38**, 52–59.
- 12 M. Chirita, *J. Bionic Eng.*, 2008, **5**, 149–158.
- 13 H. Li and J. Chang, *Acta Biomater.*, 2013, **9**, 6981–6991.
- 14 I. R. Gibson, S. M. Best and W. Bonfield, *J. Biomed. Mater. Res.*, 1999, **44**, 422–428.
- 15 F. Balas, J. Pérez-Pariente and M. Vallet-Regí, *J. Biomed. Mater. Res. Part A*, 2003, **66A**, 364–375.
- 16 P. Saravanapavan and L. L. Hench, *J. Non. Cryst. Solids*, 2003, **318**, 1–13.

- 17 T. Kokubo, M. Shigematsu, Y. Nagashima, M. Tashiro, T. Nakamura, T. Yamamuro and S. Higashi, *Bull. Inst. Chem. Res.*, 1982, **60**, 260–268.
- 18 H. M. Kim, T. Himeno, T. Kokubo and T. Nakamura, *Biomaterials*, 2005, **26**, 4366–4373.
- 19 A. Sousa, K. C. Souza and E. M. B. Sousa, *Acta Biomater.*, 2008, **4**, 671–679.
- 20 S. Yamada, M. Nishikawa and M. Tagaya, *Mater. Lett.*, 2018, **211**, 220–224.
- 21 T. Kataoka, K. Shiba, L. Y. Wang, S. Yamada and M. Tagaya, *RSC Adv.*, 2017, **7**, 19479–19485.
- 22 K. Nakata, T. Kubo, C. Numako, T. Onoki and A. Nakahira, *Mater. Trans.*, 2009, **50**, 1046–1049.
- 23 S. H. Kim, *Biomaterials*, 2003, **24**, 1389–1398.
- 24 A. M. Pietak, J. W. Reid, M. J. Stott and M. Sayer, *Biomaterials*, 2007, **28**, 4023–4032.
- 25 J. L. Xu and K. A. Khor, *J. Inorg. Biochem.*, 2007, **101**, 187–195.
- 26 K. Nakata, T. Kubo, C. Numako, T. Onoki and A. Nakahira, *Mater. Trans.*, 2009, **50**, 1046–1049.
- 27 X. W. Li, H. Y. Yasuda and Y. Umakoshi, *J. Mater. Sci. Mater. Med.*, 2006, **17**, 573–581.
- 28 M. Tagaya, T. Ikoma, N. Hanagata and J. Tanaka, *Mater. Express*, 2012, **2**, 1–22.
- 29 B. Kasemo, *Surf. Sci.*, 2002, **500**, 656–677.
- 30 W. F. Newman and M. W. Newman., *Arthritis Rheum.*, 1958, **1**, 473–474.
- 31 M. Tanaka and K. Sato, *Netsu Sokutei*, 2012, **39**, 151–157.
- 32 M. Tanaka, T. Hayashi and S. Morita, *Polym. J.*, 2013, **45**, 701–710.
- 33 H. Frauenfelder, P. W. Fenimore and B. H. McMahon, *Biophys. Chem.*, 2002, **98**, 35–48.
- 34 B. Bagchi, *Chem. Rev.*, 2005, **105**, 3197–3219.
- 35 J. Israelachvili and H. Wennerström, *Nature*, 1996, **379**, 219–225.
- 36 M. Tanaka, A. Mochizuki, T. Shiroya, T. Motomura, K. Shimura, M. Onishi and Y. Okahata, *Colloids Surfaces A Physicochem. Eng. Asp.*, 2002, **203**, 195–204.
- 37 M. Tanaka and A. Mochizuki, *J. Biomed. Mater. Res. - Part A*, 2004, **68**, 684–695.
- 38 S. Yamada, S. Motozuka and M. Tagaya, *J. Mater. Chem. B*, 2020, **8**, 1524–1537.
- 39 S. Yamada, T. Kobashi and M. Tagaya, *J. Mater. Chem. B*, 2021, **9**, 1896–1907.
- 40 O. Tirosh, Y. Barenholz, J. Katzhendler and A. Prieval, *Biophys. J.*, 1998, **74**, 1371–1379.
- 41 I. Sugiyama and Y. Sadzuka, *Drug Deliv. Syst.*, 2016, **31**, 275–282.
- 42 S. Schöttler, G. Becker, S. Winzen, T. Steinbach, K. Mohr, K. Landfester, V. Mailänder and F. R. Wurm, *Nat. Nanotechnol.*, 2016, **11**, 372–377.
- 43 B. Thierry, L. Zimmer, S. McNiven, K. Finnie, C. Barbé and H. J. Griesser, *Langmuir*, 2008, **24**, 8143–8150.
- 44 T. J. Daou, L. Li, P. Reiss, V. Jossierand and I. Texier, *Langmuir*, 2009, **25**, 3040–3044.
- 45 M. G. Patino, M. E. Neiders, S. Andreana, B. Noble and R. E. Cohen, *Implant Dent.*, 2002, **11**, 280–285.

- 46 D. A. Wahl and J. T. Czernuszka, *Eur. Cells Mater.*, 2006, **11**, 43–56.
- 47 R. Z. Wang, F. Z. Cui, H. B. Lu, H. B. Wen, C. L. Ma and H. D. Li, *J. Mater. Sci. Lett.*, 1995, **14**, 490–492.
- 48 C. M. Serre, M. Papillard, P. Chavassieux and G. Boivin, *Biomaterials*, 1993, **14**, 97–106.
- 49 J. Xie, M. J. Baumann and L. R. McCabe, *J. Biomed. Mater. Res. - Part A*, 2004, **71**, 108–117.
- 50 K. D. Johnson, K. E. Frierson, T. S. Keller, C. Cook, R. Scheinberg, J. Zerwekh, L. Meyers and M. F. Sciadini, *J. Orthop. Res.*, 1996, **14**, 351–369.
- 51 S. F. El-Amin, H. H. Lu, Y. Khan, J. Burems, J. Mitchell, R. S. Tuan and C. T. Laurencin, *Biomaterials*, 2003, **24**, 1213–1221.
- 52 S. Deshmukh, A. Dive, R. Moharil and P. Munde, *J. Oral Maxillofac. Pathol.*, 2016, **20**, 276.
- 53 W. Traub, A. Yonath and D. M. Segal, *Nature*, 1969, **221**, 914–917.
- 54 T. J. Wess, A. P. Hammersley, L. Wess and A. Miller, *J. Mol. Biol.*, 1998, **275**, 255–267.
- 55 J. Gaar, R. Naffa and M. Brimble, *Org. Chem. Front.*, 2020, **7**, 2789–2814.
- 56 A. Monshi, M. R. Foroughi and M. R. Monshi, *World J. Nano Sci. Eng.*, 2012, **02**, 154–160.
- 57 N. Puvvada, P. K. Panigrahi and A. Pathak, *Nanoscale*, 2010, **2**, 2631–2638.
- 58 H. Yu, K. Liu, F. Zhang, W. Wei, C. Chen and Q. Huang, *Silicon*, 2017, **9**, 543–553.
- 59 A. Rawal, X. Wei, M. Akinc and K. Schmidt-Rohr, *Chem. Mater.*, 2008, **20**, 2583–2591.
- 60 H. Kaji, K. Nakanishi, N. Soga and F. Horii, *J. Non. Cryst. Solids*, 1992, **145**, 80–84.
- 61 G. Gasquères, C. Bonhomme, J. Maquet, F. Babonneau, S. Hayakawa, T. Kanaya and A. Osaka, *Magn. Reson. Chem.*, 2008, **46**, 342–346.
- 62 G. Sauerbrey, *Zeitschrift für Phys.*, 1959, **155**, 206–222.
- 63 S. Yamada and M. Tagaya, *Mater. Lett.*, 2017, **209**, 441–445.
- 64 J. Xu, D. F.R. Gilson and I. S. Butler, *Spectrochim. Acta Part A Mol. Biomol. Spectrosc.*, 1998, **54**, 1869–1878.
- 65 A. K. Kronenberg and G. H. Wolf, *Tectonophysics*, 1990, **172**, 255–271.
- 66 F. M. Ernsberger, *J. Am. Ceram. Soc.*, 1977, **60**, 91–92.
- 67 M. Bredol, D. Leers, L. Bosselaar and M. Hutjens, *J. Light. Technol.*, 1990, **8**, 1536–1540.
- 68 R. D. Aines and G. R. Rossman, *Am. Mineral.*, 1984, **69**, 1116–1126.
- 69 S. Nakashima, S. Ohki and S. Ochiai, *Geochem. J.*, 1989, **23**, 57–64.
- 70 J. R. Collins, *Phys. Rev.*, 1939, **55**, 470–472.
- 71 B. A. Morrow, I. A. Cody and L. S. M. Lee, *J. Phys. Chem.*, 1976, **80**, 2761–2767.
- 72 G. E. Walrafen and S. R. Samanta, *J. Chem. Phys.*, 1978, **69**, 493.
- 73 L. Berzina-Cimdina and N. Borodajenko, in *Infrared Spectroscopy - Materials Science, Engineering and Technology*, InTech, 2012.

- 74 M. V Voinova, M. Rodahl, M. Jonson and B. Kasemo, *Phys. Scr.*, 1999, **59**, 391–396.
- 75 F. Höök, B. Kasemo, T. Nylander, C. Fant, K. Sott and H. Elwing, *Anal. Chem.*, 2001, **73**, 5796–5804.
- 76 N. J. Cho, K. K. Kanazawa, J. S. Glenn and C. W. Frank, *Anal. Chem.*, 2007, **79**, 7027–7035.
- 77 H. Stadler, M. Mondon and C. Ziegler, *Anal. Bioanal. Chem.*, 2003, **375**, 53–61.
- 78 G. Steiner, S. Tunc, M. Maitz and R. Salzer, *Anal. Chem.*, 2007, **79**, 1311–1316.
- 79 Y. Liu, M. X. Xie, J. Kang and D. Zheng, *Spectrochim. Acta - Part A Mol. Biomol. Spectrosc.*, 2003, **59**, 2747–2758.
- 80 J. Vogel, C. Russel, G. Gunther, P. Hartmann, F. Vizethum and N. Bergner, *J. Mater. Sci. Mater. Med.*, 1996, **7**, 495–499.
- 81 Y. Koide, K. Kubo, T. Sekine, Y. Mizushita, N. Ganbaater and T. HayashiI, *Hyomen Kagaku*, 2013, **34**, 494–499.
- 82 R. Gref, M. Lück, P. Quellec, M. Marchand, E. Dellacherie, S. Harnisch, T. Blunk and R. H. Müller, *Colloids Surfaces B Biointerfaces*, 2000, **18**, 301–313.
- 83 R. Michel, S. Pasche, M. Textor and D. G. Castner, *Langmuir*, 2005, **21**, 12327–12332.
- 84 S. I. Jeon, J. H. Lee, J. D. Andrade and P. G. De Gennes, *J. Colloid Interface Sci.*, 1991, **142**, 149–158.
- 85 S. Pasche, J. Vörös, H. J. Griesser, N. D. Spencer and M. Textor, *J. Phys. Chem. B*, 2005, **109**, 17545–17552.
- 86 S. J. Sofia, V. Premnath and E. W. Merrill, *Macromolecules*, 1998, **31**, 5059–5070.
- 87 T. G. P. Galindo, I. Yamada, S. Yamada and M. Tagaya, *Mater. Chem. Phys.*, 2019, **221**, 367–376.
- 88 Y. K. Sung, D. E. Gregonis, M. S. John and J. D. Andrade, *J. Appl. Polym. Sci.*, 1981, **26**, 3719–3728.
- 89 S. J. Kim, S. J. Park and S. I. Kim, *React. Funct. Polym.*, 2003, **55**, 53–59.
- 90 C. Gullekson, L. Lucas, K. Hewitt and L. Kreplak, *Biophys. J.*, 2011, **100**, 1837–1845.
- 91 A. T. Nielsen and W. J. Houlihan, in *Organic Reactions*, John Wiley & Sons, Inc., Hoboken, NJ, USA, 2011, pp. 1–438.
- 92 P. Dutov, O. Antipova, S. Varma, J. P. R. O. Orgel and J. D. Schieber, *PLoS One*, 2016, **11**, 1–13.
- 93 M. Tagaya, T. Ikoma, N. Hanagata, T. Yoshioka and J. Tanaka, *Sci. Technol. Adv. Mater.*, 2011, **12**, 034411.
- 94 A. J. Heim, W. G. Matthews and T. J. Koob, *Appl. Phys. Lett.*, 2006, **89**, 3–5.
- 95 M. P. E. Wenger, L. Bozec, M. A. Horton and P. Mesquidaz, *Biophys. J.*, 2007, **93**, 1255–1263.

- 96 L. Yang, K. O. Van Der Werf, C. F. C. Fitié, M. L. Bennink, P. J. Dijkstra and J. Feijen, *Biophys. J.*, 2008, **94**, 2204–2211.
- 97 L. Yang, C. F. C. Fitié, K. O. van der Werf, M. L. Bennink, P. J. Dijkstra and J. Feijen, *Biomaterials*, 2008, **29**, 955–962.
- 98 C. A. Grant, D. J. Brockwell, S. E. Radford and N. H. Thomson, *Appl. Phys. Lett.*, 2008, **92**, 23–25.
- 99 S. H. Rhee, J. Do Lee and J. Tanaka, *J. Am. Ceram. Soc.*, 2000, **83**, 2890–2892.
- 100 C. M. Botelho, R. A. Brooks, T. Kawai, S. Ogata, C. Ohtsuki, S. Best, M. A. Lopes, J. D. Santos, N. Rushton and W. Bonfield, *Key Eng. Mater.*, 2005, **284–286**, 461–464.
- 101 H. I. Kim, J. G. Kushmerick, J. E. Houston and B. C. Bunker, *Langmuir*, 2003, **19**, 9271–9275.
- 102 M. Takeya, T. Tanaka, Y. Kuzuma and T. Nawa, *Cem. Sci. Concr. Technol.*, 2017, **71**, 486–493.
- 103 H. Kitano, K. Ichikawa, M. Ide, M. Fukuda and W. Mizuno, *Langmuir*, 2001, **17**, 1889–1895.
- 104 M. Matsuguchi, S. Umeda, Y. Sadaoka and Y. Sakai, *Sensors Actuators B Chem.*, 1998, **49**, 179–185.
- 105 T. Sekine, S. Asatyas, T. Nyu, G. Lkhamsuren, A. Tsunoi, C. Sato, S. Morita, M. Tanaka and T. Hayashi, *Hyomen Kagaku*, 2015, **36**, 424–429.
- 106 Y. Maeda, N. Tsukida, H. Kitano, T. Terada and J. Yamanaka, *J. Phys. Chem.*, 1993, **97**, 13903–13906.

Chapter 3

Modification of Hydroxyapatite Particles with Mesoporous Silica and Poly(ethylene glycol) and Evaluation of Their Hydration States and Albumin Interactions

Chapter 3

Modification of Hydroxyapatite Particles with Mesoporous Silica and Poly(ethylene glycol) and Evaluation of Their Hydration States and Albumin Interactions

3.1 Introduction

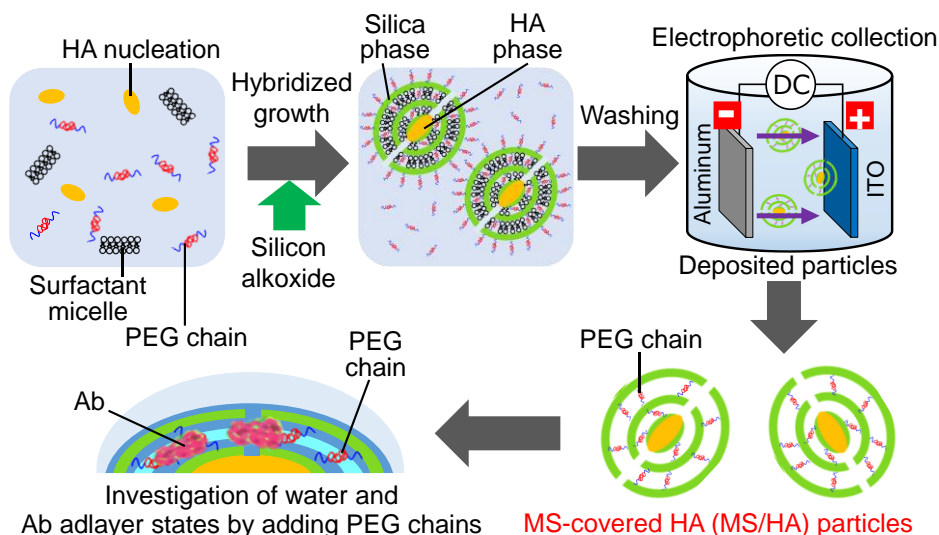
Through a surgery process for curing osteoporosis and bone tumor in a human bone tissue, the bone defect sites are sometimes generated.^{1,2} In the case, bioceramic particles are known to be useful for repairing the bone defects,³⁻⁵ and it takes long time to regenerate and integrate the surrounding tissues.⁶⁻⁸ Thus, the bioceramic particles that promote the effective bone regeneration should be developed. On the other hand, there have been the various molecules (e.g., albumin (Ab), BMP-2) that promote the bone regeneration.^{9,10} Accordingly, the effective bone regeneration by the adsorption of bone morphogenetic proteins on the bioceramic particles has been studied so far.^{11,12} For achieving the steric conformation (i.e., suppressing the denaturation) of the adsorbed proteins, it is thought to be necessary to investigate the hydration layers on the bioceramics.^{13,14} The various interactions between the intermolecular water–water and the water–ions were worked in the hydration layers,¹⁵ suggesting that the surface hydration structures can directly contribute to the adsorbed protein conformation.¹⁶⁻¹⁸ However, there has been little discussion about the relationship between the hydration layer and the protein adsorption on the bioceramic particles. Therefore, the thesis propose the importance of the controlled hydration layers and subsequently-adsorbed protein conformation states. As the candidate technique to control the surface layers, the modification by the molecules having an ethylene glycol groups can be raised.¹⁹ It has been reported that poly(ethylene glycol) (PEG) can form the stealth layers

to strongly interact the hydration layers^{20–22} and induce the specific protein adsorption. Accordingly, it is implied that the ideal adsorption states of the bone regenerative proteins can be achieved by the construction of PEG–bioceramic hybrid particle systems through the control of hydration layers. When the bioceramic particles are implanted into the human body, the enhanced biocompatibility is also required in order to prevent inflammation.²³ Therefore, the bioceramic particles that provide the controllable hydration layers and high biocompatibility should be developed.

To prepare the novel bioceramic particles with the high biocompatibility, the mimetics of the material structures and chemical compositions in the living body thought to be very important.²⁴ The low crystalline hydroxyapatite (HA, $\text{Ca}_{10}(\text{PO}_4)_6(\text{OH})_2$) nanocrystals are mainly contained in the hard tissues.^{25,26} The low crystalline HA has been focused and studied, imparting the properties such as fluorescence by the doping of a rare earth ion, unique light absorption by the hybridizing of gold nanoparticles, and antibacterial activity by the Zn-substitution.^{27–29} In order to be applicable for a drug delivery system (DDS), the HA hollow nanospheres and nanotubes were prepared using polymeric micelles as the template,³⁰ and the alginate-mediated needle-like hybrid HA nanoparticles were also synthesized under the presence of alginate.³¹ As the important points, the hard tissues *in vivo* contain a small amount of Si ion as an inorganic subcomponent. In particular, 1–2 g of Si is contained in the living body and at the concentration of 36 ppm in the bone tissue.^{32,33} Although the existence form of the Si ion in the living body and the specific role have not been elucidated, the state of the silica (SiO_2) has been suggested by an ion microscope analysis,³⁴ suggesting the importance of the silica for promoting the bone regeneration. In fact, silica is abundant in the active bone mineralization process and the skeletal growth of a rat was inhibited at no silica environment.^{35,36} Therefore, the importance of the precise design of the coexistence of HA with silica is proposed in the present paper. Based on the background above, the composites of calcium phosphate (e.g., HA) with silica glass have been studied.^{37,38} The formation of the disk between the HA and the silica indicated the partial replacement of PO_4^{3-} in HA with SiO_4^{4-} of silica at the interface and resulted in the improved bioactive properties.³⁸ Bioglass® containing phosphorus oxide and calcium oxide had the excellent affinity with bone tissue,³⁹ and Kokubo *et al.* have developed the HA–Wollastonite glass (i.e., A–W glass), which has the better mechanical strength by a wet synthesis.⁴⁰ When A–W glass is implanted into the bone defects, the biologically-active layer of bonelike apatite was spontaneously formed on the surfaces to induce the significant chemical integration with the bone tissues.⁴¹ However, there has been no reports on the bioceramic particles prepared by precisely hybridizing the low crystalline HA with silica phase. Thus, the development of the hybrid bioceramic particles should be investigated, leading to the elucidation of the interfacial mechanism between two phases.

In order to efficiently activate the surrounding bone tissues, the mesoporous silica (MS)-covered HA (MS/HA) particles were already proposed.^{42,43} The MS/HA particles had also been synthesized using PEG chains as the template for a DDS application.⁴⁴ MS synthesized from silicon alkoxide and organic supramolecular template is known to provide the regular mesostructures with the high specific surface area, and has been functionalized by the introduction of heteroelement into the silica frameworks for the enhanced bioactivity.⁴⁵⁻⁴⁷ In the previous MS studies, the control of mesostructures for the unique molecular adsorption properties has been studied for catalysis, separation, sensing and DDS applications.^{48,49} For the biomedical applications, the hydration layers on the mesopores of MS have exhibited a lowered melting point property like the behaviour of nonfreezing waters.^{50,51} Furthermore, it has been reported that the mesostructures of MS can contribute to the protein adsorption and cell adhesion.^{52,53} Based on the backgrounds, the synthetic method of the MS/HA particles have already established.^{42,43} In particular, the particles had the structures of the HA nanocrystals covered with the MS phase to exhibit the high specific surface areas, and the hydration structures formed on the surfaces were controlled to successfully suppress the protein denaturation. However, the calcination process for forming the mesopores induced the transformation in high crystalline state in the MS/HA particles and occurred the aggregation among the particles with the inhomogeneous particle shapes, indicating the low dispersibility ability in biological solution. Therefore, the low crystalline HA covered with MS that can highly disperse in biological solution should be designed for the enhanced biocompatibility.

In this study, the low crystalline HA particles were precisely hybridized with the MS phase in the presence of poly(ethylene oxide)-poly(propylene oxide)-poly(ethylene oxide) (PEG₂₀PPG₇₀PEG₂₀) triblock copolymer to synthesize the novel mesoporous bioceramic particles. With interacting of the particles with PEG chains and collecting by an electrophoretic deposition, the successful formation of the uniform particle sizes and water high dispersibility in phosphate buffer saline (PBS) were intended. Moreover, the interfacial effect on the hydration layers on the MS/HA particles on the protein adsorption and cell adhesion was investigated (**Scheme 3-1**).



Scheme 3-1. Outline of this study for preparing the MS-covered HA (MS/HA) particles and investigating the water and protein adsorption layer states by adding PEG chains.

3.2 Experimental Section

3.2.1 Chemicals

Cetyltrimethylammoniumbromide (CTAB, $C_{19}H_{42}NBr$), Dipotassium hydrogen phosphate (K_2HPO_4), 25 vol% of ammonium hydroxide, calcium chloride dihydrate ($CaCl_2 \cdot 2H_2O$), ethanol (99.5 vol%) and trypsin (0.05 w/v%)-ethylenediaminetetraacetate (0.053 M) (trypsin-EDTA) were purchased from Wako Chemical Co. Ltd. Triblock copolymer (Pluronic123, P123, $HO(CH_2CH_2O)_{20}(CH_2CH(CH_3)O)_{70}(CH_2CH_2O)_{20}H$) were purchased from Sigma-Aldrich Co. Ltd. Tetraethoxysilane (TEOS, $Si(OCH_2CH_3)_4$) was purchased from Tokyo Chemical Industry Co., Ltd. Bovine serum albumin (Ab) was purchased from Nacalai Tesque Co., Ltd. Phosphate Buffered Saline (PBS) Dulbecco's Formula (w/o Calcium, Magnesium) was purchased from DS pharma biomedical Co., Ltd. Center. Silicon (100) wafer (size: 2.4 cm \times 2.4 cm, p-type, resistivity: 16.1–18.7 Ω) was purchased from Mitsubishi Materials Trading Co., Ltd. All of the chemicals were used as received without further purification.

3.2.2 Synthesis of the Mesoporous Silica-Covered Hydroxyapatite Particles and Their Poly(ethylene glycol) Immobilization

The MS/HA particles were synthesized as follows. Cationic surfactant (CTAB) at the concentration of 103 mM was completely dispersed into 24.3 mL of ultrapure water (1.31 mmol). 12.0 mmol of K_2HPO_4 and PEG chain (P123) at the different concentrations of 0, 1.33, 2.65 and 5.30 mM was dissolved into the CTAB-dispersed solution. After adjusting the solution pH to 12

by the ammonium hydroxide, 24.3 mL of the aqueous solution containing $\text{CaCl}_2 \cdot 2\text{H}_2\text{O}$ (12.0 mmol) was added into the CTAB/PEG/ K_2HPO_4 solution at the drop rate of 1.0 mL/min. The solution in poly(propylene) vessel was continuously and vigorously stirred at 40 °C for 3 h. Then, the solution pH was adjusted to 12 by ammonium hydroxide again and 19.2 mmol of TEOS was added into the solution, and the solution was sealed in a Teflon-lined autoclave and was hydrothermally mixed at 100 °C for 12 h. The white-colored precipitation was centrifuged, washed by an ultrapure water and ethanol, and was continuously stirred in the mixture solution of ultrapure water with ethanol for 3 h.

The particles were completely dispersed in ethanol and collected by an electrophoretic deposition as follows. The soda glass substrate covered with an indium tin oxide (ITO) film (film thickness: 1500 Å, resistivity: $\geq 10 \Omega$) and aluminium foil plate were used as the working and counter electrodes, respectively. The electrode surfaces were cleaned by an exposure to UV/OZONE (ASUMI GIKEN, Limited, ASM401N) for 5 min. Then, the electrodes were immersed in the particle dispersion solution at the concentration of 1 wt% in ethanol, and a DC voltage of 100 V at the distance of 1 cm between the electrodes was applied. The deposited particles on the working electrode were collected from the surface and dried at 65 °C for 12 h as the powder state.

The PEG concentration was calculated from the relationship between the total amount of solution and the added amount of PEG chains. The resulting solid products prepared by the above method with the PEG concentration of 0, 1.33, 2.65 and 5.30 mM were defined as MS/HA-0, MS/HA-1, MS/HA-2 and MS/HA-3, respectively, which were successfully obtained by the electrophoretic collection method. As the reference samples, the solid products prepared under the same synthetic procedures without TEOS and without calcium phosphate sources were defined as HA and MS, respectively, which could not be obtained by the electrophoretic collection. Thus, the HA and MS particles without electrophoretic collection were centrifugated, washed, and dried at 65 °C for 12 h.

In the sedimentation behavior test for the particles in PBS at the higher concentration of 1 wt%, the sedimentation time effectively increased from 12 h for MS/HA-0 up to 96 h for MS/HA-1, MS/HA-2 and MS/HA-3. The hybridization with PEG chains improved the sedimentation time, although the sedimentation time was irrespective of the initial PEG concentration.

3.2.3 *Formation of Hydration Layers and Albumin Adlayers on the Particles*

In order to evaluate the hydration layer structures, the particles were dispersed in ultrapure water at the particle concentration of 1.0 mg/mL. After forming the hydration layer at room temperature for 2 h, the particles were centrifuged and freeze-dried. Subsequently, the FT-IR

spectra were measured before and after freeze-drying to evaluate the difference in the hydration layers according to **Chapter 2**.

Ab were dispersed in ultrapure water which was controlled at the pH of 7.4. The particles were dispersed in the Ab aqueous solution (28 mM) at the particle concentration of 1.0 mg/mL. The adsorption amount of Ab reached equilibrium at 37 °C for 2 h and the reaction time of this study was fixed at 2 h. After the reaction, the solids were centrifuged and freeze-dried.

The solid component of MS particles was dissolved as SiO_4^{4-} by 1.6 wt% in 2 h.⁵⁴ The particles aggregation and collapse of mesostructure was not confirmed, it was considered that the effect of dissolution was extremely low.

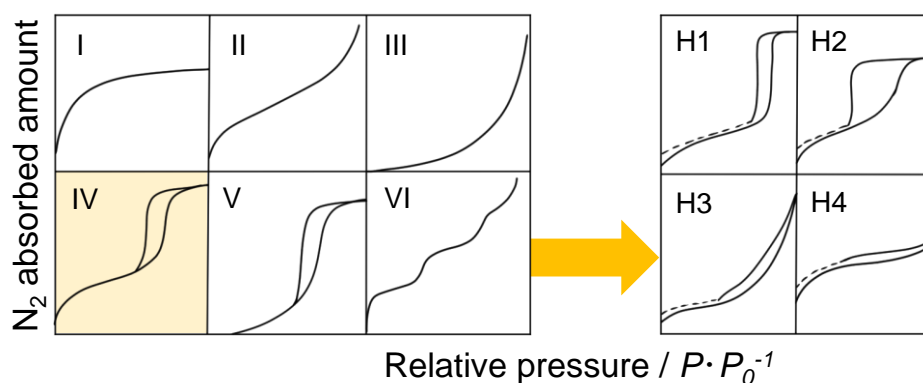
3.2.4 Characterization of the Particles

Transmission electron microscope (TEM) images were taken with a JEM-1400 (JEOL Co., Ltd.) according to **Chapter 2**. The deposited particles on the electrode were measured by a glow discharge optical emission spectrometry (GD-OES, HORIBA, Ltd., GD-Profilier2). Here, the thin particle layer formed by an ultrasonication (AS ONE Corporation, ASU-6) was analyzed. The digging depth with the measurement was determined using a surface roughness measurement device (SurfTest SJ-410, Mitutoyo Co., Ltd.) to obtain the digging rate, and the chemical composition distributions at the depth direction was calculated. The morphologies were observed using a field emission scanning electron microscope (FE-SEM: SU8000, Hitachi High-Technologies, Japan) at an accelerating voltage of 5 kV and current of 10 μA . The chemical mapping in the particles was analyzed by an energy-dispersive-spectroscopy with a software (AZtecEnergy, Oxford Instruments Co., Ltd.). The elemental compositions were characterized by an X-ray fluorescence analysis (XRF, Rigaku ZSX Primus II) according to **Chapter 2**. The evaluation of the chemical bonding states of Si and P atoms in the particles were performed by a solid state NMR spectroscopy (Avance 300wbs, BRUKER Co., Ltd.) according to **Chapter 2**. The silanol groups of the solid state ^{29}Si -NMR spectra were separated by Q_2 , Q_3 and Q_4 . Here, Q_2 (-93 ± 2 ppm) indicates two Si-O-Si and two Si-OH bonds, Q_3 (-102 ± 2 ppm) indicates three Si-O-Si and one Si-OH bonds and Q_4 (-111 ± 2 ppm) indicates four Si-O-Si bonds. This deconvolution was performed by fitting with the Gaussian function according to **Chapter 2**. All the residual values by the deconvolutions were less than 3.2 %. X-ray diffraction (XRD) patterns were recorded with an X-ray diffractometer (Smart Lab, Rigaku Co., Ltd.) and the crystallite sizes lattice parameters were calculated according to **Chapter 2**.

Infrared spectra were recorded on a Fourier transform infrared spectrometer (FT-IR, FT/IR-4600, JASCO Co., Ltd.) as the background of KBr in the range between 4000–400 cm^{-1} with an accumulation times of 64. The spectra of MS/HA particles were investigated by the FT-IR spectral deconvolution technique at the wavenumber regions between 1300–800 cm^{-1} . The adsorption

band peak due to siliceous bonding could be deconvoluted into eight components of P–OH and Si–OH ($910 \pm 5 \text{ cm}^{-1}$) P–O ($970 \pm 10 \text{ cm}^{-1}$), Si–O–P ($1008 \pm 10 \text{ cm}^{-1}$), Si–O–Si symmetric and P–O ($1030 \pm 5 \text{ cm}^{-1}$), Si–O ($1120 \pm 5 \text{ cm}^{-1}$) and Si–O–Si asymmetric ($1180 \pm 5 \text{ cm}^{-1}$) stretching vibrations, respectively.^{55,56}

Nitrogen adsorption and desorption isotherms were measured at 77 K on a BELSORP-Mini II instrument (Microtrac/BEL). Prior to the measurement, the particles were degassed under vacuum at 120 °C for 1 h. The surface area was evaluated as the Brunauer–Emmett–Teller (BET) surface area⁵⁷ and calculated Barrett-Joyner-Halenda (BJH) pore sizes.⁵⁸ The physisorption isotherms were grouped into six types by IUPAC recommendations in 1985 (**Scheme 3-2**).⁵⁹ Type I isotherms indicate microporous solids having relatively small external surfaces. Type II isotherms indicate the physisorption of most gases on nonporous or macroporous adsorbents. Type III and V isotherms indicate weak interaction between adsorbent and adsorbate, type V isotherms have pore structures in some cases. Type IV isotherms indicate mesoporous (diameter: 2–50 nm) structure. Type VI isotherms indicate layer-by-layer adsorption on a highly uniform nonporous surface. Furthermore, type IV isotherms are classified into four types by shape of hysteresis loops. The type H1 loop is found in agglomerates of spherical particles of uniform size. The type H2 loop is given by more complex pore structures in which network effects are important. The type H3 and H4 loops are found slit-shaped mesopores. The type H3 is also found in aggregates of flat particles and the type H4 may be seen in the presence of micropores. The structures of particles were considered using these classifications.

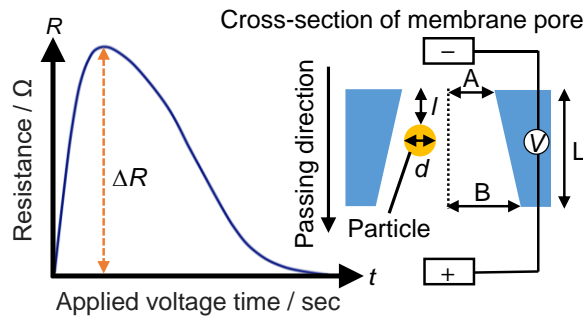


Scheme 3-2. Different types of N₂ adsorption isotherms as classified by IUPAC.⁵⁹

In the evaluation of the particles, size distribution and zeta potential were measured with a nanoparticle multianalyzer (Izon Science, Co., Ltd., qNano), which is based on the electric resistance nanopulse method. The particles were ultrasonically dispersed in PBS at a particle concentration of 50 ng/mL for the particle size evaluation. Then, the dispersion solution was used for counting 500 particles for the measurement. The average particle size (*Ave.*) and the coefficient

of variation (C_v) were calculated. Here, the current values were set to be 100–120 nA with an applied voltage of 0.66 V. As the calibration sample, the carboxylated polystyrene standard particles (Izon Science, Co., Ltd., CPC100) with the average diameter of 100 nm were placed in PBS at the concentration of 2×10^9 particles/mL and used. The outline is shown in **Scheme 3-3**, where V_0 was the supplied power voltage and V was applied voltage to the conical pores. ΔR is the resistance change, and A , B and L are the dimension sizes of pores. The particle size (d) was obtained by the following equation (3-1).⁶⁰⁻⁶²

$$d = \sqrt[3]{\frac{D^2 L \Delta R}{R}} \quad (3-1)$$



Scheme 3-3. Illustration of the resistive pulse curve to indicate the maximum resistance change (ΔR) from the baseline level with the applied voltage time. Inset: illustration of the cross-section of membrane pore structure with the passing of particle along.

The relationship of the electrophoretic velocity (v_x) of the particle x and the zeta potential is expressed by the following equation (3-2).^{63,64}

$$\frac{(v_x)_{el \text{ Sample}}}{(v_x)_{el \text{ Cal}}} = \frac{\zeta_{net \text{ Sample}}}{\zeta_{net \text{ Cal}}} \quad (3-2)$$

where $(v_x)_{el \text{ Sample}}$ and $(v_x)_{el \text{ Cal}}$ are the electrophoretic mobility of the sample particles and calibration particles, respectively. The $x_{net \text{ Sample}}$ and $x_{net \text{ Cal}}$ values are the net zeta potential of the sample particles and calibration particles, respectively. The zeta potential value of the particles at an applied pressure ($x_{P \text{ Sample}}$) can be expressed by summarizing the $x_{net \text{ Sample}}$ and membrane zeta potential (x_m) by the following equation (3-3).

$$\zeta_{P \text{ Sample}} = \zeta_{net \text{ Sample}} + \zeta_m \quad (3-3)$$

The zeta potential x^i_{Sample} of each sample particle i is given by averaging the respective zeta potential values calculated at different positions (l_x) in the pore. The l_x is the position in the pore when the particle reached at a fixed time. The zeta potential of the sample particle is estimated by taking the average of l_x at several discrete points as in the following equation (3-4).

$$\zeta^i_{\text{Sample}} = \frac{\sum_x \zeta^i_{x \text{ Sample}}}{\sum_x} = \frac{\sum_x (v^i_{x \text{ Sample}} - v^P_{x \text{ cal}}) / (v^V_{x \text{ cal}} V)}{\sum_x} \zeta_{net \text{ Cal}} + \zeta_m \quad (3-4)$$

where v_{xS}^i is the sum of the time averaged electro kinetic and convection velocity components of the sample particulates at the position of l_x within the pore by the following equation (3-5).

$$v_{xS}^i = \frac{l_x}{T_x^i} = \frac{\int_0^{T_x^i} v^i(t) dt}{T_x^i} \quad (3-5)$$

where $v_{x\text{cal}}^P$ is the convective velocity per unit pressure, $v_{x\text{cal}}^V$ is the electro kinetic velocity per unit voltage, P is the applied pressure and V is the measurement voltage. P and V are parameters at the particle size measurement. $v_{x\text{cal}}^P$ and $v_{x\text{cal}}^V$ are determined at particle size measurement. By measuring the calibration particles in addition to the sample particles of this study, the zeta potential can be measured.⁶⁵

3.2.5 FT-IR Spectral Deconvolutions for Analyzing the Hydration States

The hydration structures on the particles were investigated by the FT-IR spectral deconvolution technique at the wavenumber regions between 3850–2800 cm^{-1} according to Chapter 2. In particular, the O–H stretching band broadened by Fermi resonance was deconvoluted into three components of (I) $3200 \pm 20 \text{ cm}^{-1}$, (II) $3400 \pm 20 \text{ cm}^{-1}$ and (III) $3600 \pm 20 \text{ cm}^{-1}$, belonging to (I) free,¹⁶ (II) intermediate and (III) nonfreezing water molecules, respectively. This deconvolution was performed by fitting with the Gaussian function according to Chapter 2. The FT-IR spectra before and after freeze-drying are shown in the Figure 3-1. When the FT-IR spectra of MS/HA-0 and MS/HA-3 particles before and after the drying were

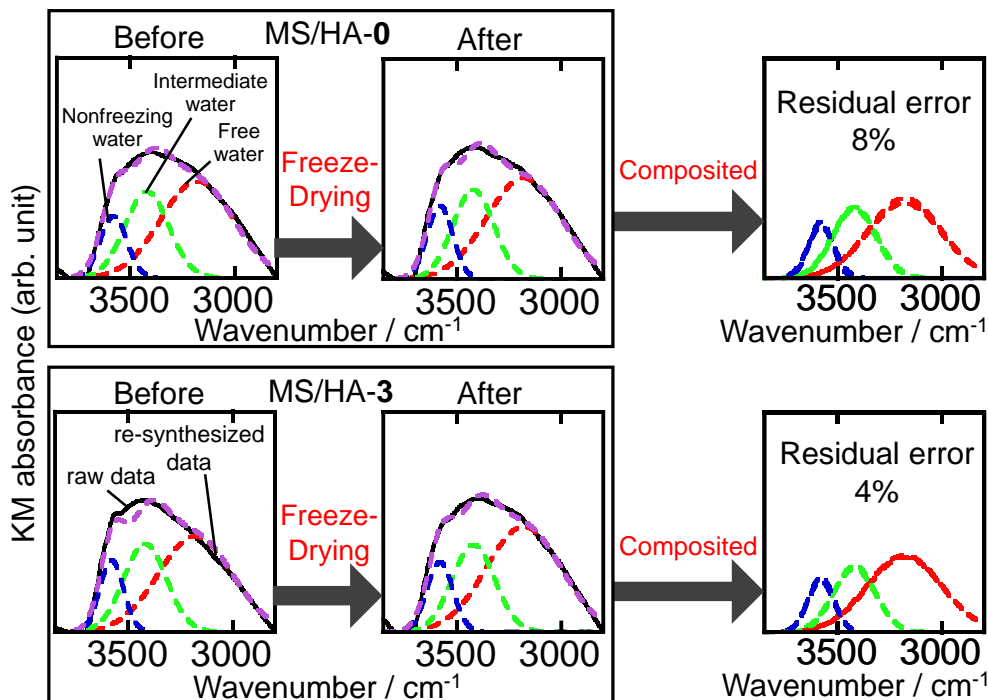


Figure 3-1. FT-IR spectral deconvolution results of three hydration layers formed on the particles before and after freeze-drying.

synthesized, no significant change of the peak height, full width at half maximum and wavenumber were observed (residual errors of 8 %). From the results, the FT-IR spectra after the freeze-drying were used for evaluation and discussion in this chapter. Furthermore, (IV) N–H stretching vibration of Col ($3300 \pm 20 \text{ cm}^{-1}$) was added to the attribution of the Col adsorbed particles. The hydration states of the Col adsorbed particles were discussed through the three components of water and the N–H stretching vibration of Col.

Furthermore, the spectra were deconvoluted into six components in order to clarify the detailed hydration structures and hydroxy group in HA of the particles according to **Chapter 2**. Here, all the residual values by the deconvolutions were less than 2.4 %. From the separated spectra, the ratio of the mono-component area was calculated. In order to evaluate the hydration layer states in detail, the ratio of the asymmetric stretching vibration component ratio (R_{as}) was determined with the component ratio of “(1) asymmetric O–H stretching vibration between water molecules” (compo(1)) by that of “(3) symmetric O–H stretching vibration of water molecules” (compo(3)) as shown in the following equation (2-4). The asymmetric stretching vibration component ratio for the particles reacted with PBS and PBS containing Ab were evaluated to be abbreviated as R_{as} and $R_{as} (Ab \text{ ad})$.

3.2.6 Evaluation of the Albumin Adsorption Amounts

The supernatant liquids after the Ab adsorption onto the particles were optically measured by the change in the absorbance at 278 nm, which was determined by a UV-Visible spectrophotometer (JASCO Co., Ltd., V-750) as shown in the spectra (**Figure 3-2 (a)**). Thus, the calibration curve of the Ab dispersion liquids with the different concentrations of 28, 22, 17, 11 and 5.5 μM were obtained as shown in the **Figure 3-2 (b)** to be the correlation coefficient of 0.9993. The protein adsorption amount on the particles were calculated using the calibration curve. The protein adsorption amount was normalized by both weight and BET surface area of the particles.

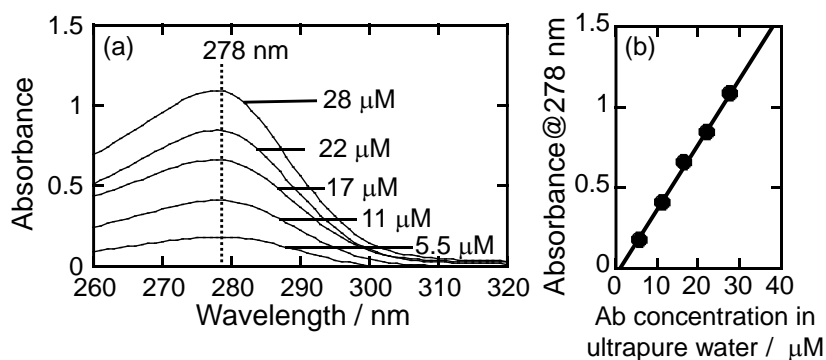


Figure 3-2. (a) UV-Visible absorption spectra of the Ab in ultrapure water with the different concentrations, and (b) their calibration curves between the concentration and absorbance ($R^2=0.99913$).

3.2.7 FT-IR Spectral Deconvolution for Analyzing the Albumin Adlayers

For evaluating the secondary structures of the adsorbed Ab on the particles, the FT-IR spectra of the freeze-dried particles containing the protein adsorption layers were measured and deconvoluted under the same techniques and conditions described above at the wavenumber between 1735–1600 cm^{-1} . The spectra were secondarily differentiated in the same way as in **Chapter 2**, The C=O stretching band was deconvoluted into six components ((i) 1634.9, (ii) 1645.8–1649.8, (iii) 1655.1–1659.9, (iv) 1668.8–1167.5, (v) 1684.3–1684.5 and (vi) 1692.7–1699.7 cm^{-1}) belonging to (i) β -sheet,^{66,67} (ii) random, (iii) α -helix, (iv) turn, (v) β -turn (1) and (vi) β -turn (2), respectively. Here, the difference spectra were obtained to eliminate the influence of the O–H bending vibration of water molecules (1635 cm^{-1}). In particular, the difference spectrum could be obtained by subtracting the spectrum before the Ab adsorption from the spectrum after the Ab adsorption, and it was deconvoluted into six components mentioned above. The deconvolution was performed by fitting with the Gaussian functions. As the reference, the spectrum of Ab alone without the further purifications was measured and deconvoluted under the same techniques and conditions described above. The deconvolution result was shown in the **Figure 3-3**.

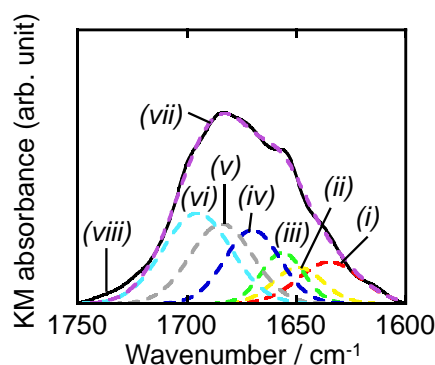


Figure 3-3. FT-IR spectral deconvolution results of the amide I absorption band of Ab, and their secondary structural components ((i): β -sheet, (ii): random, (iii): α -helix, (iv): turn, (v)(vi): β -turn), and their (vii) re-synthesized and (viii) raw spectra.

As a result, the component ratios of Ab alone were shown as follows. (i) β -sheet was 11.9 %, (ii) Random was 8.2 %, (iii) α -helix was 9.9 %, (iv) Turn was 18.8 %, (v) β -turn (1) was 22.9 % and (vi) β -turn (2) 28.4 %, respectively. In all the deconvolutions, the SOLVER option described above was used. The residual values by the deconvolutions were less than 3.7 %. Here, compo(α -helix) and compo(β -sheet) were attributed to native state components, and compo(turn) and compo(random) were attributed to denatured state components. From the viewpoints, native state component ratios were evaluated by the following equation (3-6).

$$\text{Native state component ratios} = \frac{\text{compo}(\alpha\text{-helix}) + \text{compo}(\beta\text{-sheet})}{\text{compo}(\text{turn}) + \text{compo}(\text{random})} \quad (3-6)$$

3.3 Results and Discussion

3.3.1 Characterization Results of the Mesoporous Silica-Covered Hydroxyapatite Particles

Figure 3-4 shows the TEM images of HA, MS and the MS/HA particles. The HA particles exhibited the needle-like shapes, and the sizes were $28.5 \pm 3.3 \text{ nm} \times 18.2 \pm 2.4 \text{ nm}$. The MS particles exhibited the concentric mesostructures. In the MS/HA particles, the needle-like HA were clearly covered with MS phase, suggesting that the particle had a core-shell-like structures. The thickness of MS phase that covered over the HA particles was approximately $5.2 \pm 1.7 \text{ nm}$. The needle-like HA particles in the MS/HA particles had the shape sizes of $29.8 \pm 2.5 \text{ nm} \times 6.3 \pm 1.2 \text{ nm}$, which almost matched to the crystallite sizes, indicating that the core HA was single crystal in MS/HA particles. The MS phase was precipitated by interacting with the HA particles to form the necking between the HA particles. Therefore, the low crystalline HA was hybridized with the MS phase and the surfaces of the MS/HA particles were covered with the MS phase.

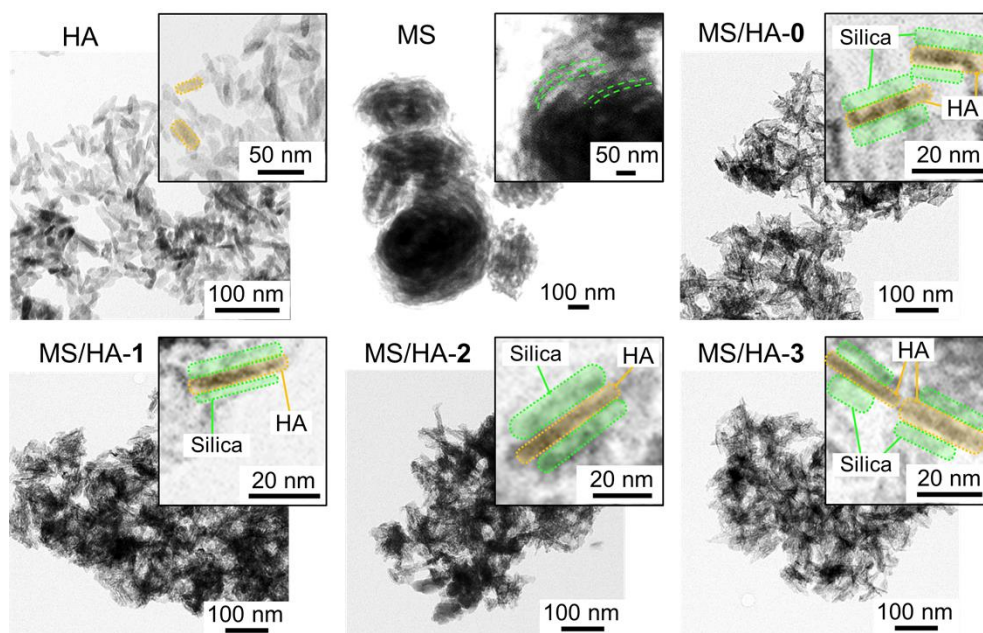


Figure 3-4. TEM images of HA, MS and the MS/HA particles (inset: magnified images). In MS, green dotted line indicated the concentric mesostructures. In MS/HA, yellow part and green part indicated HA and silica, respectively.

Figure 3-5 (a) shows the representative chemical composition profiles of the MS/HA particle (MS/HA-3), which were measured by a GD-OES analysis. The substrate surface that covered with the MS/HA particles by an electrophoretic collection method was used, and the depth profiles vertical to the substrate plane were measured. When the depth profiles for the Ca, H, Si, and P atoms were compared, that of the Si atom was observed near the surface. As compared

between the Ca, Si and P atoms, the MS phase would be formed on the outside HA phase. As shown in the SEM and EDS elemental mapping images in **Figure 3-5 (b)**, the Si, O, Ca and P elements were uniformly distributed on the particles and were existed along with the particle shape.

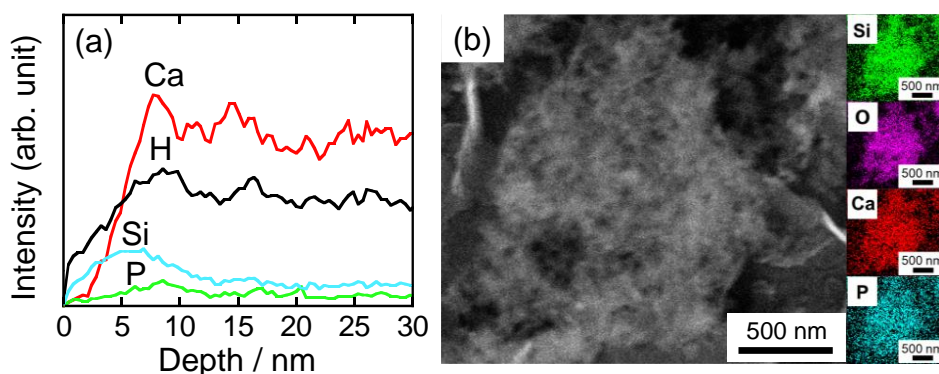


Figure 3-5. (a) Representative chemical composition profiles of the MS/HA particles (MS/HA-3), which were measured by a GD-OES analysis, and (b) the SEM and EDS elemental mapping images of Si, O, Ca and P, which were detected at 1.739 keV, 0.525 keV, 3.690 keV and 2.013 keV of $K\alpha_1$ lines.

Table 3-1 shows the resultant chemical compositions of HA and the MS/HA particles, and their Ca/P and Ca/Si molar ratios and Si wt%, which were measured by an XRF analysis. The MS/HA particles significantly contained the Ca, P and Si elements. The resultant Ca/P molar ratios of the MS/HA particles (1.86–1.87) and HA (1.77) were higher than those of the feed Ca/P molar ratios, where the initial Ca/P molar ratio was 1.00. The result is thought to be caused by replacing PO_4^- with carbonate ions at the interface and approaching the stoichiometric ratio of HA. Therefore, it was found that the chemical compositions of the synthesized MS/HA particles were similar to that of the autogenous bone with HA as the main component. Furthermore, the addition of PEG chains caused the increase in the Ca/Si molar ratio, suggesting that the presence

Table 3-1. Resultant their Ca/P and Ca/Si molar ratios and Ca/Si weight ratios of HA and the nanostructured MS/HA hybrid particles, which were measured by an XRF analysis.

	Ca/P (molar ratio)	Ca/Si (molar ratio)	Si wt%
HA	1.77	–	–
MS/HA-0	1.86	0.77	43.6
MS/HA-1	1.87	0.77	43.6
MS/HA-2	1.87	0.82	42.2
MS/HA-3	1.87	0.83	42.0

of PEG chains affect the formation of the MS phase in the particles. The Si wt% was 42.0–43.6, it was suggesting the coexistence of the calcium phosphate phase and the silica phase.

Figure 3-6 (a) shows the solid state ^{29}Si -NMR spectral deconvolution results of MS and the MS/HA particles. Q_2 (i.e., two Si–O–Si and two Si–OH bonds), Q_3 (i.e., three Si–O–Si and one Si–OH bonds) and Q_4 (i.e., four Si–O–Si bonds) were detected, but Q_0 (i.e., SiO_4^{4-} substituted with HA crystalline lattice or spherical silicate clusters in HA structure) was not detected. Therefore, it is considered that silicate exists as silica phase in the MS/HA particles instead of silicate ions. Furthermore, since Si–OH is abundantly exist on the MS/HA particle surfaces, it can be reaction site with the HA phases. **Figure 3-5 (b)** shows the solid state ^{31}P -NMR spectra of HA and the MS/HA particles. The chemical shift peak of ammonium dihydrogen phosphate as the reference sample was detected at 1.0 ppm. The intensity of the spectrum of HA was low and exhibited the peak at 0.4 ppm, which can be assigned to the crystalline HA. The spectra of the MS/HA particles exhibited the peak at 2.7 ppm, which can be assigned the distorted HA.⁶⁸

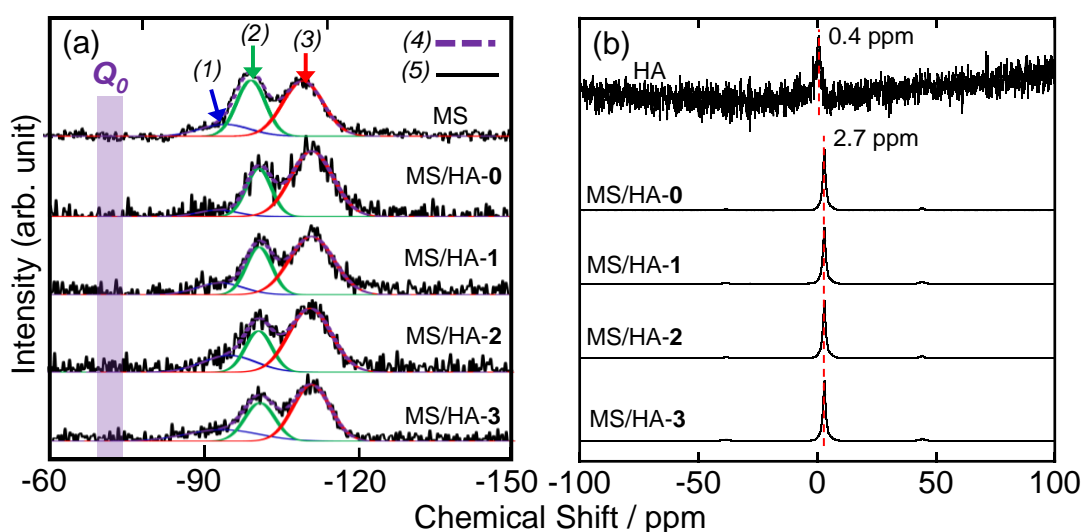


Figure 3-6. (a) Solid state ^{29}Si -NMR spectral deconvolution results of MS and the MS/HA particles, indicating the separated spectra of (1) Q_2 (i.e., two Si–O–Si and two Si–OH bonds) at -93 ± 2 ppm, (2) Q_3 (i.e., three Si–O–Si and one Si–OH bonds) at -102 ± 2 ppm and (3) Q_4 (i.e., four Si–O–Si bonds) at -111 ± 2 ppm, and (4) their re-synthesized and (5) raw spectra. (b) Solid state ^{31}P -NMR spectra of HA and the MS/HA particles.

Figure 3-7 (a) shows the XRD patterns of HA, MS and the MS/HA particles at the higher 2θ regions. All the patterns of the particles were attributed to a single phase of HA ($\text{Ca}_{10}(\text{PO}_4)_6(\text{OH})_2$, ICDD:00–009–0432), and exhibited the low crystallinity. Since the silica amorphous halo pattern was also observed in the MS/HA particles in addition of MS, it has been shown that the particles have HA phase and silica phase. **Figure 3-7 (b)** shows the XRD patterns of the MS particles at the lower 2θ regions, indicating the diffractions of the index as 100, 110,

200 and 210 reflections of a layered mesostructures with the d -spacing values of 3.9, 2.3, 2.0 and 1.5 nm, respectively. The diffractions due to the hexagonal structure could not be confirmed in the MS/HA particles.

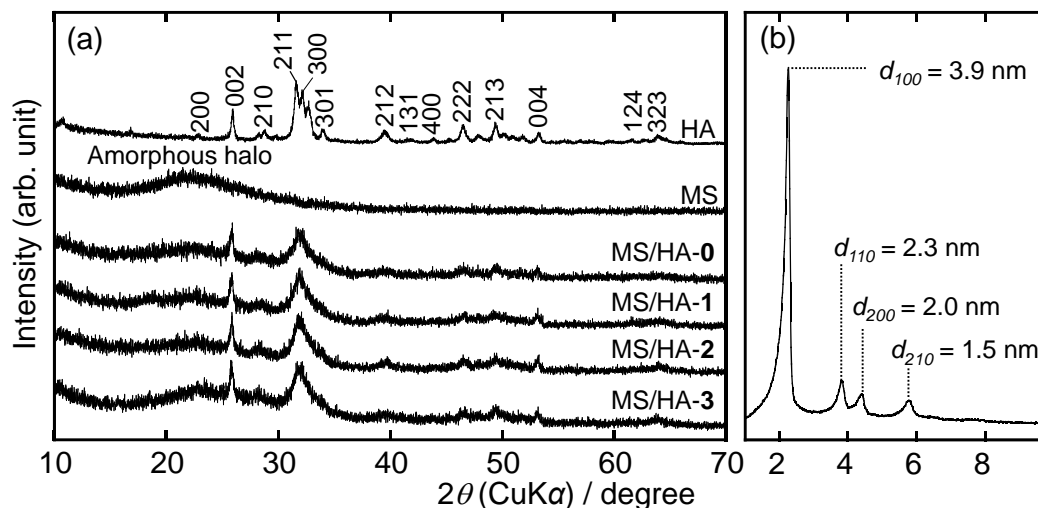


Figure 3-7. (a) XRD patterns of HA, MS and the nanostructured MS/HA hybrid particles at higher 2θ regions, which can be attributed to the crystalline phase of HA ($\text{Ca}_{10}(\text{PO}_4)_6(\text{OH})$, ICDD:00-009-0432). (b) XRD patterns of MS particles at the lower 2θ region.

The crystallite sizes and lattice constants of the particles were analyzed from XRD patterns. In HA, the crystallite sizes of D_{002} and D_{300} and the ratio of D_{002}/D_{300} were 28 and 21 nm and 1.3. In MS/HA-0, the D_{002} , D_{300} and D_{002}/D_{300} values were 29, 4.3 nm and 6.7. In MS/HA-3, the D_{002} , D_{300} and D_{002}/D_{300} values were 26, 5.4 nm and 4.9. The crystallite ratio (D_{002}/D_{300}) significantly increased 3.8–5.2 times with the hybridization of HA with MS. It is considered that the interactions between the ions (calcium and phosphate) of HA and the CTAB micelle would occur at the heterogeneous nucleation stage.⁶⁹ In addition, the negatively-charged TEOS specifically interacted with the a -plane of the HA crystal surfaces to effectively inhibit the crystal growth in the direction of a -axis.

Figure 3-8 (a) shows the FT-IR spectra of HA, MS and the MS/HA particles. **Table 3-2** shows the peak assignments of the FT-IR spectra of the MS/HA particles. In all the particles, the O–H stretching vibration bands of absorbed water appeared at 2800–3800 cm^{-1} . The C–H stretching vibration bands of the PEG molecules appeared at 2925 and 2850 cm^{-1} . **Figure 3-8 (b–g)** shows FT-IR spectral deconvolution results of chemical bonds at 800–1300 cm^{-1} . In HA, the P–O stretching vibration bands appeared at 1040 and 970 cm^{-1} . The P–OH stretching vibration bands appeared at 910 cm^{-1} . The band originated from the O–P–O bending mode appeared at 605 and 265 cm^{-1} .²⁵ In MS, the Si–O–Si asymmetric and symmetric stretching vibration bands appeared at 1170 and 1030 cm^{-1} , respectively. The Si–O stretching vibration bands appeared at

1120 cm^{-1} . The Si–OH stretching vibration bands appeared at 910 cm^{-1} . The Si–O–P symmetric stretching vibration bands have been known to be appeared at 1008 cm^{-1} .⁷⁰ Here, it is assumed that the Si–OH of the MS phase and P–OH of the HA phase were reacted to form the Si–O–P bond.

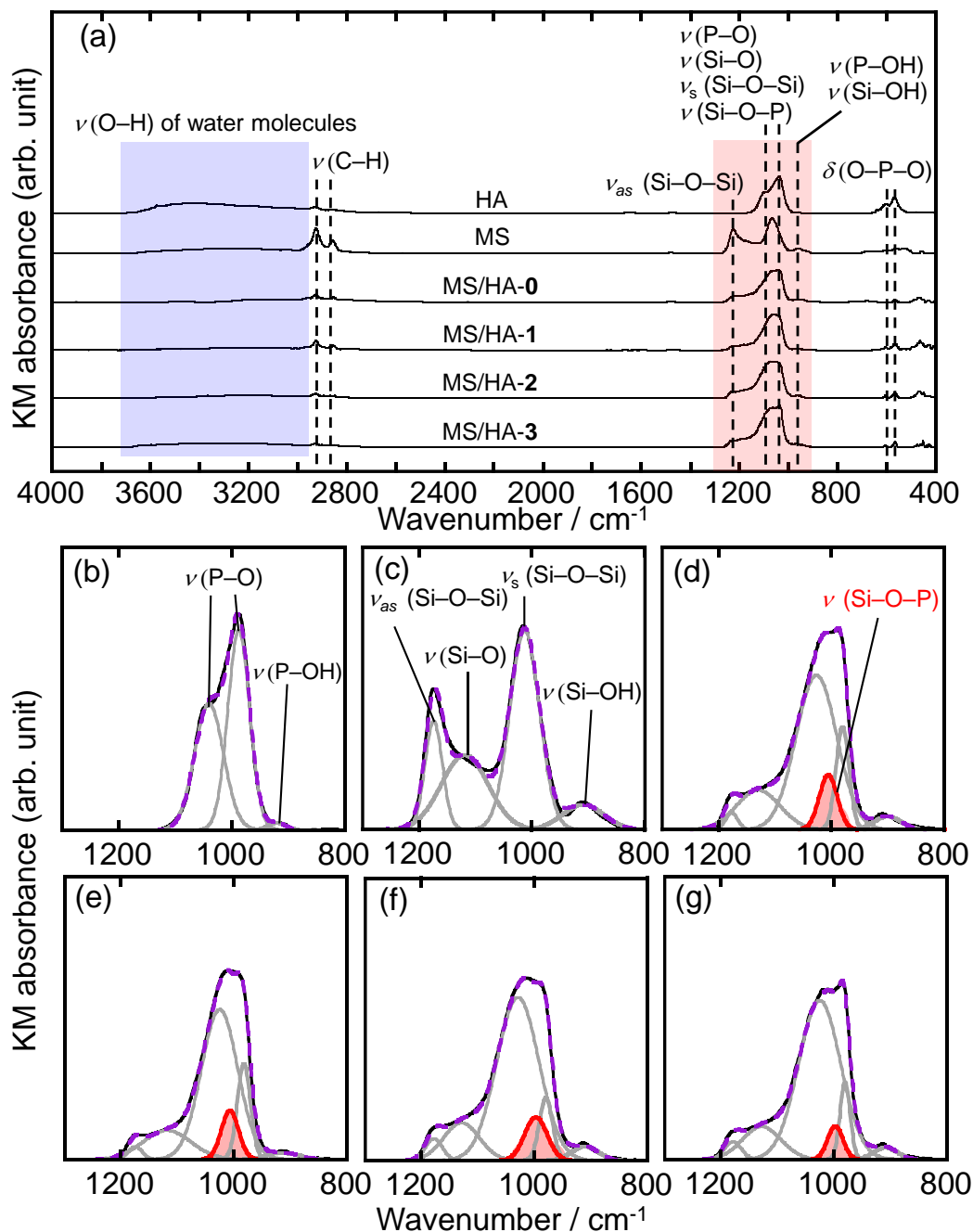
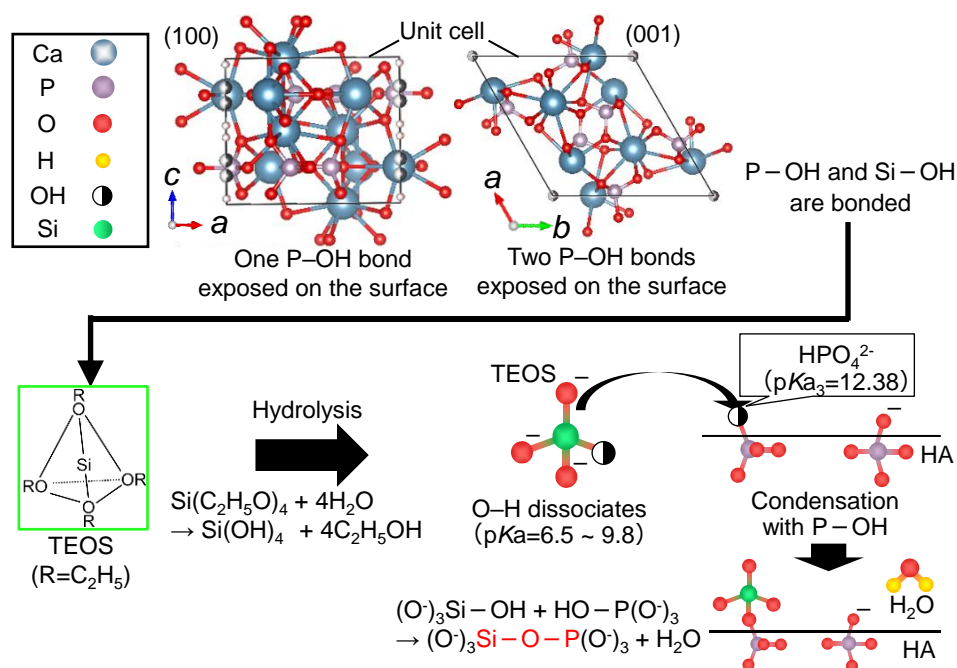
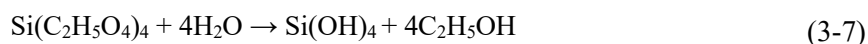


Figure 3-8. (a) FT-IR spectra of HA, MS and the MS/HA particles. (b-g) FT-IR spectral deconvolution results of chemical bonds of (b) HA, (c) MS, (d) MS/HA-0, (e) MS/HA-1, (f) MS/HA-2, and (g) MS/HA-3 at 800–1300 cm^{-1} .

Table 3-2. The peak assignments of the FT-IR spectra of the MS/HA particles.

Wavelength (cm ⁻¹)	Attribution	Bonding state
2800–3800	O–H	Stretching
2925	C–H (–CH ₃)	Stretching
2850	C–H (–CH ₂ –)	Stretching
1480	C–O	Stretching
1180	Si–O–Si ((Si–O–Si) _n)Asymmetry	Stretching
1120	Si–O	Stretching
1030	P–O Si–O–Si ((Si–O–Si) _n)Symmetry	Stretching Stretching
1008	Si–O–P	Stretching
970	P–O	Stretching
910	P–OH Si–OH	Stretching Stretching
605	O–P–O	Bending
565		

From the results above, the possible interfacial bonding formation between the MS and HA phases were considered as shown in **Scheme 3-4**. First, TEOS undergoes the hydrolysis reaction as follows.


Scheme 3-4. Illustration of the possible interfacial bonding formation between the MS and HA phases.

Then, (100) has one P–OH bond and (001) has two P–OH bonds were generated in HA crystal surfaces, and these functional groups would effectively interacted with the Si–OH on the MS phases. Here, the pK_a value of Si–OH is 6.5–9.8,⁷¹ and HPO_4^{2-} is 12.38 as follows.⁷²



Thus, the $Si-O^-$ and $P-O^-$ are mainly present on the surfaces in this synthetic solution. Therefore, the condensation reaction between the $Si-O^-$ and $P-O^-$ groups would effectively occur to form the following Si–O–P bond.⁷³

Figure 3-9 (a-f) shows the N_2 adsorption and desorption isotherms. According to the IUPAC hysteresis classification of the N_2 adsorption and desorption isotherm shapes,⁷⁴ the shape of HA could be indexed as type III, indicating the nonporous structures. The shape of MS could be indexed as the type IV and H4, indicating the bottleneck-shaped mesostructures. The shapes of the MS/HA particles were indexed as the type IV and H3, indicating the slit-shaped mesostructures (**Figure 3-9 (h)**). Thus, the mesostructures were changed by the hybridization processes. **Figure 3-9 (g)** shows the S_{BET} and BJH pore size distributions of the MS/HA particles.

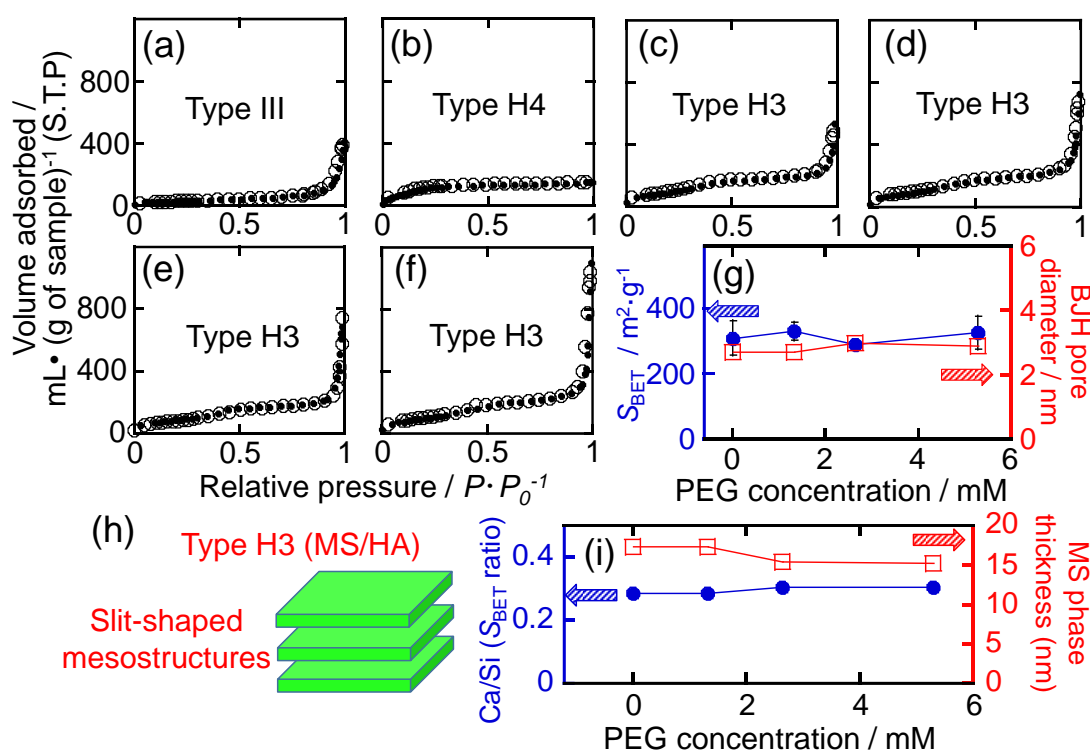


Figure 3-9. (a-f) N_2 adsorption (closed circles) and desorption (open circles) isotherms of (a) HA, (b) MS, (c) MS/HA-0, (d) MS/HA-1, (e) MS/HA-2 and (f) MS/HA-3, and (g) the changes of S_{BET} and BJH pore diameter of the MS/HA particles with the PEG concentration ($n=2$, mean \pm error). (h) The porous structure of particles as classified by IUPAC. (i) The changes of Ca/Si S_{BET} ratios and MS phase thickness of MS/HA particles with the PEG concentration.

The MS/HA particles had the S_{BET} of 288–330 $\text{m}^2\cdot(\text{g of sample})^{-1}$ and D_{BJH} of 2.7–3.0 nm, indicating the presence of mesopores, indicating the higher specific surface areas of the MS/HA particles of this study as compared to the case in the HA/silica hybrid materials in the previous reports. In previous reports, the S_{BET} values of MS-covered HA particles were 57–263 $\text{m}^2\cdot(\text{g of sample})^{-1}$ and D_{BJH} values were 13–73 $\text{m}^2\cdot(\text{g of sample})^{-1}$.^{75,76} The S_{BET} of HA was 108 $\text{m}^2\cdot\text{g}^{-1}$ and MS was 489 $\text{m}^2\cdot\text{g}^{-1}$, respectively. Here, the pore volume of MS was 0.2369 $\text{cm}^3\cdot\text{g}^{-1}$. On the other, the S_{BET} per unit weight of SiO_2 from the resultant chemical compositions by the XRF measurement was calculated to be 630–716 $\text{m}^2\cdot(\text{g of silica})^{-1}$ in the MS/HA particles. **Figure 3-9 (i) shows** Ca/Si S_{BET} ratios and MS phase thickness of MS/HA particles. It can be assumed that the high S_{BET} of MS/HA particles is due to the MS phase, and HA phase is covered with MS phase (15.2–17.4 nm). Previously-reported MS-covered HA particles had the uniform mesostructures with the thickness of the MS phase of approximately 20 nm.⁷⁷ The particles exhibited the high drug loading efficiency, and excellent near-infrared (NIR)- and pH-responsive drug release properties. The porous hollow silica nanoparticles with the shell thicknesses in the range of 5–45 nm indicated the UV-shielding and release control property of ivermectin.⁷⁸ Consequently, all the MS/HA particles with the MS phase (15.2–17.4 nm) of this study are expected to exhibit the mesostructure-based biofunctional properties. Therefore, the S_{BET} values only of the MS phase in the MS/HA particles were almost same to that of the MS inherent, indicating the successful mesopore formation of MS on the HA surfaces. Although there was no correlation between the PEG concentration and the S_{BET} , the mesopore size slightly increased with increasing the PEG chain addition amount. It was suggested that the part of PEG chains also contributed to the special formation of mesostructures.

Figure 3-10 (a–e) shows the particle size distributions. It was found that the particles were efficiently dispersed in PBS. The particles had the diameter of 122–184 nm. Taking into account the results in the TEM images, the particles formed the aggregation state in PBS to be monodispersed. It has been reported that the particle diameters of this study can be easily taken up by the cells without the cytotoxicity.⁷⁹ The average particle sizes before the electrophoretic collection for MS/HA-0, MS/HA-1, MS/HA-2, MS/HA-3 were 192, 179, 233 and 236 nm, respectively, indicating that the smaller and dispersed particles in PBS could be collected by the electrophoretic collection method of this study. After the collection, the *C.V.* value of MS/HA-3 particles is the lowest at 4.3 % in all the particles, indicating that the PEG chain addition decreased the *C.V.* value to be monodispersity of the particles. At the synthetic concentration of 5.30 mM, the monodispersed state of the particles as the aggregation form was successfully achieved. It was thought that the PEG chain isotropic liquid molecules existed on the MS/HA particles as the steric barrier to suppress the aggregation between the particles.⁸⁰ **Figure 3-10 (f)** shows the change of the zeta potential values of the MS/HA particles with the PEG concentration. The zeta potential value of MS/HA-0 was -9.3 ± 2.7 mV, MS/HA-1 was -21.9 ± 1.3 mV, MS/HA-2 was -22.0 ± 2.3

mV and MS/HA-3 was -33.8 ± 7.3 mV. The MS/HA particles indicated the higher zeta potential values than the case in HA alone. The zeta potential values of the MS/HA particles are almost same to that of the MS particles.⁸¹ Therefore, the MS phase would be present on the HA particle surfaces, which is agreed with the results by TEM images.

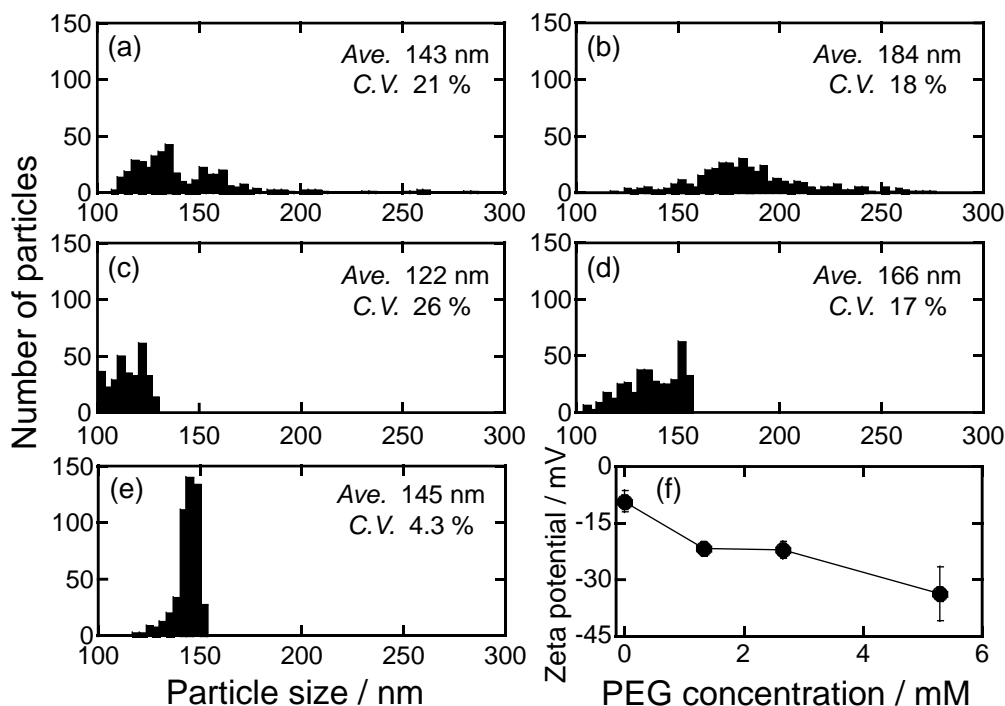
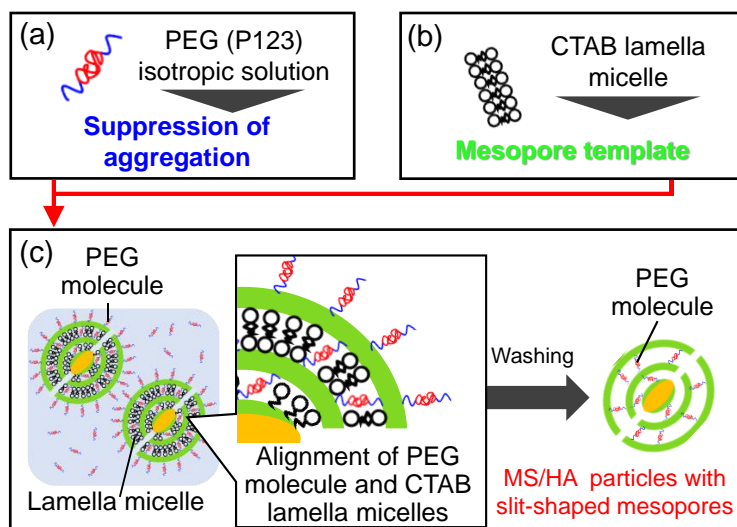


Figure 3-10. (a–e) The particle size distributions of (a) HA, (b) MS/HA-0, (c) MS/HA-1, (d) MS/HA-2 and (e) MS/HA-3. Here, the average particle size (Ave.) and coefficient of variation (C.V.) values were represented in the graphs. (f): The changes of zeta potential values of the nanostructured MS/HA hybrid particles with the PEG concentration ($n=3$, mean \pm S.D.).

Scheme 3-5 shows the illustration of the possible formation process of the MS/HA particles of this study. In the synthetic conditions in **chapter 3**, The CTAB and PEG isotropic liquid molecules would be in the solution, and CTAB lamella micelles were formed.^{82,83} When the HA and MS phases are hybridized together, the lamella micelles and part of PEG acted as the mesopore template and the PEG isotropic liquid molecules prevented the further aggregation between the particles.⁸⁴ In other words, the remaining PEG molecules with washing in the synthetic process effectively contribute to the dispersion stability of the aggregation form. Since the CTAB lamella micelles are positively charged, those are adsorbed on the siliceous precursors by electrostatic interaction. The micelle and silica structures are concertically aligned to form the concentric mesostructures. The MS/HA particles with slit-shaped mesopores were formed by removing the lamella micelles, and the PEG molecules would remain in the mesostructure. In this experiment, the particles could be synthesized at the PEG concentrations between 0–5.30 mM.



Scheme 3-5. The states and roles of (a) PEG (P123) molecule and (b) CTAB micelle. (c) Illustration of the possible formation process of the MS/HA particles of this thesis.

3.3.2 Hydration State Changes of the Mesoporous Silica-Covered Hydroxyapatite Particles with the Albumin Adsorption

The FT-IR spectral deconvolution results of three hydration layers (**Figure 3-11**) and of six water-interactive states (**Figure 3-12**) formed on the particles, and the resultant component ratios (%) of the six water-interactive states were shown in **Figure 3-12 (a)**. These spectral deconvolutions were performed with high accuracy. In comparison between the reference

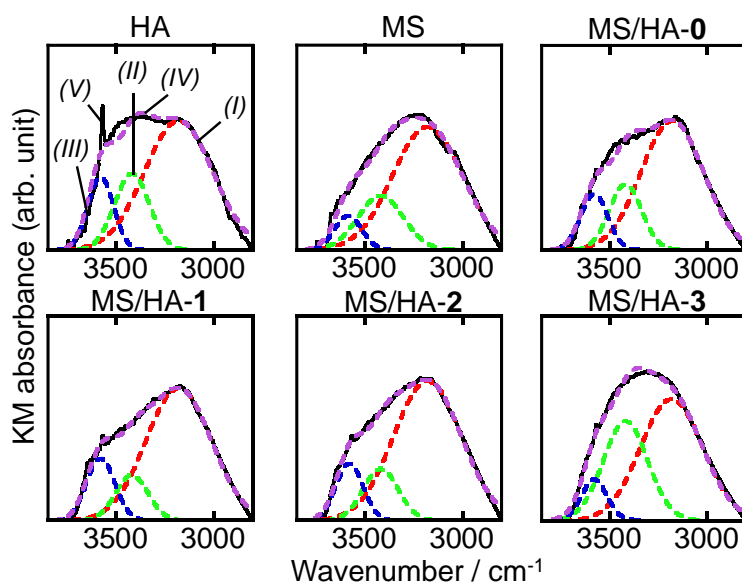


Figure 3-11. FT-IR spectral deconvolution results of three hydration layers formed on the particles. The separated (I), (II) and (III) peaks are attributed to free, intermediate and nonfreezing water molecular states, respectively, and their (IV) re-synthesized and (V) raw spectra are represented.

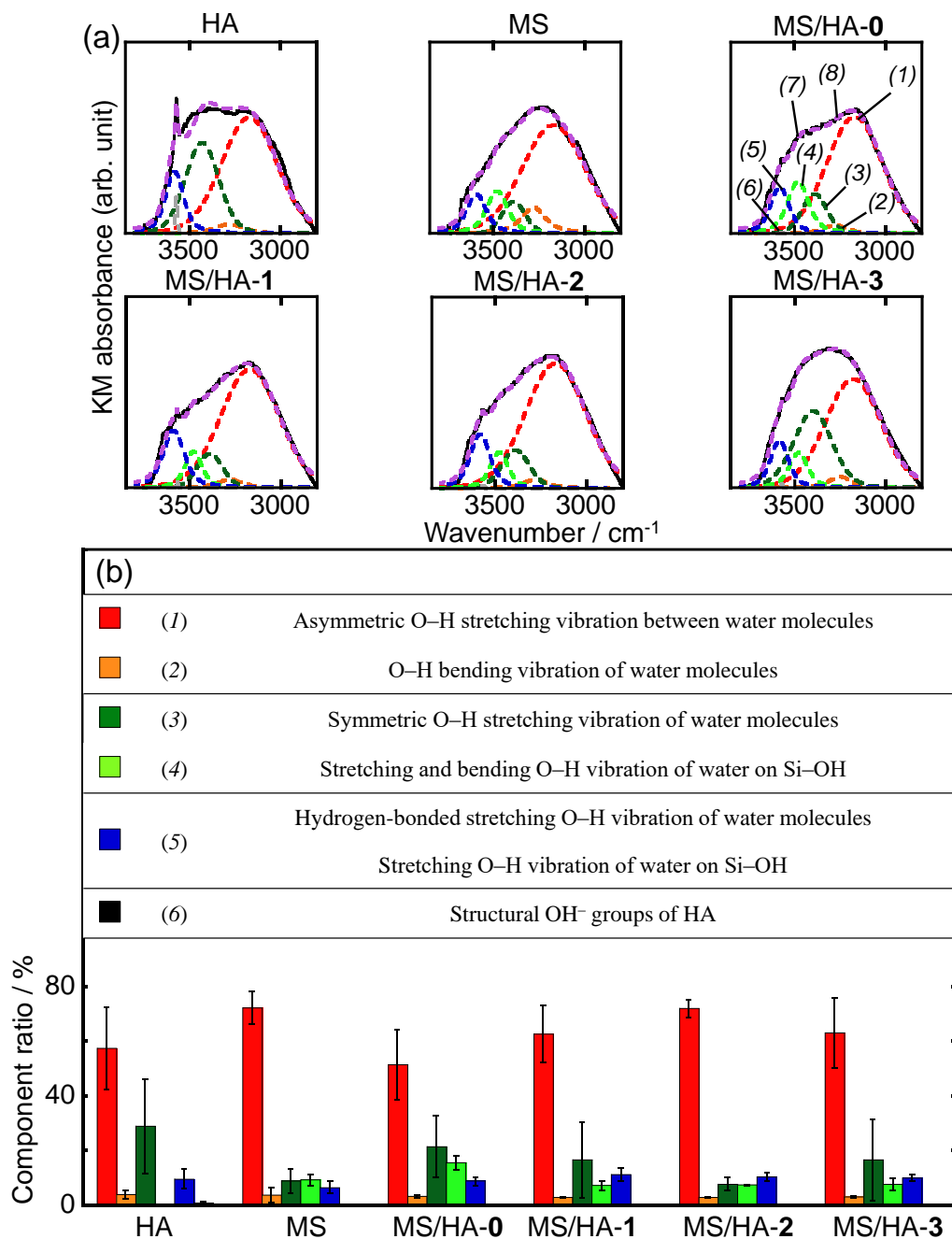


Figure 3-12. (a) FT-IR spectral deconvolution results of six water-interactive states formed on the particles, indicating the separated spectra of (1) asymmetric O–H stretching vibration between water molecules, (2) O–H bending vibration of water molecules, (3) symmetric O–H stretching vibration of water molecules, (4) stretching and bending O–H vibration of water on Si–OH, (5) hydrogen-bonded stretching O–H vibration of water molecules and stretching O–H vibration of water on Si–OH, and (6) structural OH⁻ groups of HA, respectively, and (7) their re-synthesized and (8) raw spectra. (b) Assignments of the six water-interactive states formed on the particles and resultant six component ratios.

particles and MS/HA-0, the component ratios of (4) stretching and bending O–H vibration of water on Si–OH increased by the hybridization (**Figure 3-12 (b)**). The component ratios of (1)

asymmetric O–H stretching vibration between water molecules and (3) symmetric O–H stretching vibration of water molecules were changed by the hybridization and adding the PEG chains. Therefore, the values need to be evaluated in detail.

Figure 3-13 (a) shows the resultant component ratios of three hydration layers formed on the particles and their ratios of intermediate water to free water. The hydration layer states on the particle surface assumed from these results is shown in **Scheme 3-6**. Nonfreezing water does not participate in the reaction because it has the same properties as solids. In comparison between the HA particles (**Scheme 3-6 (a)**) and MS/HA-0 (**Scheme 3-6 (b)**), the component ratio of (I) free water decreased and that of (II) intermediate water increased by the hybridization. The difference is thought to be due to the interaction between water molecules and particles (electrostatic interaction or hydrogen bond) and the presence or absence of porous structure. It is explained by the decrease in melting point with increasing interfacial contributions to the free energy of the solid and liquid by mesopores.^{85,86} Moreover, the component ratio of (I) increased and that of (II) decreased with increasing the PEG concentration. As a result, the ratio of free water to intermediate water decreased by the hybridization and increased with increasing the PEG concentration. Therefore, the MS/HA particles had the hydration layer structures with the larger ratio of intermediate water as compared to the case in the reference HA or MS alone, and the ratio of intermediate water could be controlled by the PEG concentration in the synthetic process. With increasing the added amount of PEG chains, the amount of the water molecules (i.e, clustering state) involved in the PEG chains as a PEG-interactive layer would increase.^{20,87} It is assumed that the ratio of the free water relatively increased by the clustering formation (**Scheme 3-6 (c)**). Here, the intermediate water weight concentration in MS/HA-0 particles was calculated according to **Chapter 2**. As a result, the MS/HA-0 particles thought to contain 4.7 wt% of the intermediate water, which is comparable to the previously-reported values for the polymers.^{16,88,89}

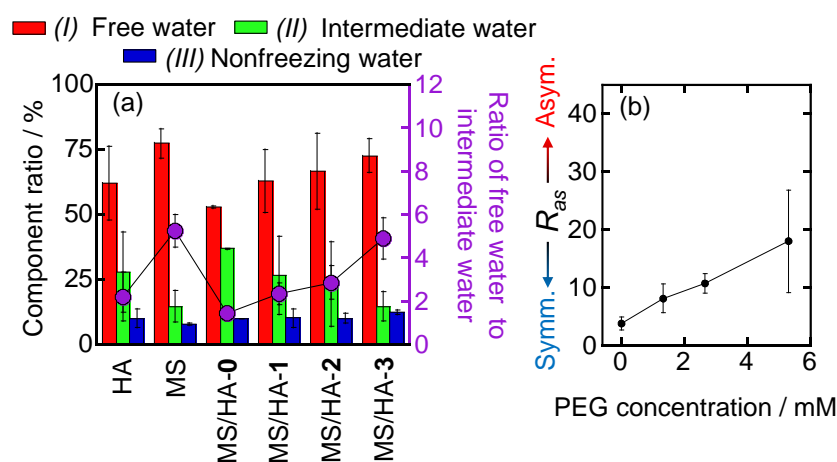
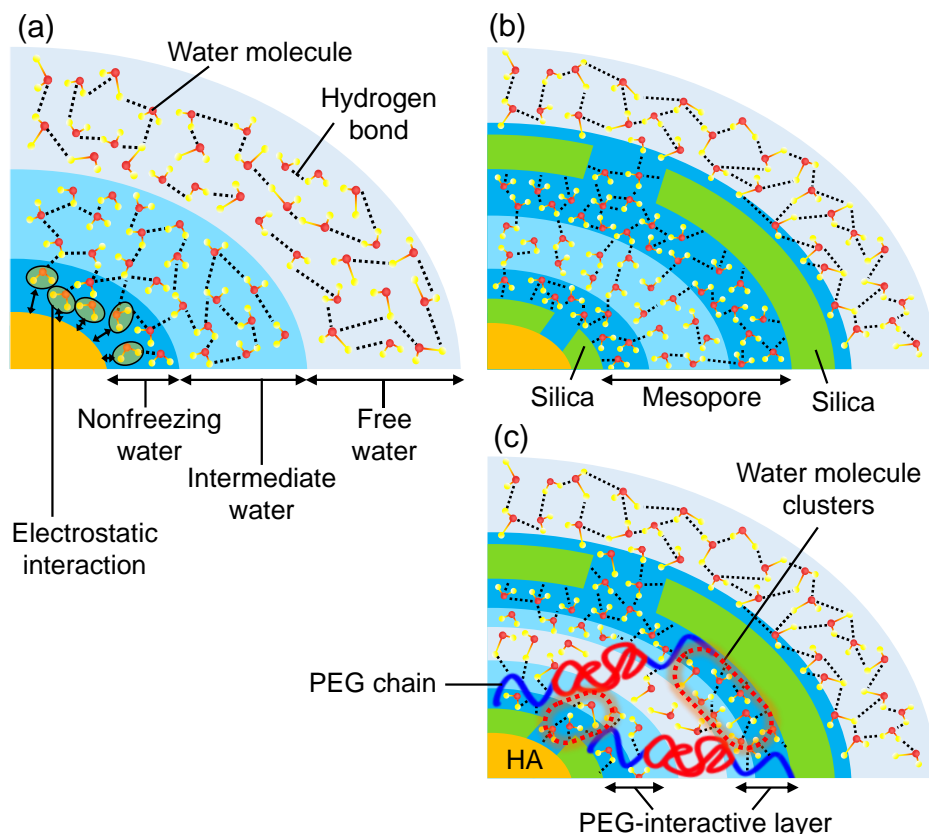


Figure 3-13. (a) Resultant component ratios of three hydration layers formed on the particles and their ratios of free water to intermediate water. (b) R_{as} value change with the PEG concentration.

Furthermore, the R_{as} increased with increasing the PEG concentration (**Figure 3-13 (b)**), suggesting that the PEG chains enhanced the asymmetric stretching vibration component ratio in free water on the MS/HA particles. It would be attributed to the formation of PEG-interactive layers under the presence of PEG molecule on the particle surfaces (**Scheme 3-6 (c)**). In particular, PEG chains of P123 is amphiphilic surfactant part and enclose the water molecules to form the PEG-interactive layers.^{20,87} According to the previous report, the mechanism of the hydration layers on the particles was suggested as follows.



Scheme 3-6. Illustration of hydration layer states on the particle surface of (a) HA, (b) MS/HA-0 and (c) MS/HA-3.

The PEG-interactive layer reduces the surface tension between the water molecules to weaken the hydrogen bonds.⁹⁰ As a result, the hydrogen bonds between the particles and the water molecules are strengthened. Thus, the hydrogen atom in the water molecules effectively forms the hydrogen bond with the oxygen atom on the particles (i.e., MS phase). Accordingly, the difference in the polarity occurs between water molecules, resulting in the formation of the asymmetric water molecular structures. In MS/HA-3, the hydrogen atoms of water molecules bind to the oxygen atoms of PEG chain, and resultingly water molecule clusters are formed,⁹¹ which has dominantly been attributed to ether oxygen as hydrogen bonding basicity in PEG.⁹² The amount of the water molecules involved in the PEG chains as the PEG-interactive layers

increased with increasing the PEG concentration, suggesting that the clustering states of water molecules were formed among the hydrogen bonding interactions based on the enhanced asymmetric O–H stretching. Therefore, it was found that the ratio of the (I) and R_{as} increased and that of the (3) decreased with increasing the PEG concentration.

The hydration layer states after Ab adsorption were also investigated. The FT-IR spectral deconvolution results of three hydration layers (Figure 3-14) and of six water-interactive states (Figure 3-15) formed on the Ab-adsorbed particles, and the resultant component ratios (%) of the six water-interactive states were shown in Figure 3-16, which were evaluated by the same method before the Ab adsorption. Figure 3-16 (a) shows the resultant component ratios of three hydration layers formed on the Ab-adsorbed particles and their ratios of intermediate water to free water. By the hybridization, the component ratio of (I) free water decreased and (II) intermediate water increased. In contrast, the component ratio of (I) increased and that of (II) decreased with increasing the PEG concentration. As a result, the ratio of free water to intermediate water decreased by hybridization and increased with increasing the PEG concentration, and the ratios were higher all around as compared with the case before the Ab adsorption (Figure 3-13 (a)). The component ratio of N–H stretching vibration increased due to the mesostructures and decreased with the PEG chain immobilization. Figure 3-16 (b) shows R_{as} (Ab_{ad}) with the PEG concentration. The R_{as} (Ab_{ad}) was higher all around than the R_{as} (Figure 3-13 (b)) and increased with increasing the PEG concentration. In the presence of the adsorbed Ab molecules, the water molecules of free water became abundant and the intermediate water decreased and the

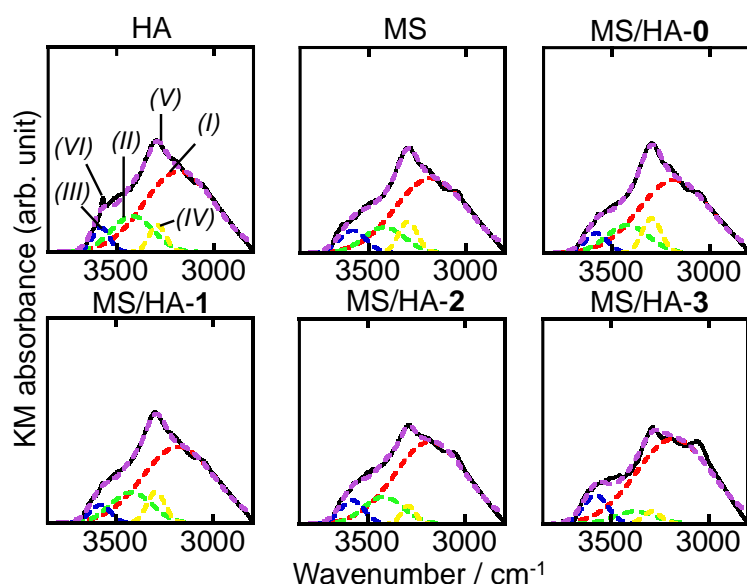


Figure 3-14. FT-IR spectral deconvolution results of three hydration layers formed on the Ab-adsorbed particles. The separated (I), (II) and (III) and (IV) peaks are attributed to free, intermediate, nonfreezing water molecular states and N–H stretching vibration of Ab, and their (V) re-synthesized and (VI) raw spectra are represented.

asymmetric stretching vibration component ratio in the hydration layer was formed, and these were effectively enhanced with increasing the PEG concentration.

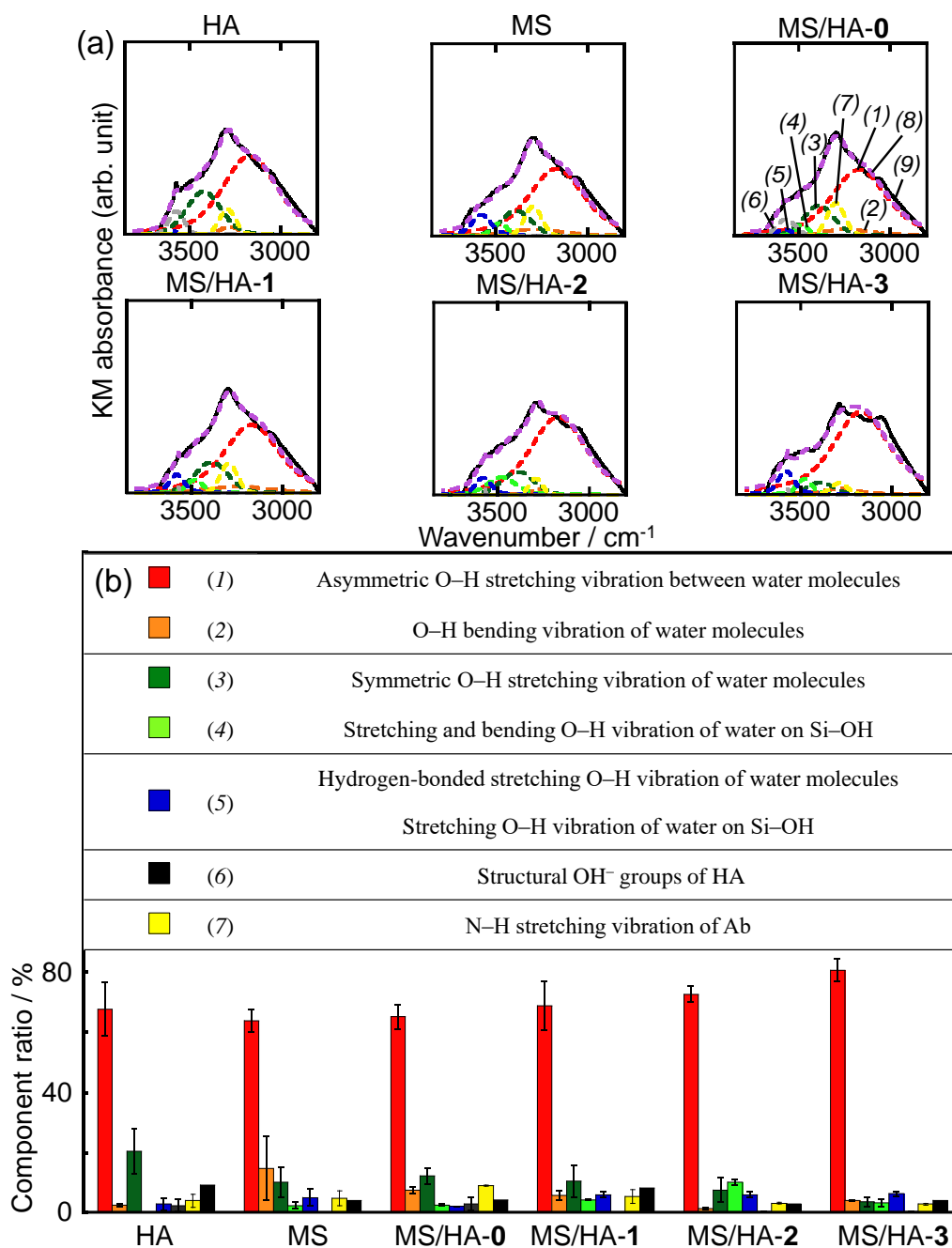


Figure 3-15. (a) FT-IR spectral deconvolution results of six water-interactive states formed on the Ab-adsorbed particles, indicating the separated spectra of (1) asymmetric O–H stretching vibration between water molecules, (2) O–H bending vibration of water molecules, (3) symmetric O–H stretching vibration of water molecules, (4) stretching and bending O–H vibration of water on Si–OH, (5) hydrogen-bonded stretching O–H vibration of water molecules and stretching O–H vibration of water on Si–OH, and (6) structural OH⁻ groups of HA (7) N–H stretching vibration of Ab, respectively, and (8) their re-synthesized and (9) raw spectra. (b) Assignments of the six water-interactive states formed on the particles and resultant six component ratios.

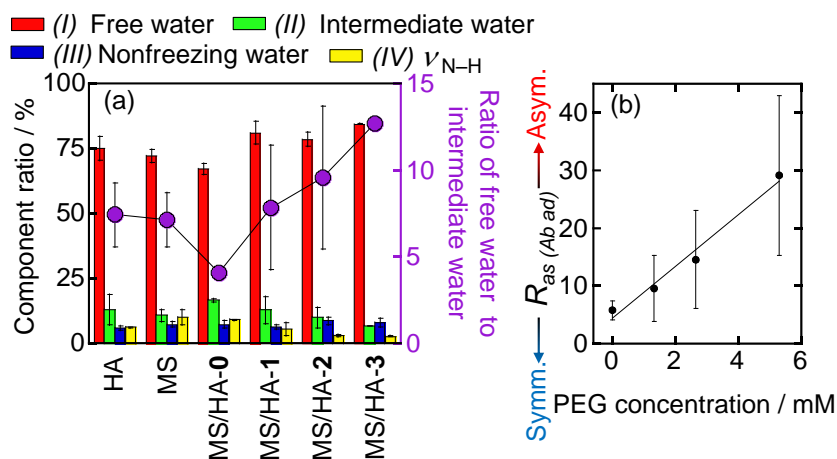


Figure 3-16. (a) Resultant component ratios of three hydration layers formed on the Ab-adsorbed particles and N–H stretching vibration of Ab, and their ratios of free water to intermediate water. (b) $R_{as} (Ab_{ad})$ value change with the PEG concentration ($R^2 = 0.97989$).

3.3.3 Surface Modification Effect of the Hydroxyapatite Particles on Albumin Adsorption States by Interfacial Hydration States

The protein adsorption layer formed on the hydration layer was evaluated. **Table 3-3** shows the Ab adsorbed amounts per weight and per BET surface area on the particles. The adsorbed amounts of Ab increased by the hybridization and decreased with increasing the PEG concentration, suggesting that the different Ab adsorption amount would be attributed to the hydration layer structure. The zeta potential values of the particles showed the negative values between -9.3 to -33.8 mV (**Figure 3-10 (f)**), which was repulsed against the negatively-charged Ab in the solution. Moreover, the molecular size of the hydrated Ab (elliptical shape: $14 \times 3.8 \times 3.8$ nm)⁹³ exceeds the pore size of the MS/HA particles (2.7–3.0 nm). Taking into account the above results, it was proposed that the hydration structures as well as the mesostructures would

Table 3-3. Adsorbed Ab amounts per weight and per BET surface area on the particles (n=3, mean \pm S.D.).

	Adsorbed amount / mmol·g ⁻¹	Adsorbed amount per BET surface area / nmol·m ⁻²
HA	0.26 \pm 0.06	2.41 \pm 0.06
MS	0.84 \pm 0.55	1.71 \pm 0.55
MS/HA-0	1.45 \pm 0.04	4.71 \pm 0.04
MS/HA-1	0.98 \pm 0.01	2.96 \pm 0.01
MS/HA-2	0.79 \pm 0.37	2.74 \pm 0.37
MS/HA-3	0.79 \pm 0.42	2.45 \pm 0.42

affect the Ab adsorption states. Here, there has been the report that the MS particles with the pore size of 2.48 nm exhibited the larger adsorption amount of Ab as compared with the case in the MS particles with the pore size of 5.35 nm.⁹⁴ The size of 2.48 nm is smaller than that of the hydrated Ab molecule, suggesting that the adsorption state was folded and adapted the mesostructures, which was different from the molecular sieve effect. Here, the adsorption area of the Ab molecule was estimated, and the sectional area of the elliptical-shaped Ab molecule was assumed to be $270 \times 10^{-18} \text{ m}^2$ for calculating the molecular occupancy of the adsorbed Ab on the particles. Using the average particle diameters of 122–184 nm from the results of **Figure 3-10**, the particles were assumed to be nonporous sphere and the specific surface areas was calculated to be 11.9–18.0 $\text{m}^2 \cdot (\text{g of sample})^{-1}$. In the case of the assumption as the nonporous spherical structures, the molecular occupancy for HA, MS/HA-0, MS/HA-1, MS/HA-2 and MS/HA-3 was 318%, 1981%, 885%, 976% and 860 %, respectively. In the case of the assumption as the mesostructures, the molecular occupancy calculated using the S_{BET} values from the results of **Figure 3-9** for HA, MS, MS/HA-0, MS/HA-1, MS/HA-2 and MS/HA-3 was 39.3 %, 27.8 %, 76.7 %, 48.2 %, 44.5 % and 39.9 %, respectively, Taking into account that the Ab adsorption state is restricted to be a monolayer,⁹⁵ it was revealed that the Ab adsorbed inside and outside the mesopores at the monolayer.

In order to evaluate the secondary structures of the adsorbed Ab, the FT-IR spectral deconvolution results of the amide I bands and their secondary structural component ratios (%) were shown in **Figure 3-17**. All the particles exhibited the different component ratios as compared with the case in the Ab alone, which was freeze-dried according to the method mentioned above (**Figure 3-2**). However, the definitive change was not seen among the six components. **Figure 3-18 (a)** shows the native state component ratios of the secondary structures. The component ratio of the native state increased by the hybridization and decreased with increasing the added PEG concentration. Furthermore, the relationship between the R_{as} of the hydration layer and the native state component ratio were considered in **Figure 3-18 (b)**. The native state component ratio decreased with increasing R_{as} . It was suggested that the increase in R_{as} is involved in the native state component ratios. Here, the Ab adlayer states on the particle surfaces assumed from these results was suggested in **Scheme 3-7**. The HA particles are positively-charged in solution, and the negatively-charged Ab can be adsorbed with an electrostatic interactions (**Scheme 3-7 (a)**). On the other hand, Ab was adsorbed with hydrogen bond on the MS/HA particle surfaces (**Scheme 3-7 (b, c)**). It is known that the protein adsorbed in the mesopores suppresses denaturation.⁹⁶ Since the MS/HA-0 particles have a large component ratio of intermediate water, the Ab adsorption state had been maintained for the same reason as in **Chapter 2 (Scheme 3-7 (b))**. In the absence of repulsive force by intermediate water (MS/HA-3), the clustered water molecules cut off the hydration layer and weaken the repulsive force. As a result, the Ab

molecules partially react with the PEG chains with hydrophobic interaction, promoting the protein denaturation based on the theory in Chapter 2.

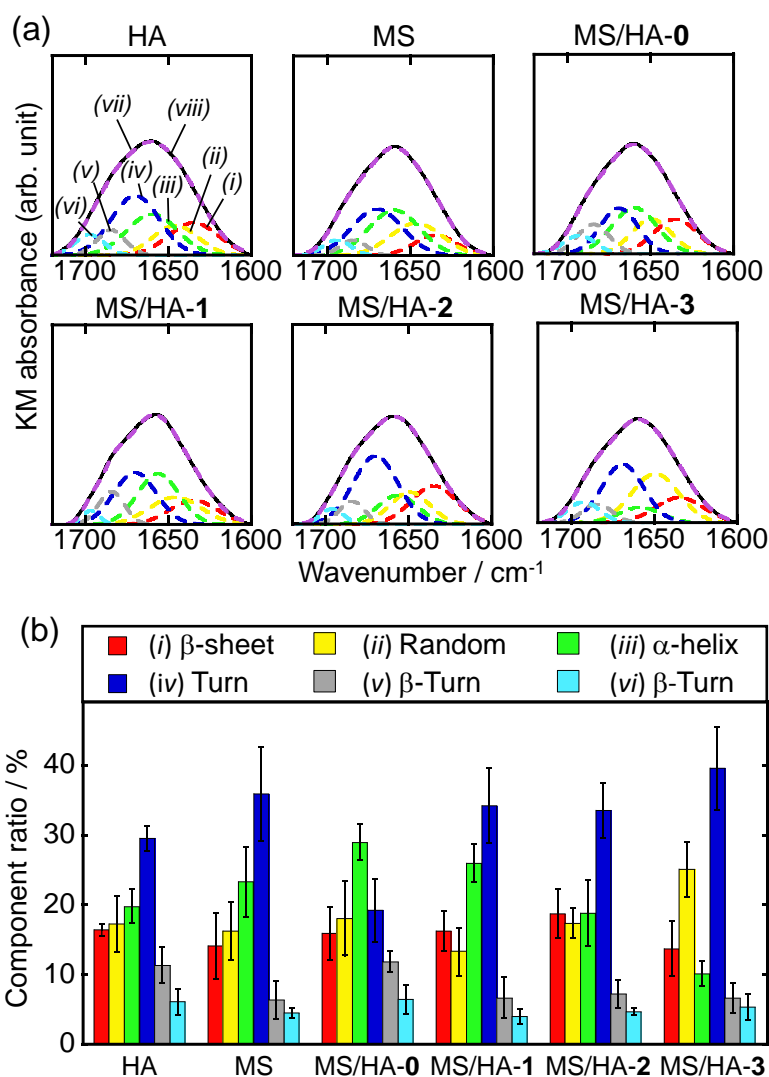


Figure 3-17. (a) FT-IR spectral deconvolution results of the amide I bands of the adsorbed Ab on the particles to provide the secondary structural components ((i) β -sheet, (ii) random, (iii) α -helix, (iv) turn, (v)(vi) β -turn), and their (vii) re-synthesized and (viii) raw spectra. (b) Component ratios on the secondary structures of the amide I bands in the adsorbed Ab on the particles.

Here, the hydration layer forms a regular network structure with continuous hydrogen bonds via nonfreezing water, intermediate water, and free water. It has been reported that the water molecules in the hydration layers effectively form the tetrahedral hydrogen bonding networks, and the networks had the low flexibility.⁹⁰ Thus, it was supposed that the protein adsorption layers were more flexible as compared with the case in the water molecules in the hydration layers. In other words, the hydration layer on the surface is an important factor influencing proteins.⁹⁷ From the backgrounds, the native-state-like Ab adsorption is expected on the surface of MS/HA-0, which forms the regular hydrogen bonding network. In MS/HA-3, Ab forms the complex

hydrogen bond with the MS phase, water molecules, and PEG chain, which is expected to reduce the native state component ratio (Scheme 3-7 (c)).

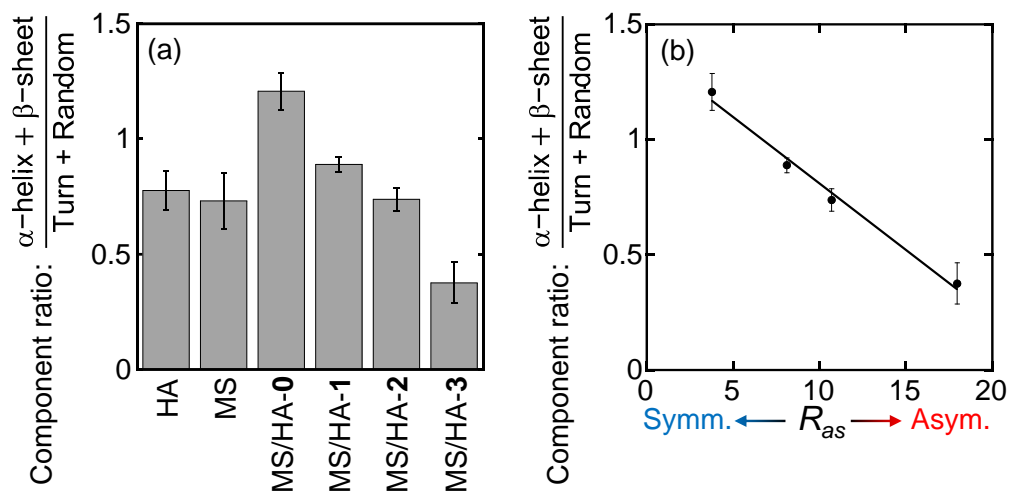
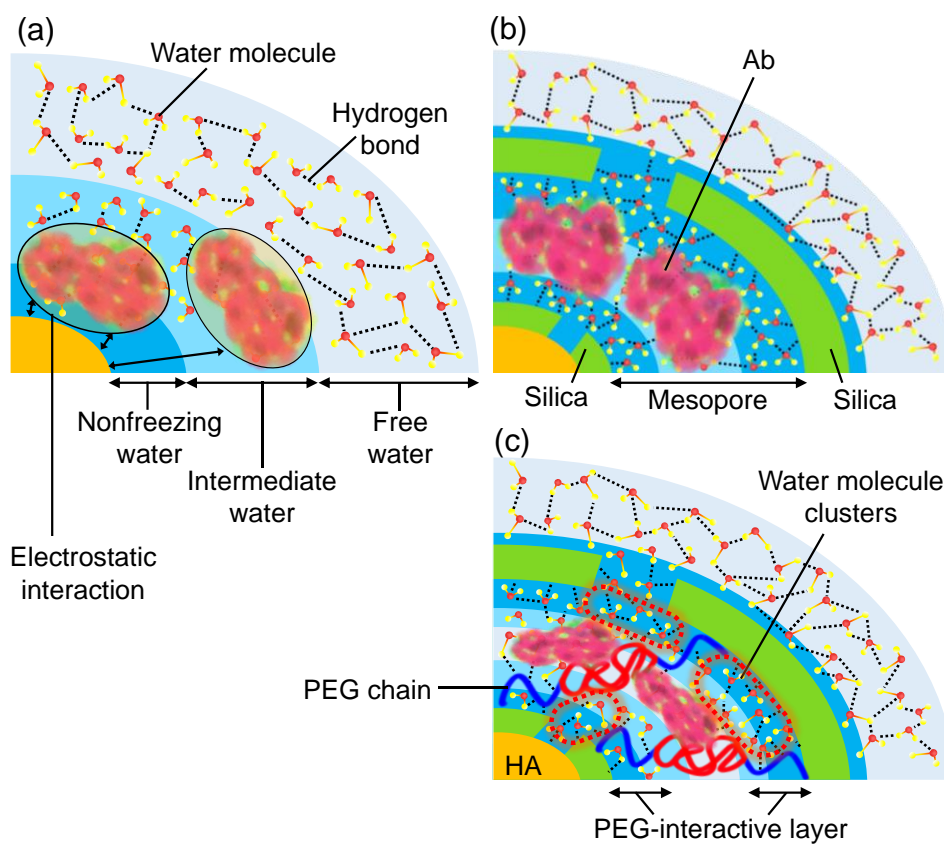


Figure 3-18. (a) The native state component ratios of the secondary structures and (b) their ratio changes with R_{as} ($R^2 = 0.98907$)



Scheme 3-7. Illustration of Ab adlayer states on the particle surface of (a) HA, (b) MS/HA-0 and (c) MS/HA-3.

3.4 Conclusion

The MS/HA particles were successfully synthesized under the existence of PEG chains. The particles formed the slit-shaped mesostructures by the bonding formation between the MS and HA phases containing PEG chains on the surfaces. Furthermore, the aggregation form of the particles exhibited the dispersion stability in water at the monodispersed state. The Ab-adsorbed amounts were significantly increased by the mesostructured of the MS phase. Then, the hydration layer states and the adsorbed Ab on the particles were investigated to understand the effect of the hydration layer states on the Ab secondary structures. The ratio of free water to intermediate water decreased by the hybridization, and increased with increasing the PEG concentration. By the hybridization, the component ratio of the asymmetric O–H stretching vibration between free water molecules decreased, and that of the symmetric O–H stretching vibration of intermediate water molecules increased. With increasing the PEG concentration, the asymmetric O–H stretching vibration between free water molecules increased and the symmetric O–H stretching vibration of intermediate water molecules decreased. Furthermore, it was found that the protein native state component ratio decreased with increasing the R_{as} , the relationship between the R_{as} and the protein native state component ratio was found. Therefore, the thesis resultantly reported the synthesis of MS/HA particles containing PEG chains for controlling the hydrated Ab adsorption state.

References

- 1 O. Johnell and J. A. Kanis, *Osteoporos. Int.*, 2006, **17**, 1726–1733.
- 2 A. Sobti, P. Agrawal, S. Agarwala and M. Agarwal, *Arch. bone Jt. Surg.*, 2016, **4**, 2–9.
- 3 W. E. Brown and L. C. Chow, *J. Dent. Res.*, 1986, **65**, 1115–1120.
- 4 T. Kurien, R. G. Pearson and B. E. Scammell, *Bone Jt. J.*, 2013, **95 B**, 583–597.
- 5 K. Kaveh, R. Ibrahim, M. Z. A. Bakar and T. A. Ibrahim, *J. Anim. Vet. Adv.*, 2010, **9**, 1055–1067.
- 6 C. J. Damien and J. R. Parsons, *J. Appl. Biomater.*, 1991, **2**, 187–208.
- 7 M. Jarcho, *Clin. Orthop. Relat. Res.*, 1981, **157**, 259–78.
- 8 N. N. Bou-Abboud, J. L. Patat, G. Guillemain, S. Issahakian, N. Forest and J. P. -Ouhayoun, *Biomaterials*, 1994, **15**, 201–207.
- 9 F. Matassi, L. Nistri, D. Chicon Paez and M. Innocenti, *Clin. Cases Miner. Bone Metab.*, 2011, **8**, 21–4.
- 10 G. Skaliczki, K. Schandl, M. Weszl, T. Major, M. Kovács, J. Skaliczki, M. Szendrői, C. Dobó-Nagy and Z. Lacza, *Int. Orthop.*, 2013, **37**, 741–745.
- 11 C. T. Laurencin, M. A. Attawia, L. Q. Lu, M. D. Borden, H. H. Lu, W. J. Gorum and J. R. Lieberman, *Biomaterials*, 2001, **22**, 1271–1277.

- 12 M. I. Alam, I. Asahina, K. Ohmamiuda and S. Enomoto, *J. Biomed. Mater. Res.*, 2001, **54**, 129–138.
- 13 H. Frauenfelder, P. W. Fenimore and B. H. McMahon, *Biophys. Chem.*, 2002, **98**, 35–48.
- 14 B. Bagchi, *Chem. Rev.*, 2005, **105**, 3197–3219.
- 15 J. Israelachvili and H. Wennerström, *Nature*, 1996, **379**, 219–225.
- 16 M. Tanaka and K. Sato, *Netsu Sokutei*, 2012, **39**, 151–157.
- 17 M. Tanaka, A. Mochizuki, T. Shiroya, T. Motomura, K. Shimura, M. Onishi and Y. Okahata, *Colloids Surfaces A Physicochem. Eng. Asp.*, 2002, **203**, 195–204.
- 18 M. Tanaka and A. Mochizuki, *J. Biomed. Mater. Res. - Part A*, 2004, **68**, 684–695.
- 19 O. Tirosh, Y. Barenholz, J. Katzhendler and A. Prievo, *Biophys. J.*, 1998, **74**, 1371–1379.
- 20 I. Sugiyama and Y. Sadzuka, *Drug Deliv. Syst.*, 2016, **31**, 275–282.
- 21 S. Schöttler, G. Becker, S. Winzen, T. Steinbach, K. Mohr, K. Landfester, V. Mailänder and F. R. Wurm, *Nat. Nanotechnol.*, 2016, **11**, 372–377.
- 22 B. Thierry, L. Zimmer, S. McNiven, K. Finnie, C. Barbé and H. J. Griesser, *Langmuir*, 2008, **24**, 8143–8150.
- 23 D. F. Williams, *Biomaterials*, 2008, **29**, 2941–2953.
- 24 H. Shin, S. Jo and A. G. Mikos, *Biomaterials*, 2003, **24**, 4353–4364.
- 25 S. Koutsopoulos, *J. Biomed. Mater. Res.*, 2002, **62**, 600–612.
- 26 W. R. Walsh and N. Guzelsu, *Biomaterials*, 1994, **15**, 137–145.
- 27 T. Kataoka, K. Shiba, L. Y. Wang, S. Yamada and M. Tagaya, *RSC Adv.*, 2017, **7**, 19479–19485.
- 28 Y. Chai, M. Nishikawa and M. Tagaya, *Adv. Powder Technol.*, 2018, **29**, 1198–1203.
- 29 F. Miyaji, Y. Kono and Y. Suyama, *Mater. Res. Bull.*, 2005, **40**, 209–220.
- 30 F. Ye, H. Guo, H. Zhang and X. He, *Acta Biomater.*, 2010, **6**, 2212–2218.
- 31 X. Ren, Z. Sun, X. Ma, Y. Wang, X. Cui, Z. Yi, X. Sun, B. Guo and X. Li, *Langmuir*, 2018, **34**, 6797–6805.
- 32 R. Jugdaohsingh, *J. Nutr. Heal. Aging*, 2007, **11**, 99–110.
- 33 S. J. Whiting and H. H. Draper, *J. Nutr.*, 1981, **111**, 1721–1726.
- 34 W. J. Landis, D. D. Lee, J. T. Brenna, S. Chandra and G. H. Morrison, *Calcif. Tissue Int.*, 1986, **38**, 52–59.
- 35 E. M. Carlisle, *Ciba Found. Symp.*, 1986, **121**, 123–39.
- 36 E. M. Carlisle, *Science.*, 1972, **178**, 619–621.
- 37 I. R. Gibson, S. M. Best and W. Bonfield, *J. Biomed. Mater. Res.*, 1999, **44**, 422–428.
- 38 F. Balas, J. Pérez-Pariente and M. Vallet-Regí, *J. Biomed. Mater. Res. Part A*, 2003, **66A**, 364–375.
- 39 P. Saravanapavan and L. L. Hench, *J. Non. Cryst. Solids*, 2003, **318**, 1–13.

- 40 T. Kokubo, M. Shigematsu, Y. Nagashima, M. Tashiro, T. Nakamura, T. Yamamuro and S. Higashi, *Bull. Inst. Chem. Res.*, 1982, **60**, 260–268.
- 41 H. M. Kim, T. Himeno, T. Kokubo and T. Nakamura, *Biomaterials*, 2005, **26**, 4366–4373.
- 42 S. Yamada and M. Tagaya, *Mater. Lett.*, 2017, **209**, 441–445.
- 43 S. Yamada, M. Nishikawa and M. Tagaya, *Mater. Lett.*, 2018, **211**, 220–224.
- 44 Y. F. Zhao and J. Ma, *J. Nanosci. Nanotechnol.*, 2009, **9**, 3720–3727.
- 45 C. T. Kresge, M. E. Leonowicz, W. J. Roth, J. C. Vartuli and J. S. Beck, *Nature*, 1992, **359**, 710–712.
- 46 T. Yanagisawa, T. Shimizu, K. Kuroda and C. Kato, *Bull. Chem. Soc. Jpn.*, 1990, **63**, 988–992.
- 47 T. Kataoka, L. Wang, K. Kobayashi, M. Nishikawa and M. Tagaya, *Jpn. J. Appl. Phys.*, 2016, **55**, 105503.
- 48 I. I. Slowing, J. L. Vivero-Escoto, C. W. Wu and V. S. Y. Lin, *Adv. Drug Deliv. Rev.*, 2008, **60**, 1278–1288.
- 49 S. Marchesan and M. Prato, *ACS Med. Chem. Lett.*, 2013, **4**, 147–149.
- 50 E. W. Hansen, M. Stöcker and R. Schmidt, *J. Phys. Chem.*, 1996, **100**, 2195–2200.
- 51 A. Schreiber, I. Ketelsen and G. H. Findenegg, *Phys. Chem. Chem. Phys.*, 2001, **3**, 1185–1195.
- 52 G. Q. Lu and X. S. Zhao, Eds., *Nanoporous Materials: Science and Engineering*, Imperial College Press, 2004.
- 53 M. Tagaya, T. Yamaguchi and K. Shiba, *Cryst. Growth Des.*, 2016, **16**, 2843–2849.
- 54 Y. C. Shang, S. Yamada, Y. D. Chai and M. Tagaya, *Key Eng. Mater.*, 2018, **782**, 59–64.
- 55 M. Handke and W. Mozgawa, *Vib. Spectrosc.*, 1993, **5**, 75–84.
- 56 L. J. Bellamy, *The Infrared Spectra of Complex Molecules*, Springer Netherlands, Dordrecht, 1980.
- 57 S. Brunauer, L. S. Deming, W. E. Deming and E. Teller, *J. Am. Chem. Soc.*, 1940, **62**, 1723–1732.
- 58 E. P. Barrett, L. G. Joyner and P. P. Halenda, *J. Am. Chem. Soc.*, 1951, **73**, 373–380.
- 59 M. Thommes, K. Kaneko, A. V. Neimark, J. P. Olivier, F. Rodriguez-Reinoso, J. Rouquerol and K. S. W. Sing, *Pure Appl. Chem.*, 2015, **87**, 1051–1069.
- 60 J. C. Maxwell, *A Treatise on Electricity and Magnetism*, Cambridge University Press, Cambridge, 2010, vol. II.
- 61 Lord Rayleigh, *London, Edinburgh, Dublin Philos. Mag. J. Sci.*, 1892, **34**, 481–502.
- 62 R. C. Schroden, M. Al-Daous, C. F. Blanford and A. Stein, *Chem. Mater.*, 2002, **14**, 3305–3315.
- 63 D. Kozak, W. Anderson, R. Vogel, S. Chen, F. Antaw and M. Trau, *ACS Nano*, 2012, **6**, 6990–6997.

- 64 R. J. Hunter, in *Zeta Potential in Colloid Science*, Elsevier, 1981, pp. 373–386.
- 65 E. L. C. J. Blundell, R. Vogel and M. Platt, *Langmuir*, 2016, **32**, 1082–1090.
- 66 G. Steiner, S. Tunc, M. Maitz and R. Salzer, *Anal. Chem.*, 2007, **79**, 1311–1316.
- 67 Y. Liu, M. X. Xie, J. Kang and D. Zheng, *Spectrochim. Acta - Part A Mol. Biomol. Spectrosc.*, 2003, **59**, 2747–2758.
- 68 J. Vogel, C. Russel, G. Gunther, P. Hartmann, F. Vizethum and N. Bergner, *J. Mater. Sci. Mater. Med.*, 1996, **7**, 495–499.
- 69 Y. Chai, T. Yamaguchi and M. Tagaya, *Cryst. Growth Des.*, 2017, **17**, 4977–4983.
- 70 L. Todan, C. Andronescu, D. M. Vuluga, D. C. Culita and M. Zaharescu, *J. Therm. Anal. Calorim.*, 2013, **114**, 91–99.
- 71 D. N. Strazhesko, V. B. Strelko, V. N. Belyakov and S. C. Rubanik, *J. Chromatogr. A*, 1974, **102**, 191–195.
- 72 E. D. Black and E. Hayon, *J. Phys. Chem.*, 1970, **74**, 3199–3203.
- 73 A. M. Elnahrawy and A. I. Ali, *J. Glas. Ceram.*, 2014, **4**, 42–47.
- 74 K. S. W. Sing, D. H. Everett, R. A. W. Haul, L. Moscou, R. A. Pierotti, J. Rouquerol and T. Siemieniewska, in *Handbook of Heterogeneous Catalysis*, Wiley-VCH Verlag GmbH & Co. KGaA, Weinheim, Germany, 2008.
- 75 S. Ng, J. Guo, J. Ma and S. C. J. Loo, *Acta Biomater.*, 2010, **6**, 3772–3781.
- 76 S. Dasgupta, A. Bandyopadhyay and S. Bose, *Acta Biomater.*, 2009, **5**, 3112–3121.
- 77 Z. Song, Y. Liu, J. Shi, T. Ma, Z. Zhang, H. Ma and S. Cao, *Mater. Sci. Eng. C*, 2018, **83**, 90–98.
- 78 X. Hao, X. Hu, C. Zhang, S. Chen, Z. Li, X. Yang, H. Liu, G. Jia, D. Liu, K. Ge, X.-J. Liang and J. Zhang, *ACS Nano*, 2015, **9**, 9614–9625.
- 79 K. Deshmukh, M. M. Shaik, S. R. Ramanan and M. Kowshik, *ACS Biomater. Sci. Eng.*, 2016, **2**, 1257–1264.
- 80 A. Sugawara-Narutaki, *Bull. Chem. Soc. Japan*, 2017, **52**, 15–19.
- 81 W. H. Zhang, L. Zhang, J. Xiu, Z. Shen, Y. Li, P. Ying and C. Li, *Microporous Mesoporous Mater.*, 2006, **89**, 179–185.
- 82 G. Wanka, H. Hoffmann and W. Ulbricht, *Macromolecules*, 1994, **27**, 4145–4159.
- 83 A. Firouzi, D. Kumar, L. M. Bull, T. Besier, P. Sieger, Q. Huo, S. A. Walker, J. A. Zasadzinski, C. Glinka, J. Nicol, D. Margolese, G. D. Stucky and B. F. Chmelka, *Science.*, 1995, **267**, 1138–1143.
- 84 K. Schumacher, M. Grün and K. K. Unger, *Microporous Mesoporous Mater.*, 1999, **27**, 201–206.
- 85 P. R. Couchman and W. A. Jesser, *Nature*, 1977, **269**, 481–483.
- 86 K. M. Unruh, T. E. Huber and C. A. Huber, *Phys. Rev. B*, 1993, **48**, 9021–9027.
- 87 T. J. Daou, L. Li, P. Reiss, V. Josserand and I. Texier, *Langmuir*, 2009, **25**, 3040–3044.

- 88 Y. K. Sung, D. E. Gregonis, M. S. John and J. D. Andrade, *J. Appl. Polym. Sci.*, 1981, **26**, 3719–3728.
- 89 S. J. Kim, S. J. Park and S. I. Kim, *React. Funct. Polym.*, 2003, **55**, 53–59.
- 90 M. Nakasako, *Mol. Sci.*, 2008, **2**, A0022.
- 91 H. Kitano, K. Ichikawa, M. Ide, M. Fukuda and W. Mizuno, *Langmuir*, 2001, **17**, 1889–1895.
- 92 M. Matsuguchi, S. Umeda, Y. Sadaoka and Y. Sakai, *Sensors Actuators B Chem.*, 1998, **49**, 179–185.
- 93 X. M. He and D. C. Carter, *Nature*, 1992, **358**, 209–215.
- 94 A. Katiyar, L. Ji, P. G. Smirniotis and N. G. Pinto, *Microporous Mesoporous Mater.*, 2005, **80**, 311–320.
- 95 Y. L. Jeyachandran, E. Mielczarski, B. Rai and J. A. Mielczarski, *Langmuir*, 2009, **25**, 11614–11620.
- 96 K. C. Kao, T. S. Lin and C. Y. Mou, *J. Phys. Chem. C*, 2014, **118**, 6734–6743.
- 97 M. Tagaya, T. Ikoma, N. Hanagata and J. Tanaka, *Mater. Express*, 2012, **2**, 1–22.

Chapter 4

Summary and Future Perspectives

Chapter 4

Summary and Future Perspectives

4.1 Summary

Injecting bioceramic particles into the bone defect is currently being attempted for repair and regeneration of the bone defects. In the conventional particles, there was a problem of the burden on the patient, the inflammation reaction and long-term for repair and regeneration. In order to solve these problems, this thesis focuses on the surface-modified silicate-containing hydroxyapatite (SiHA) particles. Hydroxyapatite (HA) particles containing silicate that mimics the living bone were synthesized, these HA particles were immobilized by poly(ethylene glycol) (PEG), evaluated and clarified the hydration layers and protein adlayers.

In *Chapter 1, "General Introduction"*, conventional types, problems and issues with the bioceramics for bone defects were explained, and the necessity to synthesize a new bioceramic particles for bone defects was described. The necessity of synthesizing particles that can support collagen (Col) and albumin (Ab) that promotes bone regeneration with ideal protein structures was proposed. Then, it was shown the importance of designing the coexistence of HA with silicate for mimetic compositions in the living body. Furthermore, it was described the hydration layer affects protein secondary structures and explained how the PEG affect the hydration layers, and showed the significance and purpose of the thesis.

In *Chapter 2, "Modification of Hydroxyapatite Particles with Tetraethoxysilane and Polyethylene glycol and Evaluation of Their Hydration States and Collagen Fibrillation"*, the silicate-containing HA (SiHA) particles were synthesized and immobilized by PEG for clarifying the effect of bioceramic surface hydration layer states on the Col fibrillation. The plate-like SiHA particles containing SiO_4^{4-} ions inside or/and outside the particles were obtained. PEG was successfully immobilized on the SiHA particles, and the hydration layer and Col adlayer states on the particles were investigated for exemplifying the importance of the water molecular states at the interface. The ratio of free to intermediate water on the particles decreased by containing silicate component, and that increased with increasing the PEG

molecular occupancy, where the R_{as} increased with increasing the occupancy. Surprisingly, all the $R_{as (Col. ad)}$ values were higher than the cases in R_{as} , indicating the hydration layer state and interaction changes by the Col adsorption. In the QCM-D measurement, the Δf and ΔD values of the PEG immobilized SiHA particles increased with the Col adsorption for 32–34 mins and then Δf slightly increased (or stopped increasing) and ΔD dramatically increased, indicating the effective water mobility and state changes by the Col adsorption and subsequent fibrillation on the PEG-immobilized particles. The Col fibrillation degree, which was evaluated by $\tan\delta$ and protein secondary structure of the adlayers, clearly increased by the PEG-immobilization, and the tendency was supported by the fibril density under the SEM observation. Although the stereoscopic states of the Col on the SiHA particles were preserved with the adsorption, SiHA-P100 can widely and effectively induce the Col fibrillation by the PEG-immobilization. In particular, the Col fibrillation degree based on the protein secondary structure was significantly correlated with the asymmetric stretching vibration component ratio in free water molecules of the hydration layer on the particles, suggesting the importance of the hydration layer states on bioceramics for controlling the efficient Col fibrillation.

In **Chapter 3**, "*Modification of Hydroxyapatite Particles with Mesoporous Silica and Polyethylene glycol and Evaluation of Their Hydration States and Albumin Interactions*", the mesoporous silica (MS)-covered HA (MS/HA) particles were successfully synthesized under the existence of PEG chains. The particles formed the slit-shaped mesostructures by the bonding formation between the MS and HA phases containing PEG chains on the surfaces. Furthermore, the aggregation form of the particles exhibited the dispersion stability in water at the monodispersed state. The Ab-adsorbed amounts were significantly increased by the mesostructured of the MS phase. Then, the hydration layer states and the adsorbed Ab on the particles were investigated to understand the effect of the hydration layer states on the Ab secondary structures. The ratio of free water to intermediate water decreased by the hybridization, and increased with increasing the PEG concentration. By the hybridization, the component ratio of the asymmetric O–H stretching vibration between free water molecules decreased, and that of the symmetric O–H stretching vibration of intermediate water molecules increased. With increasing the PEG concentration, the asymmetric O–H stretching vibration between free water molecules increased and the symmetric O–H stretching vibration of intermediate water molecules decreased. Furthermore, it was found that the protein native state component ratio decreased with increasing the R_{as} , the relationship between the R_{as} and the protein native state component ratio was found. Therefore, the thesis resultantly reported the synthesis of MS/HA particles containing PEG chains for controlling the hydrated Ab adsorption state.

4.2 Future Perspectives

4.2.1 Novel Design of Bioceramic Particles with Both Substitution and Regeneration Properties

In the cells of the osteoblasts and osteoclasts, organic substances such as proteins, inorganic substances such as calcium phosphate have played an important role in the bone remodeling mechanism.¹ **Figure 4-1** shows the bone remodeling mechanism. First, pre-osteoclasts differentiated from hematopoietic stem cells are absorbed and bound to old bone, and calcium and phosphate ions are released. After osteoclasts apoptotic, the pre-osteoblasts differentiated from mesenchymal stem cells adhere to the decomposed part of the bone. Organic substances mainly composed of type I Col are secreted from these osteoblasts to form an unmineralized substrate. Simultaneously, matrix vesicles, which are derived from the osteoblasts that have taken up calcium and phosphate ions, form calcium phosphate. The calcium phosphate forms calcospherites outside the cells, and the calcification begins along with the uncalcified matrix to form calcified tissues when they reach the uncalcified matrix while accumulating and expanding. It is thought that the part of osteoblasts is captured by the calcified ground substance and become bone cells to promote the formation of new bone tissues containing Col aggregates along with the formation.

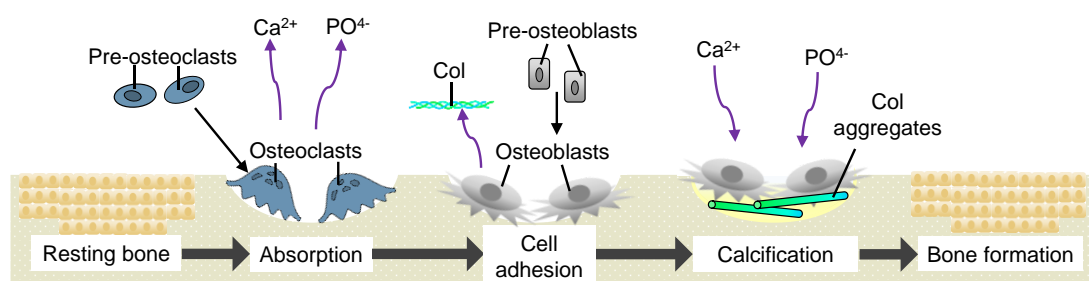


Figure 4-1. Illustration of bone remodelling mechanism.

When the implant materials are used to repair bone defects, long-term treatment may cause inflammation. Therefore, it is important to develop materials that simultaneously promote repair and regeneration. Bioceramic particles are known to be useful for repairing bone defects,²⁻⁴ but it takes a long time to regenerate and integrate the surrounding tissues.⁵⁻⁷ Thus, the bioceramic particles that promote effective bone regeneration should be developed. On the other hand, there have been various molecules (e.g., Ab, BMP-2) that promote bone regeneration.^{8,9} The concerted effect of bioceramic particles and growth-factor protein on bone repair and regeneration have been expected. Accordingly, the effective bone regeneration by the

adsorption of bone morphogenetic proteins on the bioceramic particles have been studied so far.^{10,11}

In order to solve the problem that the conventional filling bioceramic particles take a long time to become compatible and bind to the tissues *in vivo*, leading to a possibility of reoperation, so it is supposed that the bioceramic particle states is as follows. First, The bioceramic particles with the chemical compositions and structures similar to the living bone can adhere directly to living bone tissues and exhibit high biocompatibility.¹² Second, it is necessary to form the mesopore structures that can support the proteins that promote bone regeneration. Third, the bioceramic particle with a diameter between 50–200 nm may exhibit cytotoxicity, and it is assumed important to precisely control the particle size.^{13,14}

The scheme of the illustration of the possible bioceramic particle satisfying the conditions mentioned above is suggested in **Figure 4-2**. **Figure 4-2 (a)** shows the illustration of the possible bioceramic particle that promote both repairing and regeneration. For the promotion, the concerted techniques of bone-like bioceramic particle and sustained release of proteins are useful. In detail, **Figure 4-2 (b)** shows the process of slow release and absorption of the supported protein by cells. First, the proteins that promote bone formation are supported in the

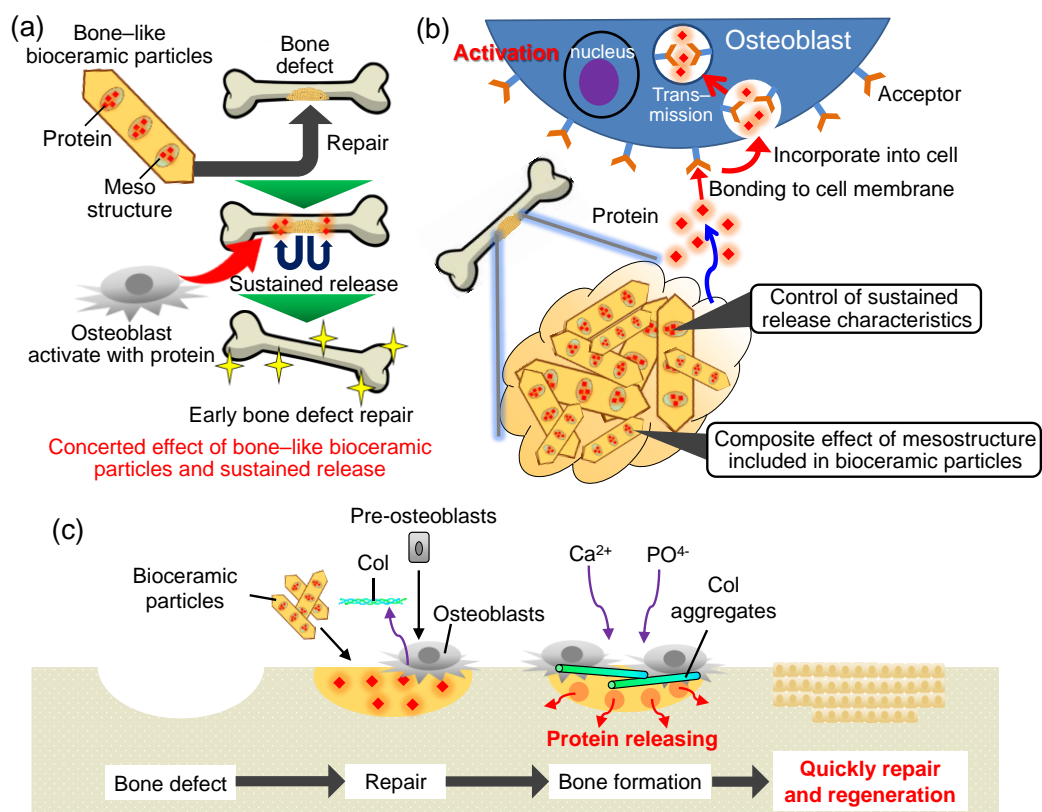


Figure 4-2. Suggested schemes of (a) bone-like bioceramic particles for repair and regeneration while activating the surrounding tissue, and (b) bioceramic particles activating the surrounding osteoblasts for bone repair and regeneration. (c) Illustration of bone remodelling with bioceramic particles.

mesostructure of the bioceramic particle with the chemical composition and structures similar to the living bone tissues. Second, by dispersing and pasting the particle and then filling them into the bone defect sites, proteins are slowly released from the mesostructure and bind to the osteoblast membranes around the bone defect. Then, it is considered that the released proteins are taken up into osteoblasts, reach the nucleus, activate the cellular activities (e.g., differentiation), and finally promote bone regeneration. If the situation can be reproduced, it will be possible to quickly repair and regenerate the bone defect as shown in **Figure 4-2 (c)**, the reaction as shown in **Figure 4-1** occurs quickly. If the bioceramic particle that effectively promote the bone regeneration process can be synthesized, it is considered that both the repair and regeneration can be achieved at the same time. The particles which were synthesized in this study are also expected to be the repair and regeneration of bone defects.

4.2.2 Prospect of Practical Application for Substituting Bone Defects

The surface modification of HA particles were successfully achieved, and proposing the relationship between the hydration layers and protein secondary structures as well as the importance of additive effect of PEG. Further studies are important to develop bioceramic particles for repairing and regeneration for bone defects toward future applications in such a field as regenerative medicine. In order to synthesis bioceramic particles for bone defect, one of the keys would be to control interfacial interactions between hydration layers and protein interactions, and selection of processes and hardeners for clinical trials. In addition, to understand the interfacial interactions between hydration layers and protein interactions will lead to a large number of multifunctional HA nanoparticles that advance the frontier technologies of bio-related fields.

The specific usage of bioceramic particles for substituting bone defects were suggested as follows. After adsorbing the Ab into the mesostructures of the MS/HA-0 (**Chapter 3**), the particles are mixed with the SiHA-P100 (**Chapter 2**) and hardener in order to make bioceramic particle pastes. When the pastes are injected into the bone defects, the Ab released from mesostructures of the MS/HA-0 promotes the osteoblast proliferation. Large numbers of osteoblasts by suppressing the differentiation will produce the abundant Col molecules. At the same time, Col molecules present in the extracellular matrix effectively becomes Col fibrils on the SiHA-P100 surface. When the Ab concentration decrease, the osteoblasts differentiate into bone tissues and forms the composite with Col fibrils, resulting in the contribution to repairing the bone defect. Here, the previous studies have been reported that the Si-substituted HA particles improved the reactivity between HA and Ab.^{15,16} The MS particles indicated the molecular sieve effect, so the Col molecules that are much larger than the pore size cannot be adsorbed into the mesostructures of the MS/HA particles.^{17,18} Therefore, the Ab adsorption on

the SiHA particles (**Chapter 2**) and Col adsorption on the MS/HA particles (**Chapter 3**) are not expected to adversely affect bone regeneration and repair. The investigation of the behavior as the bioceramic particle pastes *in vivo* is a topic of this study for the future.

References

- 1 H. C. Anderson, *J. Cell Biol.*, 1969, **41**, 59–72.
- 2 W. E. Brown and L. C. Chow, *J. Dent. Res.*, 1986, **65**, 1115–1120.
- 3 T. Kurien, R. G. Pearson and B. E. Scammell, *Bone Jt. J.*, 2013, **95 B**, 583–597.
- 4 K. Kaveh, R. Ibrahim, M. Z. A. Bakar and T. A. Ibrahim, *J. Anim. Vet. Adv.*, 2010, **9**, 1055–1067.
- 5 C. J. Damien and J. R. Parsons, *J. Appl. Biomater.*, 1991, **2**, 187–208.
- 6 M. Jarcho, *Clin. Orthop. Relat. Res.*, 1981, **157**, 259–78.
- 7 N. N. Bou-Abboud, J. L. Patat, G. Guillemain, S. Issahakian, N. Forest and J. P. -Ouhayoun, *Biomaterials*, 1994, **15**, 201–207.
- 8 F. Matassi, L. Nistri, D. Chicon Paez and M. Innocenti, *Clin. Cases Miner. Bone Metab.*, 2011, **8**, 21–4.
- 9 G. Skaliczki, K. Schandl, M. Weszl, T. Major, M. Kovács, J. Skaliczki, M. Szendrői, C. Dobó-Nagy and Z. Lacza, *Int. Orthop.*, 2013, **37**, 741–745.
- 10 C. T. Laurencin, M. A. Attawia, L. Q. Lu, M. D. Borden, H. H. Lu, W. J. Gorum and J. R. Lieberman, *Biomaterials*, 2001, **22**, 1271–1277.
- 11 M. I. Alam, I. Asahina, K. Ohmamiuda and S. Enomoto, *J. Biomed. Mater. Res.*, 2001, **54**, 129–138.
- 12 M. Ogiso, *Biomaterials*, 1980, **1**, 59–66.
- 13 G. Oberdorster, J. Ferin, R. Gelein, S. C. Soderholm and J. Finkelstein, *Environ. Health Perspect.*, 1992, **97**, 193–199.
- 14 D. W. Porter, N. Wu, A. F. Hubbs, R. R. Mercer, K. Funk, F. Meng, J. Li, M. G. Wolfarth, L. Battelli, S. Friend, M. Andrew, R. Hamilton, K. Sriram, F. Yang, V. Castranova and A. Holian, *Toxicol. Sci.*, 2013, **131**, 179–193.
- 15 F. Xiao, L. Peng, Y. Zhang and L. Yun, *J. Mater. Sci. Mater. Med.*, 2009, **20**, 1653–1658.
- 16 W. Pon-On, N. Charoenphandhu, J. Teerapornpuntakit, J. Thongbunchoo, N. Krishnamra and I.-M. Tang, *Mater. Chem. Phys.*, 2013, **141**, 850–860.
- 17 H. H. P. Yiu, P. A. Wright and N. P. Botting, *Microporous Mesoporous Mater.*, 2001, **44–45**, 763–768.
- 18 H. Takahashi, B. Li, T. Sasaki, C. Miyazaki, T. Kajino and S. Inagaki, *Microporous Mesoporous Mater.*, 2001, **44–45**, 755–762.

Achievement List

Publication Papers

1. **Shota Yamada**, Satoshi Motozuka, Motohiro Tagaya, Synthesis of nanostructured silica/hydroxyapatite hybrid particles containing amphiphilic triblock copolymer for effectively controlling hydration layer structures with cytocompatibility, *Journal of Materials Chemistry B*, 8, 1524–1537 (2020).
2. **Shota Yamada**, Takaki Kobashi, Motohiro Tagaya, “Control of the hydration layer states on phosphorus-containing mesoporous silica films and their reactivity evaluation with biological fluids”, *Journal of Materials Chemistry B*, 9, 1896–1907 (2021).
3. **Shota Yamada**, Yadong Chai, Motohiro Tagaya, “PEG-immobilization effect of silicate-containing hydroxyapatite particles on effective collagen fibrillation for exemplifying importance of interfacial hydration layer states”, *Physical Chemistry Chemical Physics*, 19, (2022).

Other Related Publication Papers and Patents

1. **Shota Yamada**, Motohiro Tagaya, “Analytical investigation of hydration and protein adsorption structures on hydroxyapatite-based mesoporous silica particles”, *Materials Letters*, 209, 441–445 (2017).
2. **Shota Yamada**, Masami Nishikawa, Motohiro Tagaya, “Mesoporous silica formation on hydroxyapatite nanoparticles”, *Materials Letters*, 211, 220–224 (2018).
3. **Shota Yamada**, Yucheng Shang, Iori Yamada, Motohiro Tagaya, “Synthesis of phosphonate-containing mesoporous silica spheres under basic condition”, *Advanced Powder Technology*, 30, 1116–1119 (2019).

Presentation in International Conference and Symposium (○ : oral presenter)

1. Yucheng Shang, **○Shota Yamada**, Yadong Chai, Motohiro Tagaya, “Synthesis of Spherical Phosphate-containing Mesoporous Silicas for Improving Their Reaction Behaviors in Simulated Body Fluid.” [Presentation No. BIO30-P0085] *30th Symposium and Annual Meeting of the*

International Society for Ceramics in Medicine, October, 2018 (Nagoya, Japan)._

2. **○ Shota Yamada**, Tania Guadalupe Penaflor Galindo; Motohiro Tagaya, “Preparation of Nanoporous Silica/Hydroxyapatite Hybrid Particles for Effectively Controlling Protein-interactions.” [Presentation No. 3a-401-03] *The 11th International Conference on the Science and Technology for Advanced Ceramics*, July, 2019 (Tsukuba, Japan).